Measurement and unsteady flow modelling of centrifugal compressor surge

Measurement and Unsteady Flow Modelling
of Centrifugal Compressor Surge

Measurement and Unsteady Flow Modelling of Centrifugal Compressor Surge

PROEFSCHRIFT

ter verkrijging van de graad van doctor aan de Technische Universiteit Eindhoven, op gezag van de Rector Magnificus, prof.dr. R.A. van Santen, voor een commissie aangewezen door het College voor Promoties in het openbaar te verdedigen op

woensdag 16 oktober 2002 om 16.00 uur

door

Corina Henrica Jacoba Meuleman

geboren te Goor

Dit proefschrift is goedgekeurd door de promotoren:

prof.dr.ir. A.A. van Steenhoven
en
prof.dr.ir. J.J. Kok

Co-promotor:
dr.ir. H.C. de Lange

Contents

Summary

At small mass flows the performance of a compression system is limited by the occurrence of aerodynamic flow instabilities, which can lead to catastrophic failure of the compressor due to mechanical and thermal loads. This so-called surge of the compression system is characterised by large amplitude pressure rise oscillations and an unsteady mass flow. The present study is concerned with measurement and modelling of centrifugal compressor surge.

Surge is studied in a laboratory gas turbine installation. At different rotational speeds and throttle valve settings surge was measured with a pressure transducer at the outlet of the compressor. From the pressure data the minimum and maximum pressure rise in a surge cycle, and the surge frequency ($\approx 19 - 24$ [Hz]) are determined. The surge frequency increases as the throttle valve is closed, which indicates that the system experiences a classic or deep surge. To investigate the mass flow oscillation during surge, a single hot-wire probe was positioned at the inlet of the compressor. By correlating the velocity to the mass flow an impression of the period with positive flow in the surge cycle is obtained.

Existing models to simulate surge are based on a lumped parameter approach of the system in which the compressor performance is modelled to react quasi-steady to flow changes. If in this conventional model the parameters of the compression system that are geometrical determined are used, the simulated surge frequency is larger and the maximum pressure rise is smaller compared to measurement. However, the shape of the surge cycle at the maximum pressure rise is captured well. To match the simulated maximum pressure rise and surge frequency with measurement, the ratio of the compressor duct length and the plenum volume has to be increased by a factor ten compared to the physical value. Nevertheless, in this case the shape of the surge cycle at the maximum pressure rise is simulated incorrectly.

In this study, a new correction is developed to improve the simulation results of the conventional model. In the conventional model the compressor performance is assumed to react quasi-steady to flow changes, while an unsteady performance is more realistic. Therefore, the developed correction accounts for the influence of the unsteady boundary layer on the compressor performance and is derived by considering the unsteady momentum equation of a fully-developed laminar flow in a duct. An important parameter in this simplified case is the Stokes number (α). The correction applied in the range $0.5 < \alpha < 80$ results in a better agreement of the amplitude and phase of the simulated pressure and mass flow oscillations with respect to the exact solution.

Subsequently, it is studied whether the correction term can be translated to a turbulent inlet flow. For verification purposes, PIV and pressure drop measurements in a water channel facility with

and without an adverse pressure gradient are performed for $0.7 < \alpha < 7.5$. Especially, for the adverse pressure gradient flow a difference between the simulations with the conventional model and experiments is found. Simulations with the improved model result in an amplitude ratio and a phase, of the mass flow and pressure, that agree well with the experimental results.

Finally, the correction is applied to the experimental compression system for which $\alpha \approx 10$. Simulations with the improved model result in a surge frequency and a maximum pressure rise as well as a pressurisation period of the surge cycle that agree with measurement. Hence, the contribution of the unsteady boundary-layer on the performance of the compressor is captured well by the developed correction. A gain of the improved model is that the parameters depend on the physical quantities of the compression system. Furthermore, a specific parameter ratio is obtained that depends on the kind of compressor that is used, rather than on the system in which the compressor operates.

Chapter 1

Introduction

1.1   Axial and centrifugal compressors

The topic of this thesis is the physical understanding and modelling of surge in compressors. Aerodynamic flow instabilities of this kind limit the performance and operating regime of the machine and can lead to severe damage of a compressor.

Axial and centrifugal compressors are widely used for the pressurization of gases. The driving force for the development of compressible flow machines was the gas turbine, which application is mainly seen in aircraft engines and electrical power generation. The gas turbine produces mechanical (shaft) power by expansion of a compressed gas through an expander. A combustion chamber positioned between the compressor and expander provides energy to overcome losses and to develop useful power. Besides the gas turbine a large market exists for the internal combustion engine turbocharger, which is used in diesel and gasoline engines. The internal combustion engine turbocharger compresses the gas entering the manifold of the engine and is driven by a turbine running on the engine exhaust gases. In turbocharging a wide range of stable operation is necessary. This is an advantage of a centrifugal compressor with its generally wider operational area. Other applications of the compressor are for ventilation, process and chemical industries.

Axial and centrifugal compressors transfer energy from a rotating device to a gas, using shaft torque to impart the moment to the gas. Different components of the compressor can be distinguished. In the case of an axial compressor, see Figure 1.1(a), each stage consists of a row of rotor blades followed by a row of stator blades. In the rotor passage the flow is initially accelerated and then decelerated by the stator blades. Here the kinetic energy transferred to the gas in the rotor passage is converted to static pressure. The centrifugal (radial) compressor, see Figure 1.1(b), consists essentially of a rotating impeller and a number of fixed diverging passages in which the gas is decelerated with a consequent rise of the static pressure. The different diverging passages in the diffuser region are the vaneless or vaned region, and a volute which function is to duct flow away and to decelerate the flow further.

(a) axial compresor

(b) centrifugal compressor
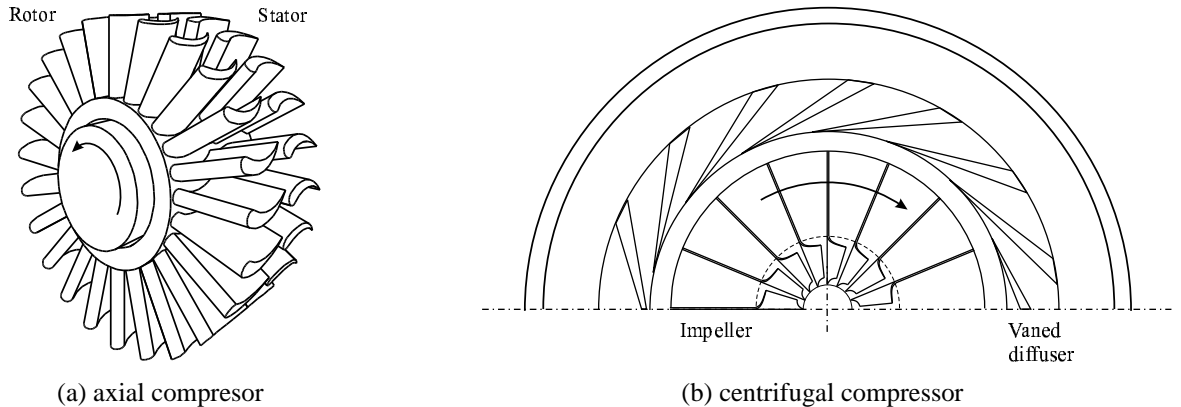
Figure 1.1: Sketch of a compressor.

1.2   Compressor map

The steady performance of the compressor is often specified in a compressor map by curves that relate the rotational speed, the pressure rise across the compressor and the mass flow through the compressor. Figure 1.2 shows a compressor performance of the centrifugal turbocharger compressor used in this study, approximated by *Willems [70]* see Appendix C.4, presented in two different ways. The left-hand side Figure 1.2(a) shows the overall performance of the compressor by plotting the pressure ratio versus the mass flow for a range of rotational speeds in full dimensions. The compressor pressure ratio is the ratio of the compressor outlet pressure (p_2) to the compressor inlet pressure (p_1 or p_0 if the inlet pressure is ambient). In the right-hand side Figure 1.2(b) the same data is plotted but nondimensionalised by use of the aerodynamic scaling. A discussion on the aerodynamic scaling can be found in Appendix A. The figure shows the pressure rise coefficient versus the inlet flow coefficient. Expressed in these aerodynamic variables it is seen that the compressor performance is almost independent of the rotational speed, i.e. the Mach number is not an important variable in the range of rotational speeds in which this compressor was operated. The operating range of a compressor is bounded for high mass flows by the phenomenon known as choking, which is indicated by the stone wall line. The choking occurs when locally, usually in the vaned diffuser throat or impeller throat, the flow becomes equal to the speed of sound (*[72]*). At low mass flows the compressor experiences unstable flow. As the flow is reduced, at a constant rotational speed, a point is reached at which the slightest further reduction in flow rate leads to an abrupt and definite change in flow pattern in the compressor. Beyond this point the compressor enters into either rotating stall or surge that is marked by the surge (or stall) line.

1.3   Unsteady compressor flow

Two compressor flow instabilities are known to occur for small mass flows in compressors, i.e., rotating stall and surge. A review of these instabilities in turbomachines can be found in
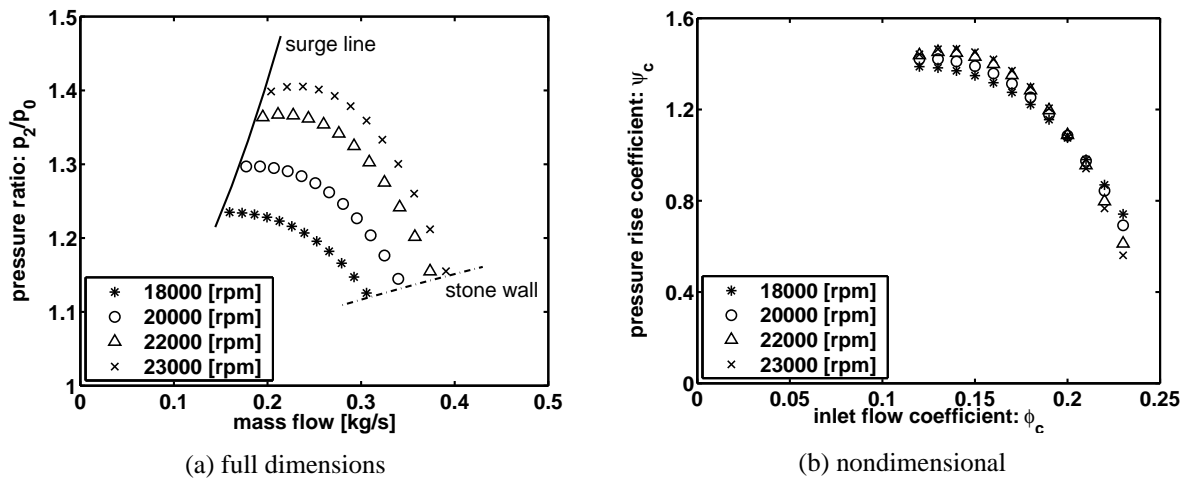
Figure 1.2: Compressor map.

Greitzer [33] and *Pampreen [56]*.

Rotating stall is a two-dimensional, local instability phenomenon in which one or more local regions of stagnant flow, i.e. stall cells, rotate around the circumference of the compressor. The annulus-averaged compressor mass flow is steady, but circumferentially non-uniform. This can have a large impact on the bearings of the compressor shaft. Furthermore, rotating stall induces large vibratory stresses in the blades and can result in a large drop in performance and efficiency that has disastrous effects on the performance of e.g. airplane engines. The effect of the rotating stall is local to the compressor, so it hardly affects the flow far upstream or downstream of the compressor. Some features of rotating stall can be found in Appendix B.

Surge is a flow state in which there are fluctuations in the average flow through the whole compression system. The mass flow fluctuations at surge can be that large that during a short part of the surge cycle the mass flow becomes negative. The oscillatory loading and unloading of the compressor in surge imposes transitory loads on the bearings supporting the compressor shaft and can have disastrous effects on the whole compression system. Furthermore, surge produces mechanical vibrations and is usually clearly audible. This section discusses the general features of the aerodynamic flow instability surge.

The initiation of surge can be explained by looking at the compressor map, see Figure 1.3(a), and considering the compressor and the throttle characteristic, shown by the dash-dotted and dotted line, respectively. To explain the instability of a compression system and the development of surge the model and simulation parameters as proposed by *Willems [70]*, see Appendix C.4, are used. The discussion of the initiation starts at a mass flow for which the compressor mass flow, ϕ_c, and pressure rise, ψ_c, is stable and equals the mass flow and pressure rise of the throttle valve, (Y_{T1}). At this point ($*$), the compressor flow is unconditionally stable, i.e., if a small reduction of mass flow is considered it results in an increase in the compressor pressure rise and a decrease in the throttle pressure rise. The flow will accelerate and will increase until the original equilibrium is restored.

As the throttle valve is closed, dependent on the throttle valve position, i.e., in between Y_{T2} and Y_{T3}, unstable flow situations occur. Suppose that the compressor is operating at point Y_{T3} when a small decrease in mass flow occurs; the pressure rise decreases slightly and the pressure rise of the throttle decreases substantial. In the case the compressor and throttle would be connected directly, without any volume in which flow can be accumulated, this would result in a stable operational system. Nevertheless, between the compressor and throttle there is a volume and the produced compressor pressure rise at this smaller mass flow is lower than the pressure rise the compressor produced before the small decrease in mass flow had occurred. The compressor no longer is able to work-up to the pressure of the gas in the volume. The gas through the compressor will decelerate or even accelerate backwards through the compressor, which will reduce the mass flow further, leading to an unstable flow situation.

(a) surge cycles. $-\cdot-$: steady-state compressor characteristic, $\cdots$: throttle line, ——: surge cycle, $\ast$: stable performance at Y_{T1}, $+$: stable performance at Y_{T2}

(b) time traces of pressure rise and flow coefficient. Y_{T4}=0.29
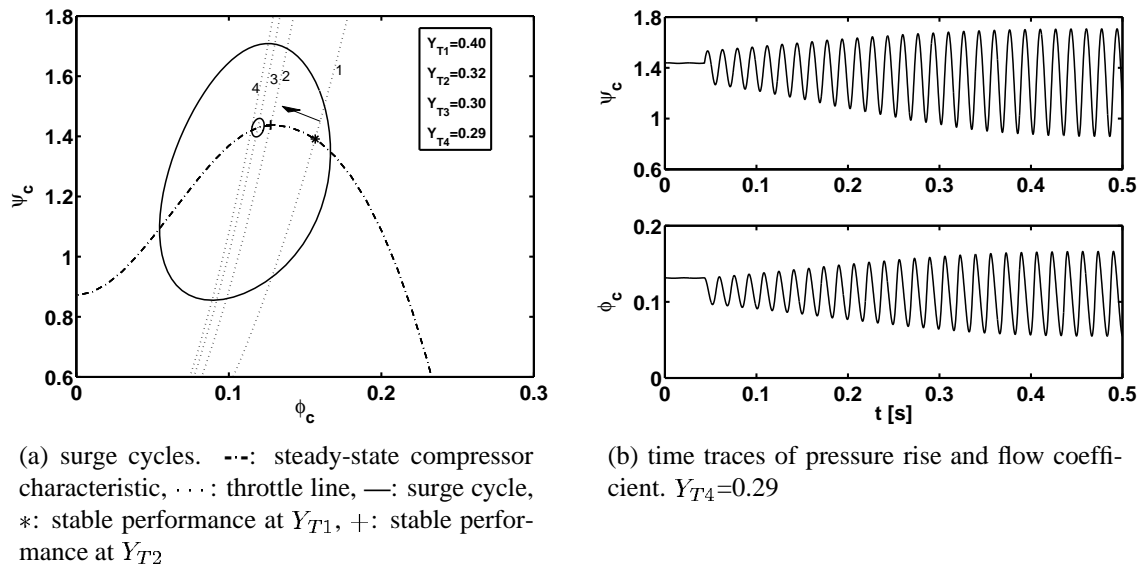
Figure 1.3: Compressor performance at different throttle valve positions. $N = 21000$ [rpm].

The development of the surge cycle, after the initiation of surge, is shown in Figure 1.3(b) for throttle valve position Y_{T4}. After some time a limit surge cycle is reached, which shape and frequency depends on the configuration of the system. Parameters that play a role are, e.g., the throttle and compressor characteristic, the volume and ductwork in between the compressor and the throttle, and the throttle valve position. Starting at the maximum pressure rise the surge cycle is formed by a counterclockwise motion in the compressor characteristic. Due to a reduction of mass flow through the compressor the pressure in the volume drops. At a certain pressure the compressor is able to work-up to the pressure in the volume again and the mass flow through the compressor will restore. Then, the pressure in the system will rise until the maximum pressure rise is reached and another surge cycle is started.

Dependent on the compression system and the operating conditions, different categories of mass flow and pressure fluctuations during surge can be distinguished, *De Jager [41]*: Mild surge, classic surge, deep surge and modified surge.

- During *mild surge* the frequency of the oscillation is close to the Helmholtz frequency, i.e.

the resonance frequency of the compressor duct and the volume connected to the compressor *[13]*, and no flow reversal occurs. A mild surge cycle is illustrated in Figure 1.4(a) (1). The mild surge frequency is independent of rotational speed or operating conditions *[66]*, *[40]*. Measurements of mild surge are performed by, e.g., *Fink et al. [23]* and *Ribi and Gyarmathy [62]*.

- *Classic surge* is characterised by larger pressure oscillations with a lower frequency, which is dependent on the rotational speed and operational condition. For this condition the dynamics become non-linear that is found in the occurrence of higher harmonics. In Figure 1.4(a) classic surge is illustrated, the compressor operating point describes for a small system volume a roughly oval cycle (2) centred around the throttle line. At a larger system volume (3) the higher harmonics are seen more clearly and the mass flow can, for a short period, become negative, *Greitzer [31]*.

- *Deep surge* is characterised by even larger pressure and mass flow oscillations, which becomes negative for part of the cycle, see Figure 1.4(b). In reversed flow the instantaneous operating point moves down a line known as the negative flow characteristic. This line defines the resistance that the rotating blades offer to flow in the reversed direction. For flow in the positive direction the operating point closely follows the steady-state characteristic, *[31]*, *[16]*. The frequency of deep surge is determined by the filling and emptying of the volume connected to the compressor and therefore depends on the system configuration.

- Finally, surge can also occur in combination with rotating stall, so called *modified surge*. Then the mass flow through the compressor is unsteady and non-axisymmetric, due to the superposition of rotating stall and entire annulus mass flow oscillations in flow direction. The effect of rotating stall on the performance of the compressor is shown in Appendix B.

(a) mild and classic surge
$V_{p1} = 3 \times 10^{-3}$ [m^3], $V_{p2} = 4 \times 10^{-3}$ [m^3]
and $V_{p3} = 2 \times 10^{-2}$ [m^3]

(b) deep surge
$V_p = 4 \times 10^{-1}$ [m^3]
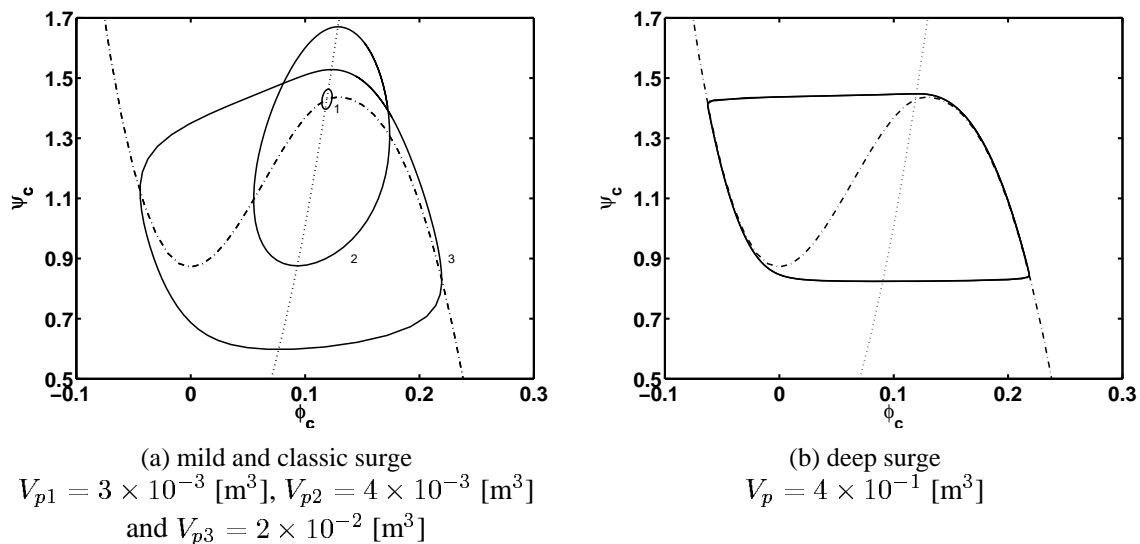
Figure 1.4: Classification of surge cycles. ‐‐: steady-state compressor characteristic, ⋯: throttle line, —: surge cycle, $N = 21000$ [rpm], $Y_T = 0.30$ [-]

Generally, the stability of a compression system is guaranteed as long as the slope of the compressor characteristic is negative. This means that the limit of dynamic stability coincides with

the maximum of the pressure rise characteristic, *[33]. Hunziker and Gyarmathy [40]* extended this argument to the individual components of the stage to indicate the components that are potentially unstable. For example, it is shown that when the mass flow is reduced, the slope of the characteristic in the diffuser throat changes with decreasing mass flow. Although, its slope is always negative, and so this component is stable, the rapid decrease of its slope with smaller mass flows causes the compression system to become unstable.

By changing the diffuser vane setting *Hunziker and Gyarmathy [40]* and *Buse et al. [8]* showed that the stability of a compression system could be influenced. Using this knowledge, *Harada [35]* implemented computer-controlled variable diffuser vanes into a centrifugal compressor and showed that the stable operational range of the compressor could be improved. An advantage of this variable geometry stabilisation is that it is based on local measurements in the diffuser and only a characteristic curve of the static pressure difference on the diffuser vane against the angle is required. On the other hand, this method introduces a relatively large efficiency penalty (*[26]*, *[24]*), and is difficult to apply to existing machines and designs. A method that can be applied to a wide range of existing machines and designs is the suppression of the instabilities by active control. In literature a considerable performance improvement up to 20% reduction in surge point mass flow is reported by applying active control to experimental set-ups (*[71]*, *[57]*). The method of active control requires a model of the compression system, i.e., the compressor and its connecting ducts, volumes and valves. In this thesis, the focus is on the modelling of the compression system including the unsteady flow dynamics in the compressor during surge.

1.4   Surge modelling

In 1976 *Greitzer [31]* observed that, although the phenomena rotating stall and surge were known to occur in compression systems, it was not yet understood what fundamental mechanisms are responsible for determining the mode of instability. Therefore, compression system models were developed. The oscillations in the system are modelled in a manner analogous to those of a Helmholtz resonator. This kind of modelling has an analogy with electrical and mechanical systems as shown by, e.g., *Dean and Young [18] and Cumpsty [13]*. The Helmholtz resonator behaviour was proposed earlier by *Emmons et al. [19]* who used a linearised analysis to examine compression instability. However, this approach is fundamentally unable to describe the large amplitude pulsations encountered during a surge cycle. To overcome this problem Greitzer developed a nonlinear mathematical model of transient compression system behaviour.

The assumptions of a Helmholtz resonator imply that all the kinetic energy of the oscillations is associated with the motion of the gas in the compressor and ducts. The potential energy of the gas is associated with the compression of the gas in the plenum. Furthermore, the assumptions are that the inlet Mach numbers are low and that the pressure rises are small compared to the ambient pressure. The gas dynamic model that is used in the analysis is shown in Figure 1.5.

The compressor and its ducting are replaced by an actuator disk, to account for the pressure rises due to the compressor, and a constant area pipe with a certain length, to account for the dynamics of the gas in the compressor duct. Similarly, the throttle is replaced by an actuator disk, across
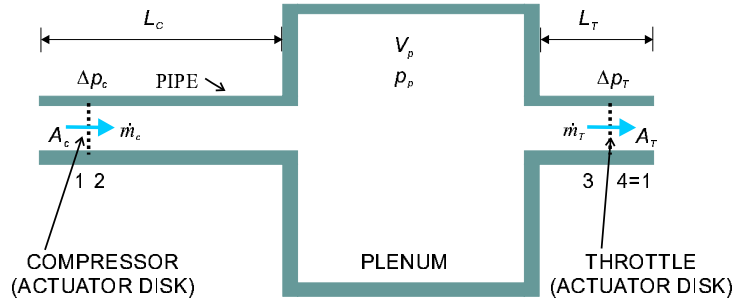
[Greitzer [31]]

Figure 1.5: Equivalent compression system used in analysis.

which the pressure drops, plus a constant area duct. The actuator disk theory assumes that a blade row can be represented by a small plane across which the mass flow is continuous, but pressure changes can be discontinuous. The flow in the ducts can be considered incompressible, since the inlet Mach number is assumed to be low, the pressure rise is small and the frequency of the oscillations associated with surge are regarded to be low. As a consequence, the mass flow at the inlet of the duct is equal to the mass flow at the outlet of duct. The details of the equations of motion as written down by *Greitzer [31]* are given in Appendix C. The modelling of the compression system with a lumped parameter approach is widely accepted in literature, and is useful in the stabilisation of rotating stall and surge by means of active control. Furthermore, it forms a basis for models dealing with long compressors, (*[9], [22]*), or compressibility in the compressor (*[54], [48]*).

The resulting equations of the dynamics of the system are Equations (C.3), (C.4), and (C.6):

$$\frac{d\dot{m}_c}{dt} = -\frac{A_c}{L_c}\left\{\Delta p - \Delta p_c\right\} \ , \tag{1.1}$$

$$\frac{d\dot{m}_T}{dt} = -\frac{A_T}{L_T}\left\{-\Delta p + \Delta p_T\right\} \ , \tag{1.2}$$

$$\frac{dp_p}{dt} = \frac{a^2}{V_p}\left\{\dot{m}_c - \dot{m}_T\right\} \ . \tag{1.3}$$

The first and second equation are the one-dimensional incompressible momentum equations for the compressor and throttle duct, respectively. Herein, is Δp the pressure rise across the duct. The loss (viscous) terms, and the contribution of the rotation in case of the compressor, are assumed to react quasi-steady to mass flow, $\dot{m}$, changes and are represented by the steady-state characteristics: Δp_c, Δp_T. The third equation describes the conservation of mass in the plenum in which an isentropic compression is assumed.

In this model the assumption that the compressor flow reacts quasi-steady to flow changes is questionable. In literature, it is shown that any lag of response of the compressor flow, due to transient flow during surge or the appearance of rotating stall, can be simulated by a first-order transient-response model (for details, see Section C.3). A drawback of the lumped parameter modelling is that the resulting model parameters (e.g., A_c, L_c, V_p) are determined by fitting the simulations to the measurements, rather than being founded on physical arguments.

1.5   Research objectives

In the lumped parameter method equivalent compressor lengths, areas, and volumes have to be provided that are not straightforward obtainable from physical dimensions of the compression system. Furthermore, a relaxation equation is necessary to obtain simulation results that are comparable with measurements. The necessary parameters are obtained by fitting the simulations to measurements. This limits the usefulness of the model for commercial use and makes the understanding and explanation of surge in physical terminology difficult. Therefore, the research is focused on developing a physical model that particularly takes into account the unsteady character of the compressor flow. In this way a model representation of the compression system is obtained with parameters that can be determined by physical arguments.

The study contains:

1. Investigation of surge in a laboratory gas turbine installation with a centrifugal compressor
   (*Chapter 2*)

2. Application of the lumped parameter model to this laboratory gas turbine installation
   (*Chapter 3*)

3. Analytical derivation of a correction term that accounts for the unsteady flow performance of the compressor during surge
   (*Chapter 4*)

4. Application of the correction term on an unsteady turbulent inlet flow in a water channel installation
   (*Chapter 5*)

5. Application of the correction term on the surging compressor flow in the laboratory gas turbine installation
   (*Chapter 6*)

A better knowledge of the physical background of surge and its initiation results in refinements to existing models, and provides new insights into methods that suppress this instability. In a companion research project: *Compressor surge control*, the practical limitations of active surge control on centrifugal compressors have been studied (*[70]*). Together with the research project into flow models for compressor surge, the companion project is part of the multi-disciplinary *Compressor Surge Project* at the Department of Mechanical Engineering, Eindhoven University of Technology, The Netherlands.

Chapter 2

Experiments on Surge

Most researchers find mild surge a non-disastrous kind of instability, since the amplitude of the oscillation and its frequency is bounded such that it cannot harm the compressor. In the case the system experiences mild surge, see e.g., *Toyama et al. [66]* and *Hunziker and Gyarmathy [40]*, the frequency of the surge corresponds to the Helmholtz frequency of the compression system and remains the same at other rotational speeds and throttle valve positions.

More effort has been put into the development of the unstable compressor flow after mild surge has started and the mass flow is throttled further. Then, the so-called classical surge or deep surge cycles are obtained, *[32]*, in which intermittent mild surge cycles as well as rotating stall can occur, *[61]*. A characteristic of deep surge cycles is shown by *Arnulfi et al. [1]* and *Meuleman et al. [49]*. As the throttle valve is closed, the surge traces show that the period with positive flow decreases and the period with negative flow increases. This results in a maximum surge frequency at an intermediate throttle valve setting, between surge inception and valve shut-off. The explanation of this behaviour is that for deep surge cycles the period with positive flow is mainly characterized by a pressure build-up to the critical pressure. Due to a smaller throughflow area, as the throttle valve is closed, this pressure build-up occurs faster. The negative flow period is characterized by the blow-down process, which occurs as a positive flow through the throttle valve and as a reverse flow through the compressor. As the throttle valve is closed the flow resistance increases, which results in a longer blow-down period.

To be able to develop and validate models that describe the dynamics in a compression system, knowledge about the dynamics is necessary. Therefore, surge is studied in a laboratory gas turbine installation. By generating surge at different rotational speeds and throttle valve settings the influence of these parameters on the surge characteristics is studied by means of pressure measurements. Furthermore, hot-wire probe measurements are performed to find out the nature of the surge.

2.1   Experimental set-up

A laboratory-scale gas turbine installation designed and instrumented by *Van Essen [20]*, is used to study surge in a centrifugal compressor. The installation is designed around a turbocharger,

as is shown in Figure 2.1. The turbocharger consists of a single stage, centrifugal compressor with a vaned diffuser and an axial turbine both mounted on the same rotational axis. Surge
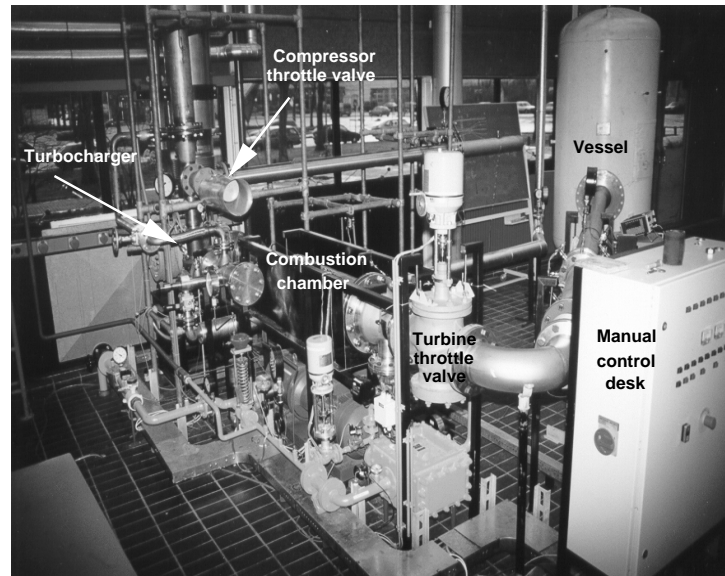
(a) photograph of the installation
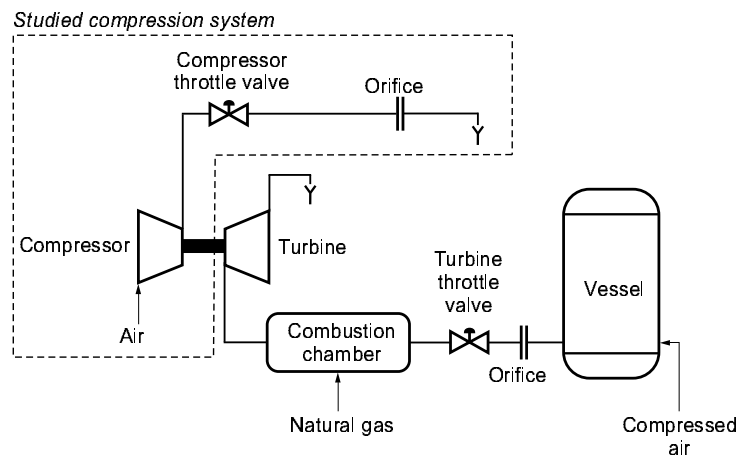
(b) scheme of the installation

Figure 2.1: Experimental set-up.

measurements are performed with a configuration in which the compressor and turbine mass flows are decoupled. The turbine that is only used to rotate the compressor under investigation, is powered by externally supplied compressed air that first flows via a combustion chamber before it expands over the turbine. Due to the rotation, air is sucked into the compressor, where it is pressurised, and is discharged via the compressor throttle valve into the atmosphere.

Since the mass flow rate of the externally supplied compressed air is limited, the maximum rotational speed in the decoupled mass flow configuration is ≈ 25000 [rpm]. Higher rotational speeds can be achieved by using the installation in the gas turbine configuration, in which the pressurised compressor flow drives the turbine. This configuration is less practical for surge measurements. First, the surge related pressure oscillations are dependent on the discharged

volume of the compressor. The smaller the discharged volume the less flow is accumulated in the volume, resulting in smaller pressure oscillations that are less harmful for the equipment. Compared to the gas turbine configuration, the decoupled mass flow configuration has a relatively small discharged volume, with which reproducible surge measurements are performed. Second, *Fink et al. [23]* and *Arnulfi et al. [1]* showed that with a small discharge volume the compressor is stable for smaller mass flows, which means that the steady-state compressor characteristics are measured up to smaller mass flows. Third, in the decoupled mass flow configuration the system can be operated at any desired (compressor) operating point, as the turbine and compressor are coupled only by a power balance. In the gas turbine configuration the number of operating points is reduced due to the extra balance of mass between the compressor and turbine. Moreover, the large mass flow fluctuations during surge cause a combustor flame-out, which makes detailed gas turbine surge experiments impossible.

measurement system

In Figure 2.2(a) the isolated compression system is shown with the location of the transducers used for the surge measurements. To determine the overall performance of the compressor, the system is equipped with a thermocouple, T_2, to measure temperature and a high-frequency-response pressure transducer, p_2, to measure static pressures at the outlet of the compressor. The rotational speed, N, of the impeller is registered by a semiconductor tachometer. With an

(a) compression system with measurement positions   (b) cross-section of the compressor
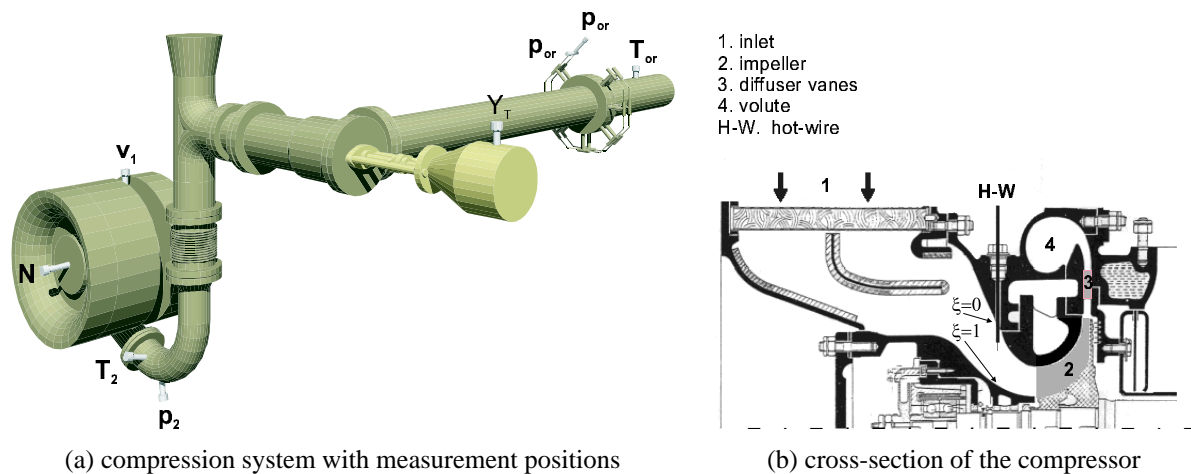
Figure 2.2: Details of the compressor set-up.

instrument orifice, $p_{or}, \Delta p_{or}, T_{or}$, the steady compressor mass flow is determined. The compressor mass flow is controlled by a throttle valve, which position is measured, Y_T. The accuracy of the measurement equipment can be found in *Van Essen [21]*. All transducer signals are connected to a 'NATIONAL INSTRUMENT' data acquisition Plug-in board in the measurement computer. A 'LABVIEW' based data acquisition system is used to measure, monitor and store all the available measurement signals.

Measurements of the transients into and during fully-developed surge consist basically of data

from the high-frequency-response pressure probe at the outlet of the compressor, the throttle valve position sensor and the rotational speed transducer. The sample rate of the transient measurements was 200 [Hz]. Nevertheless, information of the unsteady mass flow cannot be determined from the instrumented orifice, since it is only capable of measuring steady flow. To obtain some information about the flow velocity, v_1, a single hot-wire probe is used at 35 [mm] upstream of the inlet of the compressor duct, see Figure 2.2(b). The position of the hot-wire probe is measured from the casing wall ($\xi = 0$ [-]). The maximum position is $\xi = 1$ [-] at the inner wall of the inlet. Further details about the hot-wire measurements can be found in Appendix D and in *Maas [47]*. Measurements including the hot-wire probe are performed at a 1000 [Hz] sampling rate.

2.2 Compressor characteristic

Measurements are carried out on a single-stage centrifugal compressor, with an unshrouded, radial ending impeller without backsweep and a diffuser with straight vanes, see Figure 2.2(b). The compressor is part of a turbocharger (BBC VTR 160L). Relevant geometrical compressor parameters can be found in Table 2.1.

Table 2.1: Geometrical compressor parameters.

Impeller				Diffuser			
number of blades	Z	20	[-]	number of vanes	z	45	[-]
inducer inlet diameter (casing)	$d_{1,a}$	0.106	[m]	vanes inlet diameter	d_3	0.215	[m]
inducer inlet diameter (hub)	$d_{1,h}$	0.054	[m]	vanes outlet diameter	d_4	0.258	[m]
impeller diameter	d_2	0.180	[m]				
impeller exit width	b_2	0.007	[m]				

Steady-state measurements are performed to determine the overall performance of the compressor and to find the minimum mass flow for which steady compression was assured. In Figure 2.3(a) the pressure ratio of the outlet pressure, p_2, and the inlet pressure, p_0, of the compressor versus the mass flow, $\dot{m}_c$, is shown for three rotational speeds, N. Surge is determined experimentally by detecting the initiation of surge. Then the compressor is operated close to the surge point such that no surge was incepted. In this way the minimum stable mass flow was measured using the orifice mass flow.

In Figure 2.3(b) the nondimensional compressor map is shown. The definition of the nondimensional pressure rise (Equation (A.1)) and mass flow (Equation (A.3)) are:

$$\psi_c = \frac{\Delta p_c}{\frac{1}{2}\rho_0 U_t^2} \qquad \text{dimensionless pressure rise}$$

$$\phi_c = \frac{\dot{m}_c}{\rho_0 A_c U_t} \qquad \text{dimensionless mass flow}$$

in which Δp_c is the pressure difference between the outlet pressure, p_2, and the inlet pressure, p_0, ρ_0 is the atmospheric density, A_c is the compressor throughflow area, and U_t is the impeller

tip speed. The atmospheric density, ρ_0, is determined from the ideal gas law,

$$\rho_0 = \frac{p_0}{RT_0}. \tag{2.1}$$

(The atmospheric density is different from the one used by *Willems [70]* who took it to be constant, $\rho_0 = 1.2$ [kg/m^3]). The atmospheric pressure, p_0, and temperature, T_0, are determined at the beginning of every measurement session. The compressor throughflow area is defined as:

$$A_c = \pi \frac{d_{1,a}^2 - d_{1,h}^2}{4} = 6.53 \; 10^{-3} \; [\text{m}^2] \,, \tag{2.2}$$

and the impeller tip speed as:

$$U_t = \pi d_2 \frac{N}{60} \,.$$

The nondimensional compressor map shows that the rotational speed curves nearly coincide. The critical flow coefficient at which surge is initiated is not unique. In *Meuleman [52]* it is shown that the critical flow coefficient increases with increasing rotational speed.

(a) dimensional   (b) nondimensional
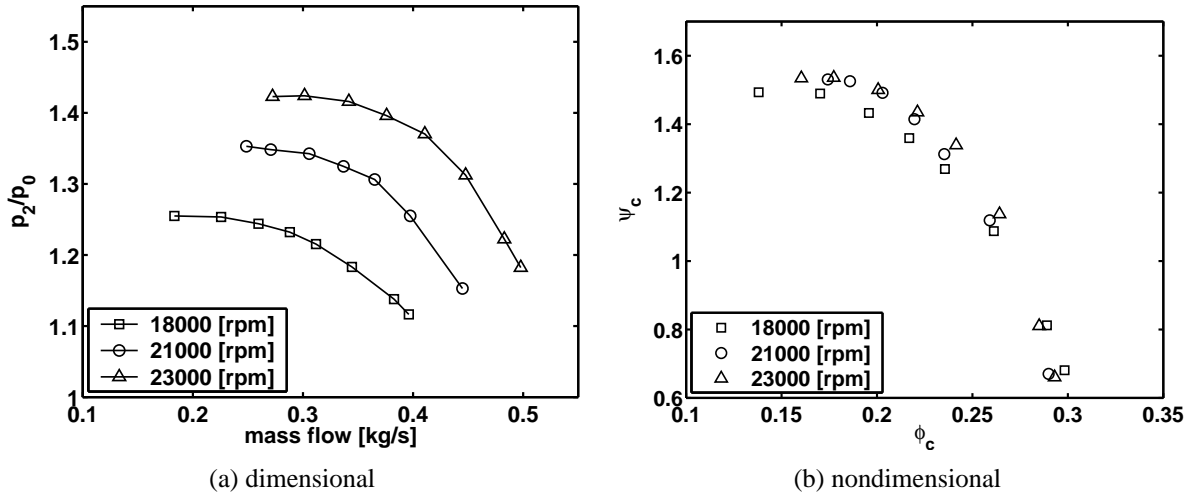
Figure 2.3: Measured compressor map.

2.3 Throttle valve characteristic

The compressor mass flow is controlled by a throttle valve. Since the relation between the mass flow through the throttle and the opening area of the throttle is linear, the mass flow is proportional to the valve position, Y_T, (*Van Essen [21]*). The position of the valve is measured by a potentiometer, which gives a measure for the opening area of the valve. For subsonic flow conditions the throttle valve mass flow is assumed to be given by:

$$\phi_T = c_T \, Y_T \, \sqrt{\psi_T} \,. \tag{2.3}$$

Herein, a nondimensional throttle valve mass flow, ϕ_T, and nondimensional throttle valve pressure rise, ψ_T, are used. Both nondimensionalised by relevant compressor parameters (see Equations (A.1) and (A.3)). Furthermore, the throttle valve position is nondimensionalised by its maximum position:

$$
\begin{aligned}
\phi_T &= \frac{\dot{m}_T}{\rho_0 A_c U_t} && \text{dimensionless mass flow} \\
\psi_T &= \frac{\Delta p_T}{\frac{1}{2}\rho_0 U_t^2} && \text{dimensionless pressure rise} \\
Y_T &= \frac{y_T}{y_{T\,max}} && \text{dimensionless throttle valve position}
\end{aligned}
$$

The pressure difference Δp_T of the throttle is defined as the difference between the inlet pressure, p_2, and the outlet pressure, p_0, of the throttle. The geometrical parameters of the impeller can be found in Table 2.1.

The dimensionless throttle valve parameter, c_T, is determined from Equation (2.3) with use of the measured mass flow, rotational speed, pressure rise, and throttle valve position. In Figure 2.4(a) the ratio $\phi_T/\sqrt{\psi_T}$ is shown versus the measured dimensionless throttle valve position Y_T. As can be seen, the ratio $\phi_T/\sqrt{\psi_T}$ is linear in Y_T, so c_T is a constant. The best fit of c_T in a least square sense is made for the measurements for $Y_T < 0.8$. Then $c_T = 0.406$. Figure 2.4(a) shows that $\phi_T/\sqrt{\psi_T}$ can accurately be described by the linear approximation, as long as $Y_T \leq 0.8$. In addition, c_T, is used to estimate the nondimensional mass flow, ϕ_T, see Equation (2.3). This gives reasonable results, as shown in Figure 2.4(b). However, care should be taken for mass flows $\phi_T < 0.15$ and $\phi_T > 0.28$.

(a) c_T determined from measurement

(b) measured and estimated ϕ_T
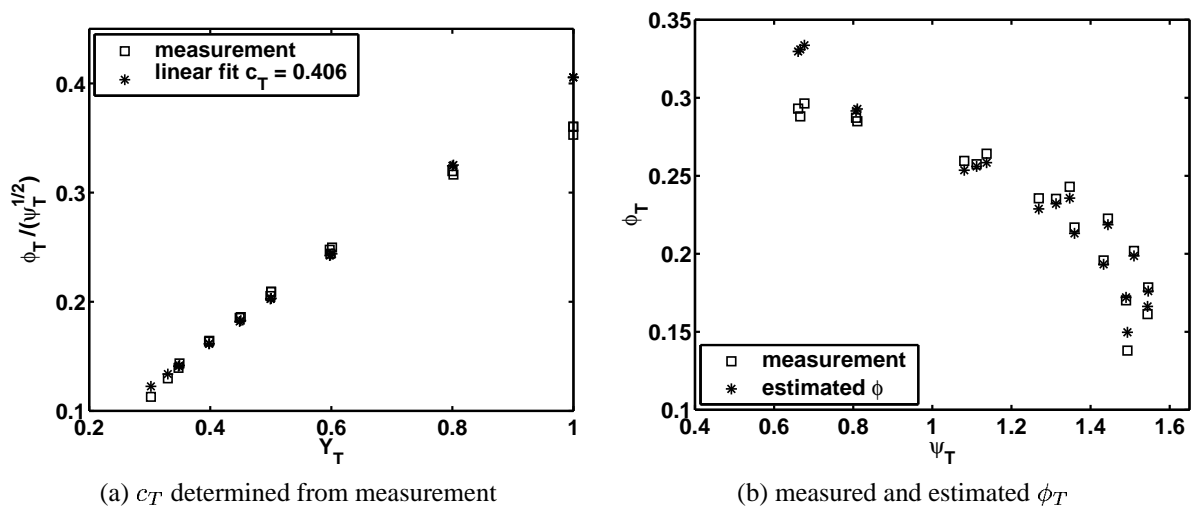
Figure 2.4: Dimensionless throttle valve characteristic.

2.4 Surge development measurements

Surge initiation measurements are performed to determine the stability of the compressor system. In Figure 2.5 the initiation of surge is shown. By closing the throttle valve, Y_T, the mass flow is decreased, and surge is initiated as can be seen in the pressure ratio. The initiation of surge is defined as the point at which the amplitude of the pressure trace starts to grow and a distinct oscillation frequency appears, which is pointed out in the lower right plot. Upon surge initiation a surge development zone B is recognized in which the surge develops to fully-developed surge that occurs in zone C. Due to a constant shaft power, the reduction of mass flow results in a slight increase of the mean rotational speed, N. The figure also shows that while the throttle valve is kept at a certain value, the rotational speed still increases due to inertia of the rotating parts.

(a) throttle valve

(b) rotational speed

(c) pressure ratio

(d) detailed pressure ratio at surge initiation
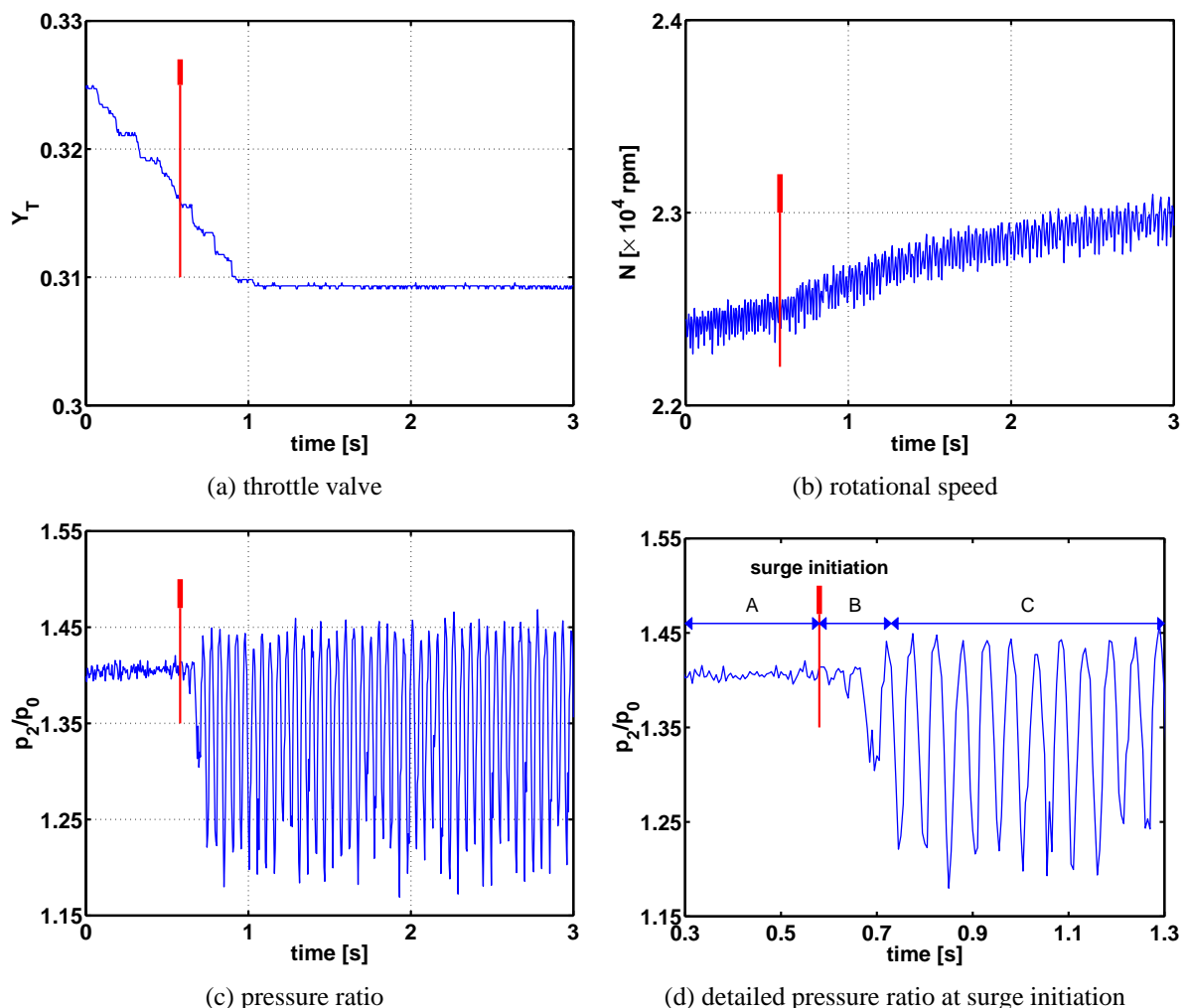
Figure 2.5: System signals as surge is incepted. A: normal operation, B: surge development, C: fully-developed surge

The development of the surge is sketched in a compressor map in Figure 2.6(a). As the throttle

is closed the compressor performance follows the steady-state characteristic (for simplicity a constant rotational speed scenario is followed). At a certain pressure ratio the surge limit line is reached and a surge cycle is initiated. Before reaching the limit cycle some smaller cycles occur, as is seen in the pressure ratio in the B-zone of Figure 2.5(d).

(a) sketch of the surge cycle (b) surge initiation line
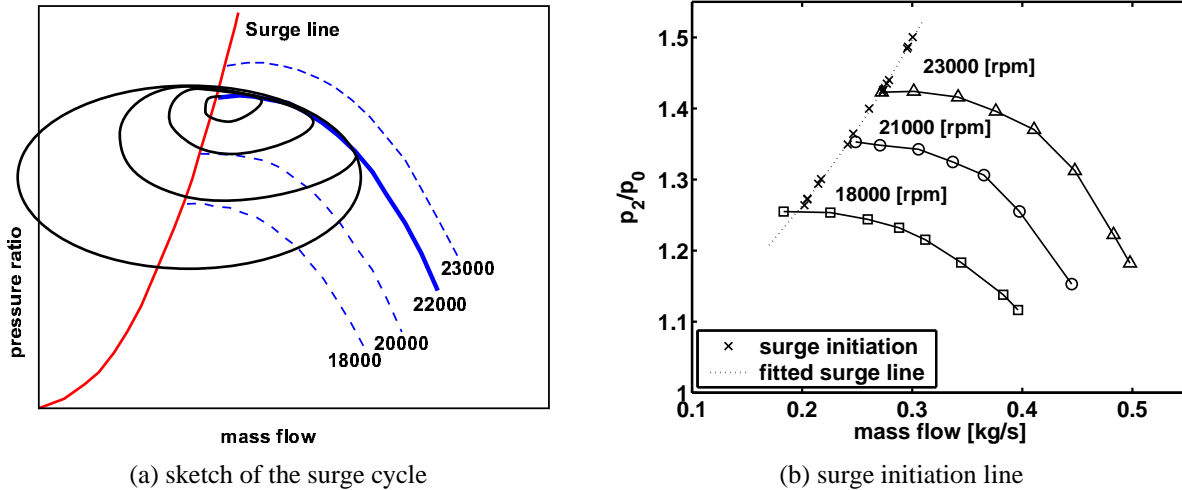
Figure 2.6: Stability of the compression system in the compressor map.

The stability line of the compressor is determined also from the transient measurements. Since for transient measurements into surge the instrumented orifice cannot be used for reliable mass flow measurements, the relation between the throttle valve position and the mass flow, Equation (2.3), is used to determine the surge initiation mass flow. First, for different rotational speeds the surge initiation points, i.e. pressure ratio, rotational speed and throttle valve position at initiation, are determined. Then the mass flow is calculated. In Figure 2.6(b) the surge initiation points are shown in the compressor map. As can be seen, the determination of the mass flow via the throttle valve position is reasonable, since the surge initiation points are close to the lowest measured steady mass flows. Only the initiation of the curve with rotational speed $N = 18000$ [rpm] shows an overestimation of the mass flow determined via the transient measurements. This is due to the fact that the fit that is used to determine the transient mass flow is not applicable for flow coefficient $\phi_c < 0.15$.

For this compression system, the development of surge after the surge initiation point as described above, only applies for rotational speeds larger than ≈ 19000 [rpm]. For rotational speeds smaller than ≈ 19000 [rpm], prior to fully developed surge, a drop in compressor pressure ratio is measured, as shown in Figure 2.7. This is a characteristic of abrupt rotating stall, see Appendix B. After the drop in pressure ratio, in zone B, a distinct frequency is found, which indicates that the system is not in a stable operating point but rather experiences a surge around the assumed rotating stall characteristic. Furthermore, it develops to fully-developed surge, as shown in zone C. The stability of the present compression system is explained by assuming that there exists a rotating stall limit line that is specific for the compressor, and a surge limit line that is specific for the whole compression system. For $N > 19000$ [rpm], sketched in Figure 2.6(a), reduction of mass flow leads to the surge limit. Due to a quick change of mass flow and pressure a fully-developed surge is obtained without any sign of (abrupt) rotating stall. For

$N < 19000$ [rpm], sketched in Figure 2.8, a reduction of mass flow first results in an abrupt rotating stall. Since the rotating stall limit and the surge limit are very close, the system does not operate stable on the rotating stall characteristic. The unstable flow eventually develops to a fully-developed surge.

(a) sudden drop in pressure ratio

(b) detail of the drop in pressure ratio
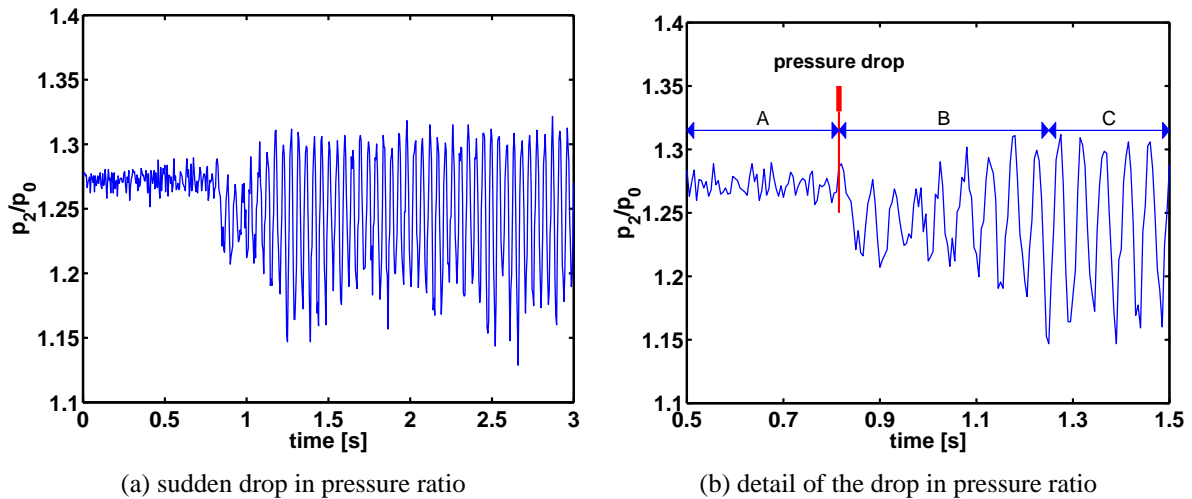
Figure 2.7: System signals as rotating stall and surge is incepted. $N = 18700$ [rpm], A: normal operation, B: pressure drop and surge development, C: fully-developed surge
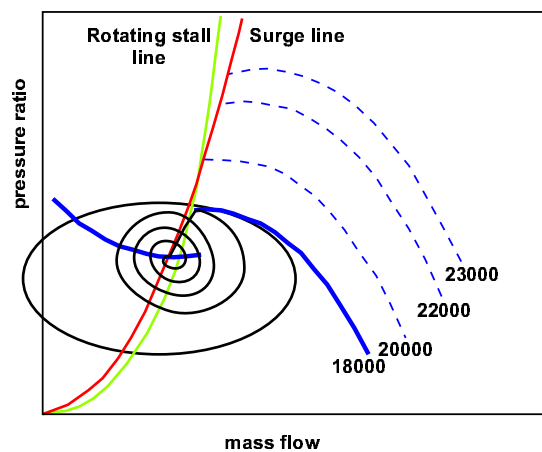
Figure 2.8: Sketch of the surge cycle preceded by rotating stall in the compressor map.

Willems [70] was able to stabilise the investigated compression system for surge by one-sided surge control. For rotational speeds smaller than ≈ 19000 [rpm] the stabilised system appeared to operate stable on the rotating stall characteristic. Information about the presence of rotating stall cells at initiation and during fully-developed surge is lacking, as there are no pressure sensors placed around the circumference of the compressor and the sample frequency of 200 [Hz] is too low to acquire any information on the rotating stall frequency, which is of the order of the rotational speed.

2.5 Fully-developed surge characteristics

Fully-developed surge data is collected for different rotational speeds and throttle valve settings. The procedure of data collection is that the compressor was put into surge by closing the throttle valve to a determined throttle valve setting. After the rotational speed is settled data is acquired. Therefore, in this section the settled rotational speed belonging to the throttle valve setting in surge is used to discuss the dependence of the surge characteristics on the rotational speed. The surge frequency is determined from a spectral analysis of the fully-developed pressure oscillations. In this way the computed surge frequency is within 0.5 [Hz] of the real frequency. In Figure 2.9 the resulting surge frequency is shown versus the throttle valve position and rotational speed (*[52]*). As can be seen, the surge frequency shows a relation with the throttle valve position, see Figure 2.9(a). The surge frequency increases as the throttle valve is closed. Furthermore, a slight influence of the rotational speed is seen. For a certain throttle valve position, the surge frequency decreases slightly as the rotational speed increases, this was also found by *Arnulfi et al. [1]*, *Jin et al. [42]*, and *Hansen et al. [34]*. In Figure 2.9(b) it is seen that the surge frequency is not directly related to the rotational speed.

(a) versus throttle valve position   (b) versus rotational speed
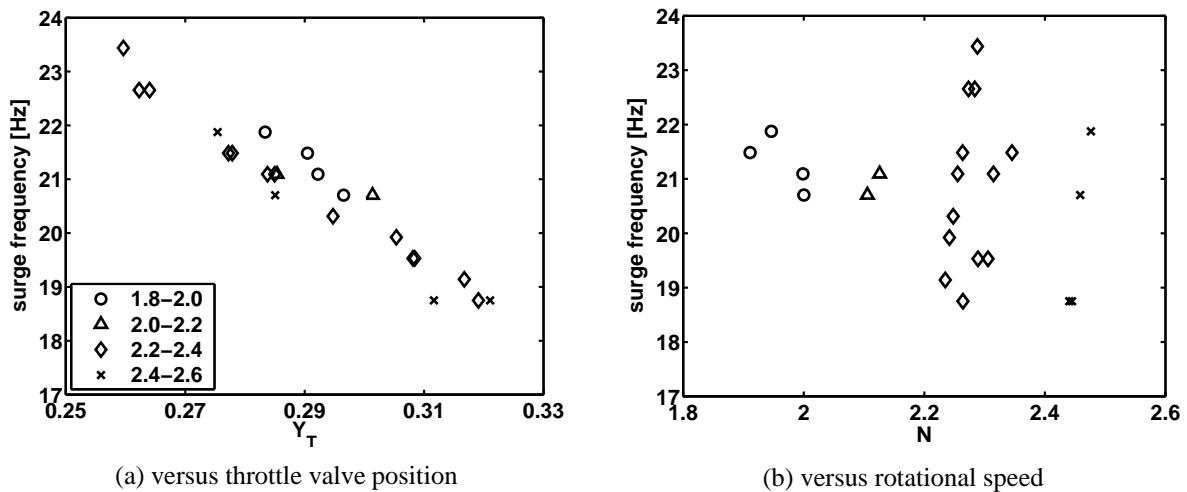
Figure 2.9: Surge frequency for different rotational speeds [$\times 10^4$ rpm].

Figure 2.10 shows for two rotational speeds the pressure signals belonging to two throttle valve positions. The time is nondimensionalised with the surge frequency. As can be seen, no distinct difference between the signals is found. This means that for this compression system a smaller throttle opening results in a proportional reduction of the pressurization and pressure drop period.

In Figure 2.11 the mean maximum and mean minimum nondimensional pressure rise versus the rotational speed and throttle valve position are shown (*[51]*). As can be seen, the maximum pressure rise coefficient seems to be virtually constant. A detailed study showed that there is a small increase of the maximum pressure rise for a decreasing throttle valve position. The scatter in the minimum pressure rise coefficient is larger than for the maximum pressure rise coefficient. This is mainly due to the sharp pressure signal at the minimum pressure, which is not always sampled at its minimum value. The pressure rise coefficients at initiation of surge are

(a) $N = 22600$ [rpm]   (b) $N = 24500$ [rpm]
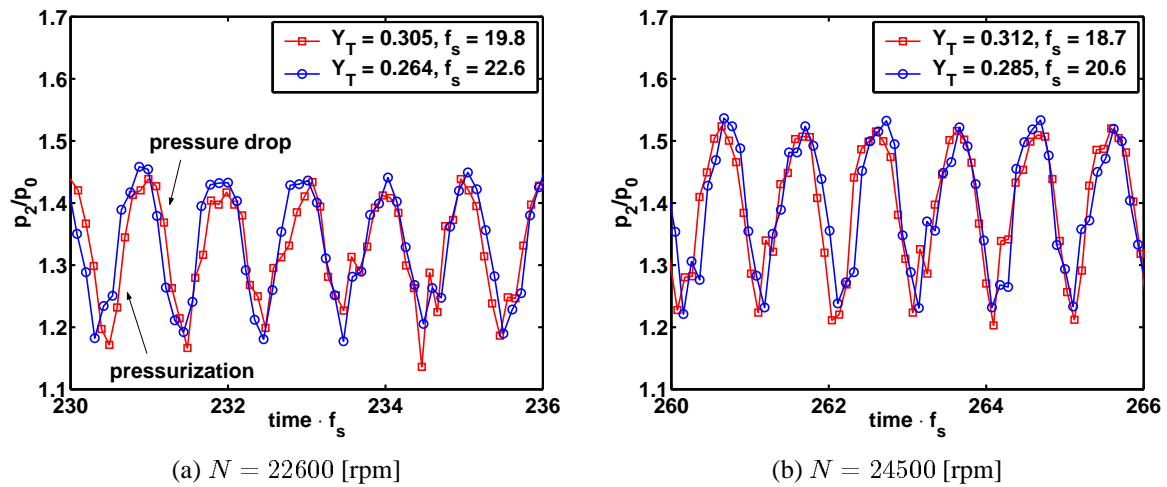
Figure 2.10: Pressure ratio versus the nondimensional time for different throttle valve settings.

also shown in Figure 2.11. As can be seen, the maximum pressure rise during fully-developed surge is larger than the pressure rise at initiation of surge.

(a) versus rotational speed   (b) versus throttle valve position
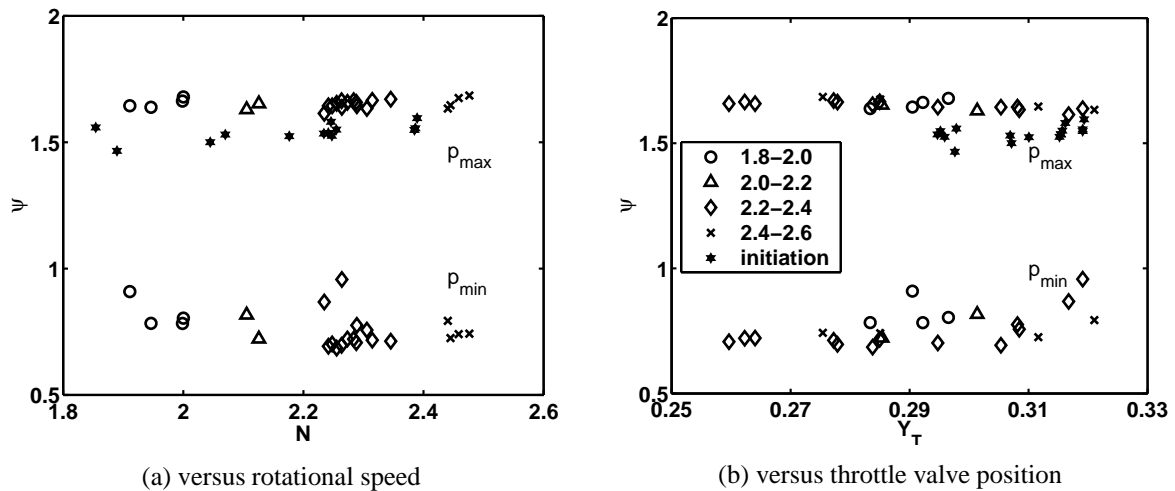
Figure 2.11: Maximum and minimum compressor pressure during fully-developed surge for different rotational speeds [$\times 10^4$ rpm].

Both the pressure-rise period and pressure-drop period are shortened as the throttle valve is closed. This results in an increase of the surge frequency. A decrease of the pressure rise period is expected, since due to a smaller throughflow area the pressure build-up occurs faster. On the other hand, the pressure drop period is expected to increase, since due to the increased flow resistance of a smaller throttle valve setting the pressure drop occurs slower. Apparently, in this system, the pressure drop period is less determined by the resistance of the throttle valve. Rather by the resistance of the impeller, which is independent of the throttle valve setting. This could also explain the nearly constant pressure rise of the surge cycle for different throttle valve settings. If the throttle valve determines the flow resistance, the pressure rise becomes higher as the throttle valve is closed. In this system the pressure drop period seems to be brought about

by mass flow through the throttle valve as well as through the compressor. Therefore, a period of reversed flow through the compressor is expected to occur.

2.6   Pressure-flow relation at fully-developed surge

To obtain some information about the flow during surge, velocity measurements at different positions from the casing at the inlet of the impeller are performed at $N \approx 21100$ [rpm] and $Y_T \approx 0.30$. In this section, the presented data is filtered with a low-pass filter with a cut-off frequency of 400 [Hz] to obtain a clearer view on the pressure and velocity trace during surge. In Figure 2.12 a detail of the pressure ratio and velocity for $\xi = 0.73$ are shown in one figure. The position, ξ, is the ratio between the distance from the casing wall and the location of the inner wall. Starting from time $t = 1$ [s] a decrease of the velocity is seen, while the pressure ratio increases. As the maximum pressure ratio is obtained the velocity shows a sudden drop. Thereafter, the velocity signal fluctuates to at least the time at which the minimum pressure ratio is obtained. At $t \approx 1.05$ [s] the cycle is repeated.
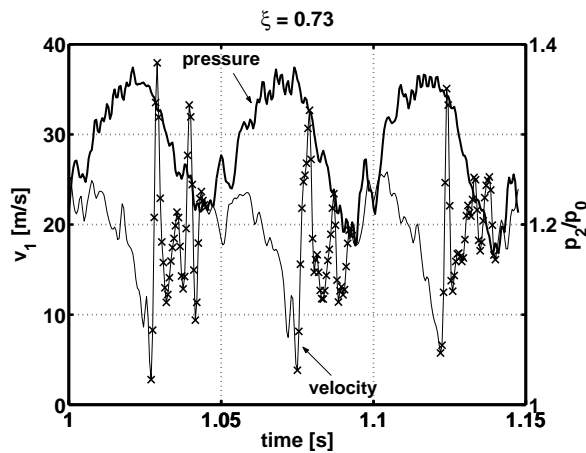
Figure 2.12: Detailed pressure ratio and velocity. $\xi = 0.73$, $N = 21100$ [rpm], $Y_T = 0.30$, $\times$: uncertain measurement

The periods with the large fluctuations of the velocity are marked ($\times$). In these regions the velocity measurements are uncertain. The distorted measurement can be caused by the existence of three-dimensional flow at the inlet of the impeller which causes cooling of the wire other than perpendicular to it and mechanical vibrations of the probe and wire during the surge cycle. The sudden velocity drop at the beginning of the fluctuations might indicate the turning of the flow from forward to reversed flow. In the case of flow reversal, the flow comes from the impeller and has a swirl that cools the wire. Furthermore, the wire would be confronted with a wake-jet flow which could initiate vibration of the wire and probe. Both result in a larger measured velocity. On the other hand, the flow coming from the outlet of the compressor is much warmer, $T \approx 350$ [K], which would cool the wire less than forward flow at ambient temperature. This would result in a smaller measured velocity. A second sudden velocity drop at the end of the fluctuations, which indicates that the flow has turned to forward flow again, is less visible. Therefore, it is not clear whether flow reversal takes place during surge in this compression

system. Nevertheless, the large fluctuation period are caused by a change in the flow field that seems to be highly distorted during this period and is not yet understood.

In Figure 2.13 signals of the pressure ratio and velocity are shown for four hot-wire probe positions. The procedure of operation was that the compressor was operated at a stable operation
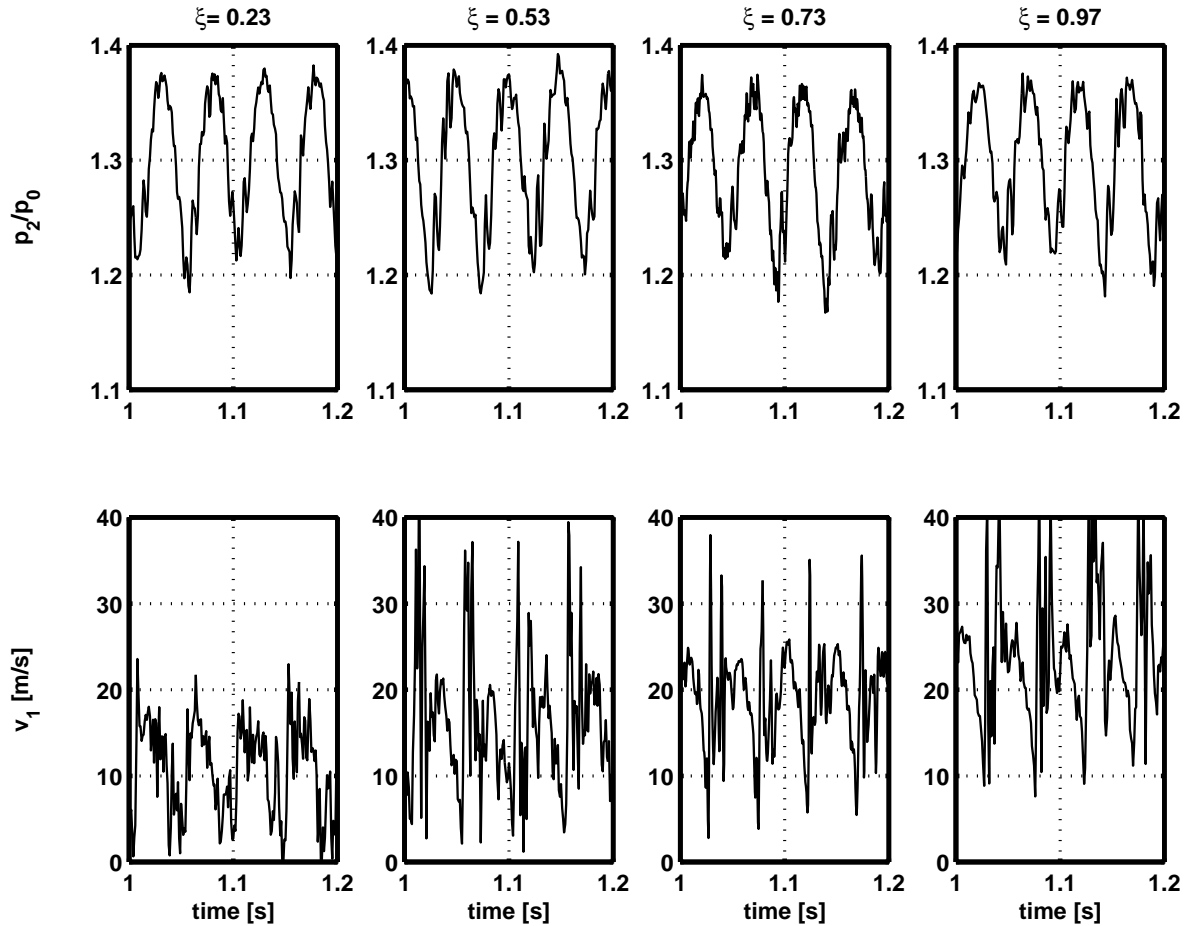
Figure 2.13: Pressure ratio and velocity for different radial positions. $\xi = 0$ casing wall, $\xi = 1$ inner wall, $N \approx 21100$ [rpm], $Y_T = 0.30$

point. The hot-wire probe was positioned, the compressor was put into surge and data was acquired. Hereafter, the compressor was again operated in a stable operation point and the hot-wire probe was repositioned. In this way the reproducibility of surge is shown in the pressure ratio data. As can be seen, the pressure signals are quite similar. The pressure signal is periodic with a surge frequency of 20.5 [Hz].

Looking at the velocity trace in detail it is seen that at least for $\xi \geq 0.53$ there exists a fast fluctuating part, which is mainly recognized by large velocity peaks beyond 30 [m/s], and a smoother part, which is mainly characterized by a slow drop in velocity. For $\xi = 0.23$ these peaks are less pronounced. Here, the velocity decreases slowly, while the pressure ratio increases. The two sudden drops of the velocity (only one drop is seen for $\xi \geq 0.53$) as the maximum and minimum pressure ratios are obtained, might indicate the reversal of the flow. First, from forward to backward flow, and second, the recovery of the mass flow, from backward to forward flow.

In Figure 2.14 a velocity profile of phase ensemble averaged surge data is shown for the period in which a decreasing velocity takes place. The lines are separated by $\Delta t = 0.003$ [s]. It is seen that the velocity is larger as ξ is larger, which is an effect of the curved inlet duct and the way the hot-wire probe is traversed.
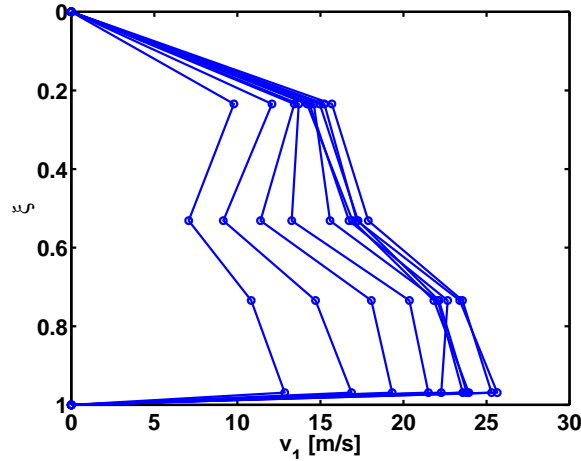
Figure 2.14: Velocity profile determined from surge measurements at different positions. $N \approx 21100$ [rpm], $Y_T = 0.30$, $\Delta t = 0.003$ [s]

To be able to compare the velocity data with the measured steady compressor mass flow, the velocity measured at one position ξ has to be multiplied by a factor $\mathcal{A}$, which in the case the velocity is uniform over the height of the inlet, would represent the product of the density and the throughflow area of the compressor, $\mathcal{A}_{\text{uniform}} = \rho A_c = 0.008$ [kg/m]. Since the velocity is not uniform the factor is determined using steady-state measurements. The mass flow measured with the orifice is correlated to the measured velocity at position $\xi = 0.66$. In Figure 2.15 it is seen that the resulting factor $\mathcal{A}$ depends on mass flow and rotational speed. Generally, factor $\mathcal{A}$ is larger than $\mathcal{A}_{\text{uniform}}$, which suggests that the measured velocity is smaller than it would be in a uniform velocity case. Furthermore, this difference becomes larger for smaller mass flows. In the next discussion, the factor is determined for each rotational speed at the lowest steady measured mass flow. Therefore, the mass flow of the surge cycle only gives an impression of the unsteady mass flow rather than the real one. This should be kept in mind during the discussion on the surge cycle.

To get an impression of the measured surge cycle in a compressor characteristic way, the signals at $\xi = 0.66$ are separated in a valid part, basically for which the pressure ratio increases from low to high, and an invalid part, for which the large hot-wire fluctuations are found and the pressure ratio is dropping. An example of separation of the signals is shown in Figure 2.16(a). In Figure 2.16(b) fifty valid parts of the surge cycle are plotted for $N = 20100$ [rpm] and $Y_T = 0.28$. Furthermore, a phase average is determined and plotted with squares. Figure 2.17, for $N = 20100$ [rpm] and $Y_T = 0.26$, and Figure 2.18, for $N = 23200$ [rpm] and $Y_T = 0.29$, are compared with Figure 2.16.

The valid part of the surge cycle can be divided in three areas, i.e.:

1. mass flow recovery, at low pressure ratio
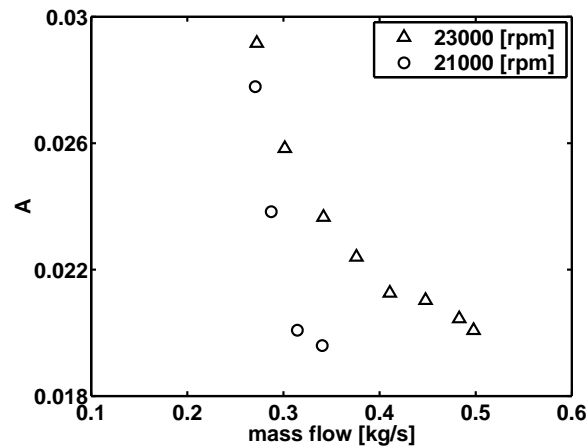
Figure 2.15: Factor $\mathcal{A}$ versus the mass flow. $\xi = 0.66$

2. pressure build-up, while the mass flow decreases

3. pressure and mass flow beyond the surge line

In the first area, the mass flow recovers while the pressure increases. Especially, in Figure 2.17(b) for a smaller throttle valve setting and in Figure 2.18(b) for a larger rotational speed a local maximum pressure is obtained. After this maximum the pressure ratio shows a small drop before it enters the second area. To understand this part of the surge cycle, detailed measurements in the compressor are necessary. For example, it could be caused by a temporary appearance of rotating stall as in *[1]* and *[3]* in which a rotating stall on the low pressure portion of the surge cycle was observed.

In the second area, a gradual rise of pressure and decrease of mass flow is seen. Due to the uncertainty in the mass flow trace it is not obvious whether the steady-state characteristic is followed. For $N = 23200$ [rpm] the $\mathcal{A}$ seems to be chosen well since the lowest steady measured mass flow coincides with part of the surge cycle.

In the third area, the mass flow decreases past the surge line to very small values. The pressure ratio is rather constant in this area and larger than the maximum steady measured pressure (See also Figure 2.11). This agrees with what was measured by *Arnulfi et al. [1]*, *Fink et al. [23]*, and *Hansen et al. [34]*. The transition from the second to the third area is quite smooth for $N = 20100$ [rpm], but a small pressure drop and thereafter a sudden pressure increase is seen for $N = 23200$ [rpm].
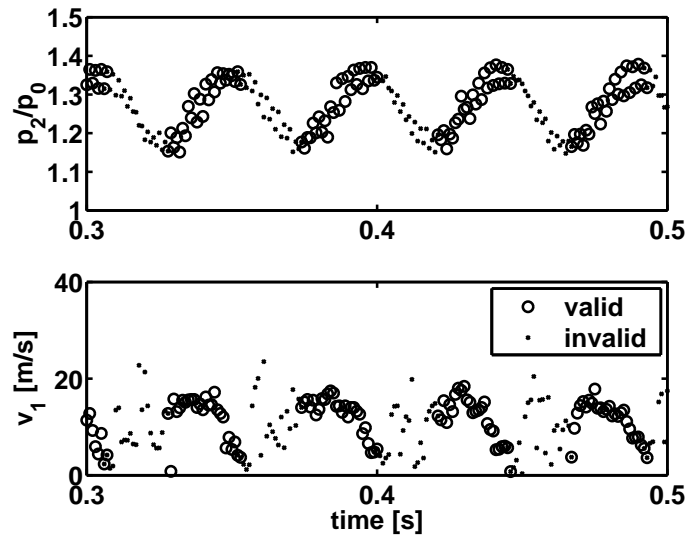
(a) indication of the valid and invalid pressure and velocity time traces
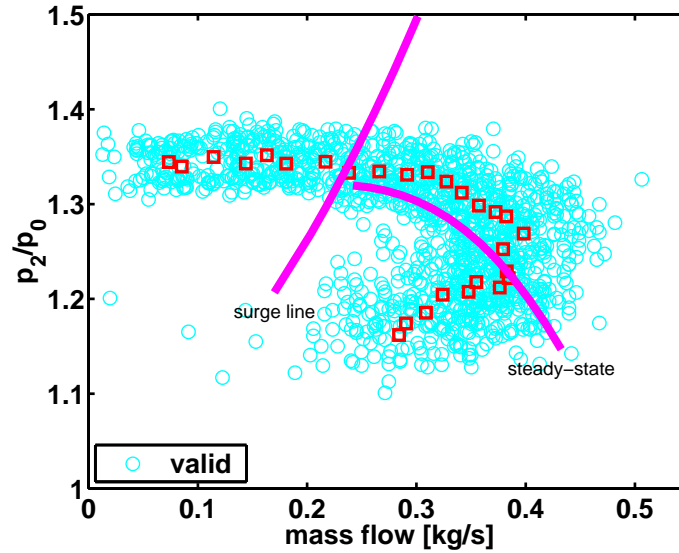
(b) surge in compressor map. ○: valid parts of 50 surge cycles, □: mean values, –: steady-state characteristic

Figure 2.16: Impression of the measured surge cycle. $\xi = 0.66$, $N = 20100$ [rpm], $Y_T = 0.28$, $\mathcal{A} = 0.024$ [kg/m]
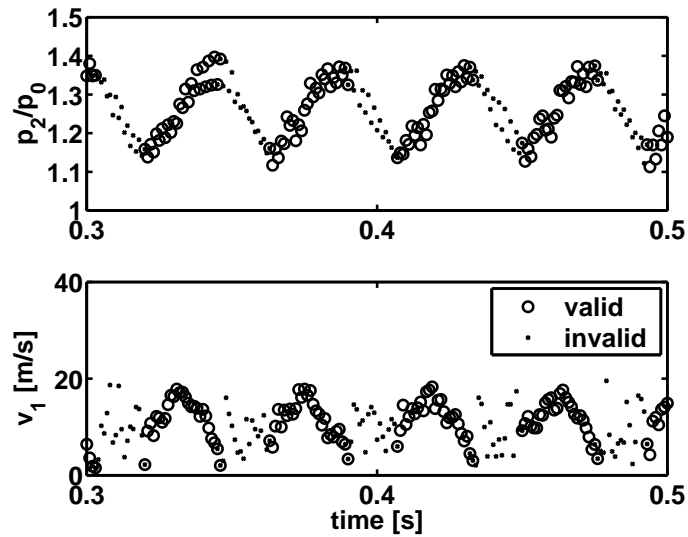
(a) indication of the valid and invalid pressure and velocity time traces
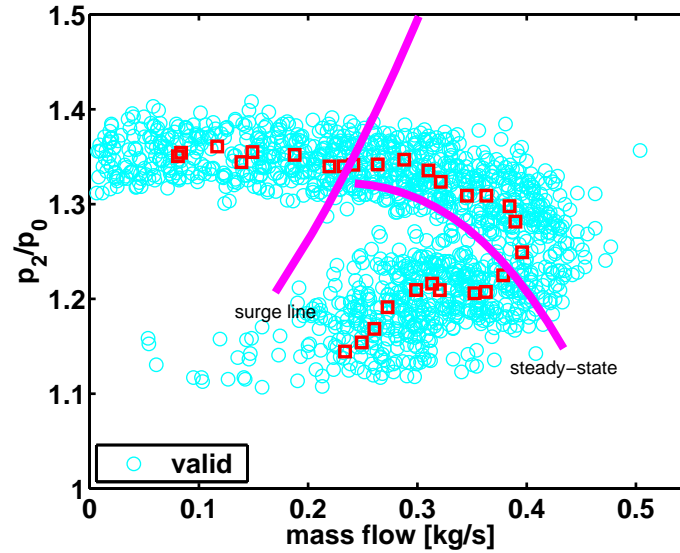
(b) surge in compressor map. ∘: valid parts of 50 surge cycles, □: mean values, –: steady-state characteristic

Figure 2.17: Impression of the measured surge cycle. $\xi = 0.66$, $N = 20100$ [rpm], $Y_T = 0.26$, $\mathcal{A} = 0.024$ [kg/m]
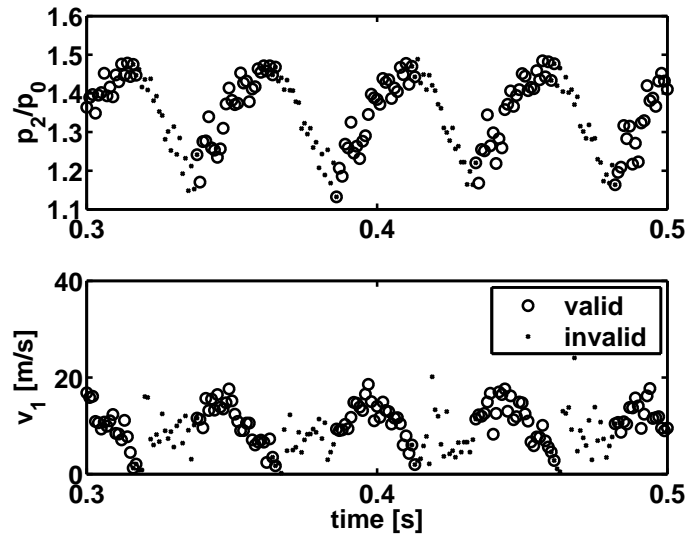
(a) indication of the valid and invalid pressure and velocity
time traces
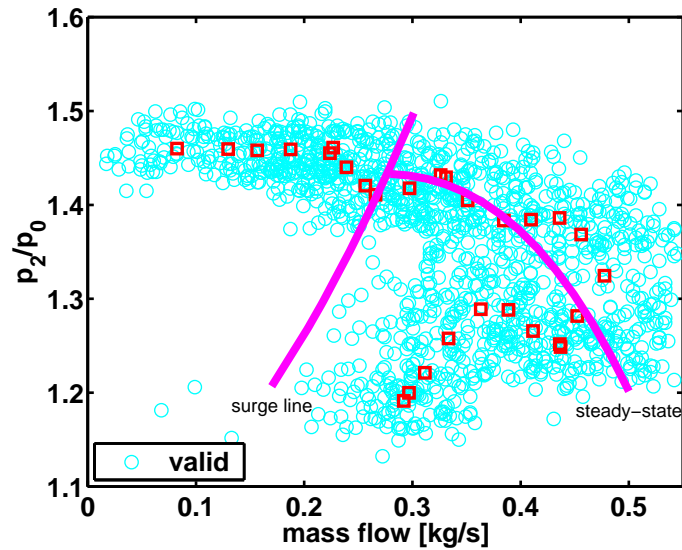
(b) surge in compressor map. ○: valid parts of 50 surge cy-
cles, □: mean values, –: steady-state characteristic

Figure 2.18: Impression of the measured surge cycle. $\xi = 0.66$, $N = 23200$ [rpm], $Y_T = 0.29$,
$\mathcal{A} = 0.029$ [kg/m]

2.7   Discussion

In this chapter surge is studied in a laboratory gas turbine installation. With pressure measurements at the outlet of the compressor surge was measured at different rotational speeds and throttle valve settings. The influence of these parameters on the surge characteristics is studied. Furthermore, hot-wire probe measurements are performed to find out the nature of surge.

The surge frequency depends on the operational condition of the system. Since for mild surge, the frequency of the surge would correspond to the Helmholtz frequency of the compression system and remain the same at other rotational speeds and throttle valve positions, this system experiences classic or deep surge.

At the inlet of the compressor hot-wire measurements are performed. Unfortunately, no definite information on the occurrence of a change in flow direction is obtained. Nevertheless, by correlating the velocity to the mass flow an impression of the positive flow period of the surge cycle is obtained.

With the pressure measurements at the outlet of the compressor the characteristic parameters of the surge cycle in the compression system are obtained. These are the surge frequency and the pressure rise amplitudes that are used to evaluate the simulated surge cycles that are discussed in the next chapter and in Chapter 6. Furthermore, the impression of the period with positive flow in the surge cycle that is determined from the measurement is used to see whether the shape of the simulated surge cycle approaches the measured shape.

Chapter 3

Compression system modelling

In this chapter the lumped parameter model as discussed in Chapter 1.4 and Appendix C is used to simulate surge in the experimental system. It is found that there are many uncertainties in the model. First, the steady-state performance of the compressor has to be known in a region of negative and positive mass flows. Only part of this region, for which the system is stable, is measured. Second, the geometry data is difficult to determine straight forward from the system due to a lumped parameter concept. Third, the question arises whether a quasi-steady compressor characteristic can be applied in the frequency region the surge is in. This is discussed by means of determining the compressor characteristic from the measured pressure and mass flow data.

3.1 Governing equations and parameters

The compression system is modelled by a non-linear lumped parameter model, for which the different components are shown in Figure 3.1. Details of the equations of motion are given in Appendix C. Three components can be distinguished: the compressor duct, the plenum, and
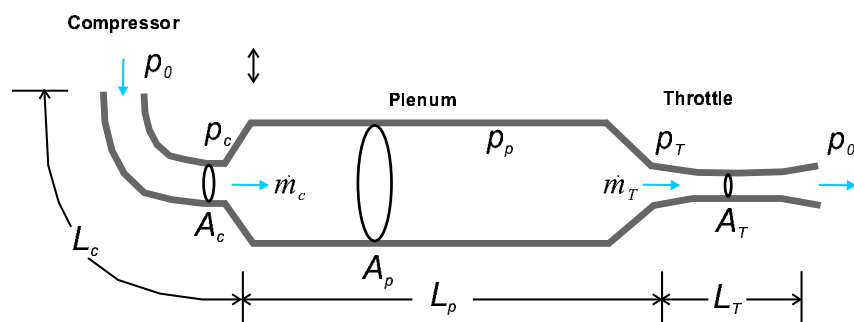
Figure 3.1: Compression system components.

the throttle valve duct. The pressure rise that is established in the compressor and the pressure drop in the throttle valve are represented by conservation of momentum for an incompressible flow in a duct. Due to the presence of the plenum, in which isentropic compression is assumed,

Table 3.1: Parameters and variables used in the model.

Symbol	Definition	Dimension
A_c	Compressor duct area	[m^2]
A_T	Throttle valve duct area	[m^2]
a	Speed of sound	[m/s]
L_c	Equivalent compressor duct length	[m]
L_T	Equivalent throttle valve duct length	[m]
$\dot{m}_c$	Compressor mass flow	[kg/s]
$\dot{m}_T$	Throttle valve mass flow	[kg/s]
N	Rotational speed	[rpm]
p_0	Ambient pressure	[Pa]
p_p	Plenum pressure	[Pa]
Δp_c	Steady-state compressor pressure difference	[Pa]
Δp_T	Steady-state throttle valve pressure difference	[Pa]
t	Time	[s]
U_t	Blade tip speed	[m/s]
V_p	Plenum Volume	[m^3]
ω_H	Helmholtz frequency	[rad/s]
c_T	Dimensionless throttle valve parameter	[-]
$\tilde{t}$	Dimensionless time	[-]
Y_T	Dimensionless throttle valve position	[-]
ϕ_c	Dimensionless compressor mass flow	[-]
ϕ_T	Dimensionless throttle valve mass flow	[-]
ψ	Dimensionless plenum pressure rise	[-]
ψ_c	Dimensionless steady-state compressor pressure rise	[-]
ψ_T	Dimensionless steady-state throttle valve pressure rise	[-]

the mass flow through the compressor can be different from the mass flow through the throttle. Therefore, a mass balance in the plenum is applied. The governing equations that describe the dynamics of the compression system are (Equation (C.3), (C.4) , and (C.6)):

$$\frac{d\dot{m}_c}{dt} = -\frac{A_c}{L_c}\left\{p_p - p_0 - \Delta p_c\right\} , \tag{3.1}$$

$$\frac{d\dot{m}_T}{dt} = -\frac{A_T}{L_T}\left\{p_0 - p_p + \Delta p_T\right\} , \tag{3.2}$$

$$\frac{dp_p}{dt} = \frac{a_p^2}{V_p}\left\{\dot{m}_c - \dot{m}_T\right\} . \tag{3.3}$$

The meaning of the parameters and variables used in the model are listed in Table 3.1. Introducing the dimensionless mass flow ϕ and the dimensionless pressure difference ψ:

$$
\begin{aligned}
\phi &= \frac{\dot{m}}{\rho A_c U_t} \, , \\
\psi &= \frac{\Delta p}{\frac{1}{2}\rho U_t^2} \, .
\end{aligned}
$$

The nondimensional representation of the dynamics of the compression system are (Equation (C.7), (C.8), and (C.9)):

$$
\frac{d\phi_c}{d\tilde{t}} = -B\left\{\psi - \psi_c\right\} \, , \tag{3.4}
$$

$$
\frac{d\phi_T}{d\tilde{t}} = -\frac{B}{G}\left\{-\psi + \psi_T\right\} \, , \tag{3.5}
$$

$$
\frac{d\psi}{d\tilde{t}} = \frac{1}{B}\left\{\phi_c - \phi_T\right\} \, , \tag{3.6}
$$

with

$$
B = \frac{U_t}{2\,\omega_H L_c} \, , \qquad G = \frac{L_T A_c}{L_c A_T} \, , \qquad \tilde{t} = t\,\omega_H \, , \qquad \omega_H = a\sqrt{\frac{A_c}{V_p L_c}} \, .
$$

To be able to solve the set of equations a relation for the steady-state compressor and throttle valve pressure rise, ψ_c and ψ_T, respectively, and the geometrical parameters have to be determined. In Section 2.3 the pressure rise over the throttle valve duct is determined as function of the throttle valve position, Y_T, and the throttle valve flow, ϕ_T:

$$
\psi_T = \left(\frac{\phi_T}{c_T Y_T}\right)^2 \, , \qquad \text{with} \qquad c_T = 0.406 \, .
$$

The steady-state compressor pressure rise, ψ_c, is a function of the compressor flow, ϕ_c, and the rotational speed, N. A discussion on the determination of the steady-state characteristic is given in Section C.2. From the measurements only part of the mass flow range needed for the calculation is known. Starting at a high mass flow, at a certain point surge starts and no steady-state data is obtained. Therefore, these parts of the compressor characteristic have to be guessed. The compressor characteristic is approximated by a cubic polynomial in ϕ_c (see for reference *Moore and Greitzer [53]*):

$$
\psi_c(\phi_c) = \psi_c(0) + H\left\{1 + \frac{3}{2}\left(\frac{\phi_c}{W} - 1\right) - \frac{1}{2}\left(\frac{\phi_c}{W} - 1\right)^3\right\} \, , \tag{3.7}
$$

in which $\psi_c(0)$ is the valley point of the characteristic located at the compressor pressure rise axis. Parameter H and W are fit parameters. An illustration of the approximated compressor characteristic is given in Figure 3.2. The difference between the maximum pressure rise, $\psi_{c_{ini}}$,
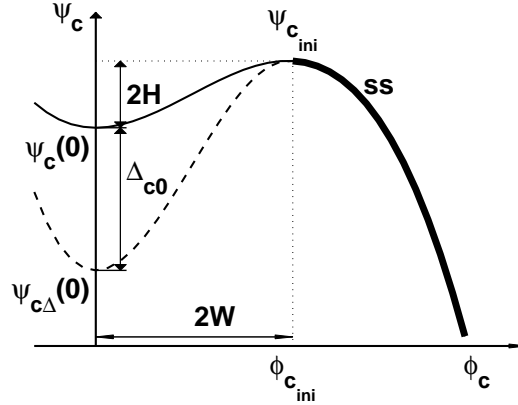
Figure 3.2: Illustration of the approximated compressor characteristic. –: cubic polynomial fitted to measurement, - -: with adjusted valley point

and the minimum pressure rise at zero mass flow, $\psi_c(0)$, is defined as $2H$. The dimensionless compressor mass flow at the top of the characteristic, $\phi_{c_{ini}}$, is defined as $2W$. To obtain a best fit of all steady-state measurements Equation (3.7) is rewritten to ([70]):

$$\psi_c(\phi_c) = c_0(N) + c_1(N)\phi_c^2 + c_2(N)\phi_c^3 \, ,$$

with

$$c_0(N) = \psi_c(0) \, , \quad c_1(N) = \frac{3H}{2W^2} \, , \text{and} \quad c_2(N) = \frac{-H}{2W^3} \, .$$

For each rotational speed line in the compressor characteristic the parameters $c_0(N)$, $c_1(N)$, and $c_2(N)$ are determined. The dependence of these parameters on rotational speed N is approximated by a quadratic polynomial in N:

$$
\begin{aligned}
c_0(N) &= & -8.0952 \cdot 10^{-10}N^2 & + 2.6068 \cdot 10^{-5}N & + 1.1289 \, , \\
c_1(N) &= & -6.4091 \cdot 10^{-8}N^2 & + 3.8522 \cdot 10^{-3}N & - 2.5466 \cdot 10^1 \, , \\
c_2(N) &= & 3.1337 \cdot 10^{-7}N^2 & - 1.6641 \cdot 10^{-2}N & + 9.5245 \cdot 10^1 \, .
\end{aligned}
$$

The stagnation pressure ratio at zero mass flow can be determined from (*Cohen et al. [11]*, *Gravdahl et al. [30]*):

$$\frac{p_2}{p_1}(0, N) = \left(1 + \frac{\pi^2(N/60)^2(d_2^2 - d_1^2)}{2c_pT_1} \right)^{\frac{\gamma}{\gamma - 1}} \, . \tag{3.8}$$

In which $d_1^2 = 1/2\,(d_{1,a}^2 + d_{1,h}^2)$ is the compressor average inlet diameter, d_2 is the impeller exit diameter, c_p is the specific heat of air at constant pressure and γ is the ratio of specific heats. The

geometric parameters of the compressor can be found in Table 2.1. The compressor pressure rise at zero mass flow then is:

$$\psi_{c\Delta}(0, N) = \frac{\left(\frac{p_2}{p_1}(0, N) - 1\right) p_1}{\frac{1}{2}\rho U_t^2} \ . \tag{3.9}$$

The calculated $\psi_{c\Delta}(0, N)$ does not agree with the approximated valley point $\psi_c(0)$, that is chosen such that the measured steady-state characteristic is approximated well. Therefore, as in *Willems [70]*, the valley point of $\psi_c(0)$ is moved without changing the approximation at the measured part of the compressor characteristic. The amount of movement, Δ_{c0}, depends on the rotational speed and is determined according to:

$$\Delta_{c0}(N) \ = \ \psi_c(0, N) - \psi_{c\Delta}(0, N) \ .$$

The dependence of this parameter on rotational speed N is approximated by a quadratic polynomial in N:

$$\Delta_{c0}(N) = -9.4433 \cdot 10^{-10} N^2 + \ 2.6631 \cdot 10^{-5} N \ + \ 3.2717 \cdot 10^{-1} \ .$$

The resulting approximated compressor characteristic is determined with the parameters W and H, and $\psi_c(0)$ which depend on ϕ_c:

$$\phi_c \geq 2W, \quad H' = H \quad \text{and} \quad \psi_c'(0) = \psi_c(0) \ ,$$

$$\phi_c < 2W, \quad H' = H + \frac{1}{2}\Delta_{c0} \quad \text{and} \quad \psi_c'(0) = \psi_c(0) - \Delta_{c0} \ .$$

In Figure 3.3(a) the approximated nondimensional compressor map is shown. As can be seen, in the region for which measured compressor data is available, the compressor characteristic is approximated well. Also, when the data is transferred to full dimensions, in Figure 3.3(b), the measured compressor data is approximated well.

The geometric parameters of the compression system are indicated in Figure 3.1. All parameters are based on physical lengths of the system and are shown in Table 3.2. For the compressor a momentum relation for an incompressible flow in a duct is solved. This requires a length over which the pressure rise takes place and an area on which the pressure acts. Therefore, the length, L_c, is chosen to be the length the flow travels from the inlet of the compressor to the inlet of the volute. The assumption is that this is the length in which the largest part of the pressure build-up takes place. (The contribution to the pressure rise from the inlet to the outlet of the volute only measures 0.5 % of the total pressure rise.) The area, A_c, is based on the inlet throughflow area, according to Equation (2.2).

For the throttle valve also a momentum relation for an incompressible flow in a duct is solved. The pressure drop is assumed to take place over the length of the throttle valve flow channel. Furthermore, the area of the throttle is taken to be a function of the throttle valve position. The maximum area is assumed to be the area of the pipe the throttle is connected to. For the plenum an isentropic compression is assumed. This requires the speed of sound, a_p, in the plenum and the volume in which compression takes place. The plenum consists of the volume of the pipe between the compressor and the throttle and the volume of the volute.

(a) nondimensional   (b) dimensional
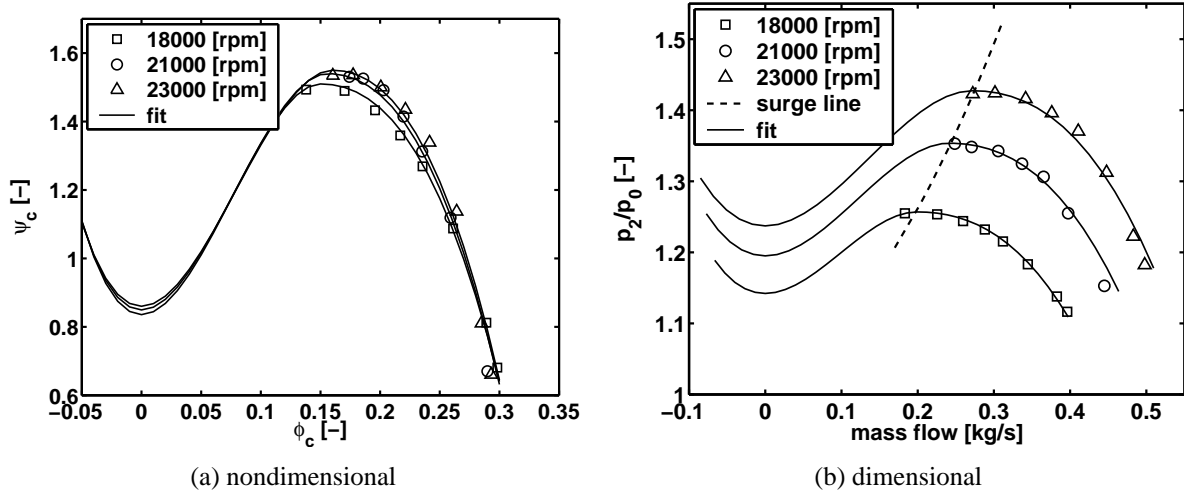
Figure 3.3: Approximated compressor map.

Table 3.2: Compression system parameters.

Parameter	Value		Parameter	Value	
Compressor			**Throttle**		
A_c	$6.53 \cdot 10^{-3}$	$[\mathrm{m}^2]$	A_T	$9.56 \cdot 10^{-3}$ Y_T	$[\mathrm{m}^2]$
L_c	0.16	$[\mathrm{m}]$	L_T	0.10	$[\mathrm{m}]$
Plenum					
V_p	$2.39 \cdot 10^{-2}$	$[\mathrm{m}^3]$			

3.2 Variation of compressor duct length and plenum volume

The lumped parameter method requires equivalent duct lengths, areas, and volumes that cannot always be determined straightforwardly from the compression system. Therefore, in literature (e.g., *[70], [30], [2]*) especially the length of the compressor duct is used to match simulations with measurements. The parameters of the compression system, based on physical lengths can be found in Table 3.2. In Figure 3.4 the simulated surge cycle and its power spectral density obtained with these parameters are shown. In this chapter, the simulations are compared with measurements explained in Section 2.6, Figure 2.16(b). Note, that the measured flow is determined from a measured velocity trace and therefore not accurately determined. The pressure trace is measured accurately. Therefore, the comparison can be made best with the pressure trace. Compared to measurement, the simulated surge reveals a higher surge frequency and a lower maximum pressure rise. Furthermore, the pressurisation and pressure drop period follows the steady-state characteristic, which is typical for a deep surge cycle.

A better match with some of the measured surge characteristics can be made when the length of inertia, L_c, and the size of the compression volume, V_p, are varied and their influence on the surge frequency and surge amplitude is evaluated. In Figure 3.5 the surge frequency, and maximum and minimum pressure rises are shown versus the compressor duct length, L_c, for
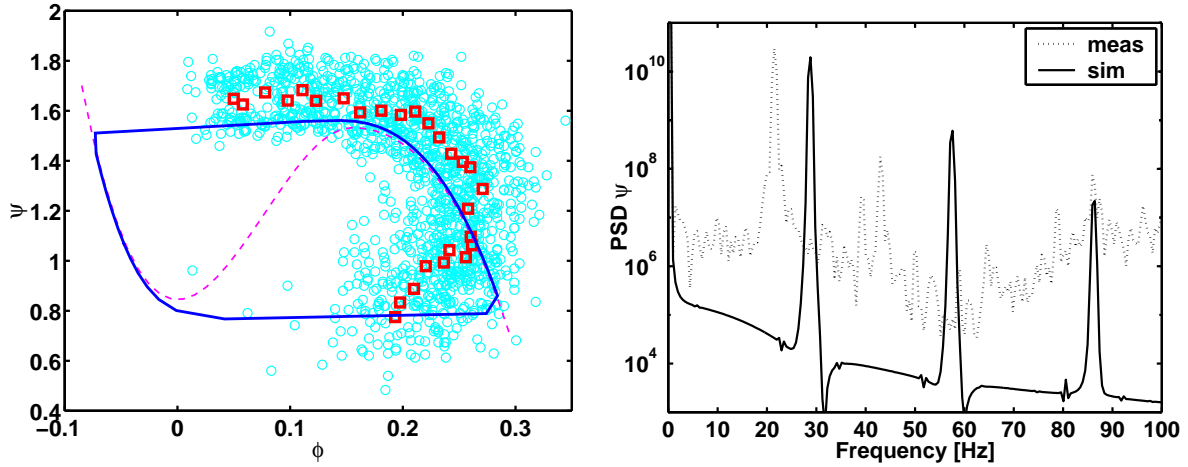
(a) surge cycle. ○: valid parts of 50 measured surge cycles, □: mean measured values, - -: steady-state characteristic, –: simulation

(b) power spectral density of the pressure rise

Figure 3.4: Simulation result. $L_c = 0.16$ [m], $V_p = 2.39 \cdot 10^{-2}$ [m^3], $N = 20100$ [rpm], $Y_T = 0.28$

different plenum sizes, V_p, for $N = 20100$ [rpm] and $Y_T = 0.28$. Furthermore, the expected (measured) value is indicated by a straight line. In Figure 3.5(a) is seen that there is not a unique combination of (L_c, V_p) which fits the indicated surge frequency. The trend is that when a larger L_c is chosen the volume V_p should become smaller.

To find out which (L_c, V_p)-combination approximates the measurements best an extra criterion, besides the surge frequency, is needed. In Figure 3.5(b) and 3.5(c) the maximum and minimum pressure rises are shown. As can be seen, the pressure rises are, for small L_c, hardly affected by a change in plenum volume. Furthermore, it is seen that the measured maximum and minimum pressure rises are not coinciding for the same combinations of (L_c, V_p). Therefore, only the maximum or minimum pressure rise can be used as extra criterion. The correctness of the minimum pressure rise is not given too much weight. On one hand, it is shown in Section 2.5, Figure 2.11 that the mean measured minimum pressures reveal a scattered result. On the other hand, in the simulations the steady-state compressor characteristic is used for which the lowest pressure rise at zero mass flow is determined by calculation instead of by measurement. Both arguments introduce a large uncertainty about the minimum pressure during surge. The maximum pressure is measured with less scatter and in the simulation a measured maximum pressure rise is used in the derivation of the steady-state characteristic. Therefore, the maximum pressure rise is used to determine the (L_c, V_p)-combination that approximates the measurements best.

The resulting length and plenum volume are $L_c = 1.4$ [m] and $V_p = 2.01 \cdot 10^{-2}$ [m^3]. These dimensions do not agree with the compression system data suggested in Table 3.2, i.e., especially the compressor length is overestimated by a factor ≈ 9. In Figures 3.6 the simulation result is shown. The measured surge frequency and higher harmonics are simulated well. Also, the maximum pressure rise is achieved. Due to the larger duct length the inertia of the system is increased and larger excursions from the steady-state characteristic are simulated. So-called classic surge cycles are obtained. Nevertheless, looking at the top of the cycle the pressure rise

(a) surge frequency

(b) maximum pressure

(c) minimum pressure
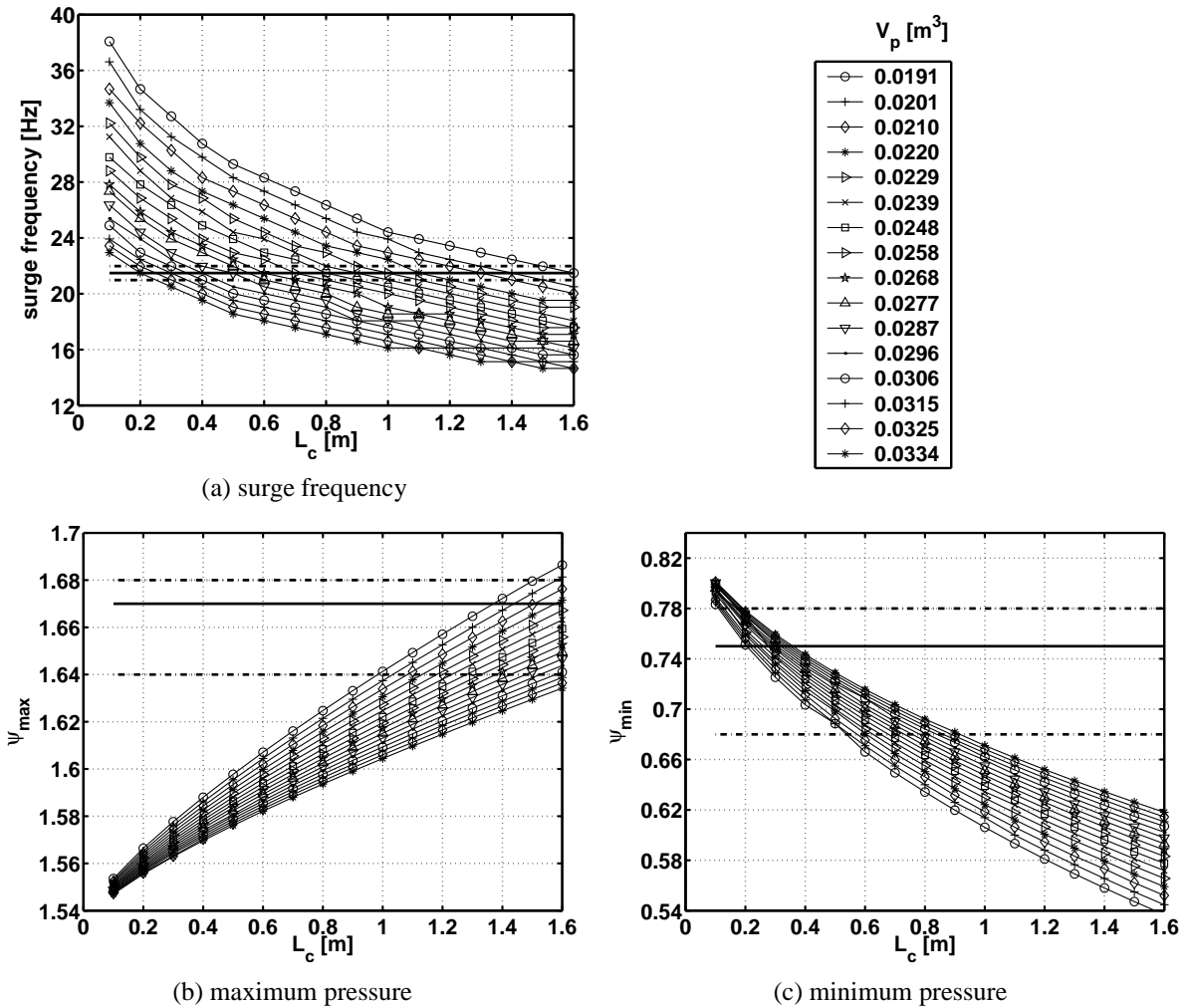
Figure 3.5: Simulation parameters versus the compressor duct length for different plenum sizes. $N = 20100$ [rpm], $Y_T = 0.28$, –: measured value with uncertainty indicated by ---

decreases too fast with decreasing mass flow to fit the measurements. The rather constant measured pressure rise is better captured if a short duct length, which result is shown in Figures 3.4, is used.

Variation of the geometrical data in the simulations yields some characteristics of the measured surge. However, a simulated surge cycle that exactly matches the measurement cannot be found. In this study, it is assumed that the geometrical data used in the model at least should be of the order of magnitude of the data determined from the compression system under investigation. Therefore, the study is continued with these values and another uncertainty in the model, i.e., the assumption of a (quasi-) steady compressor performance is looked upon.

(a) surge cycle. ○: valid parts of 50 measured surge cycles, □: mean measured values, - -: steady-state characteristic, –: simulation

(b) power spectral density of the pressure rise
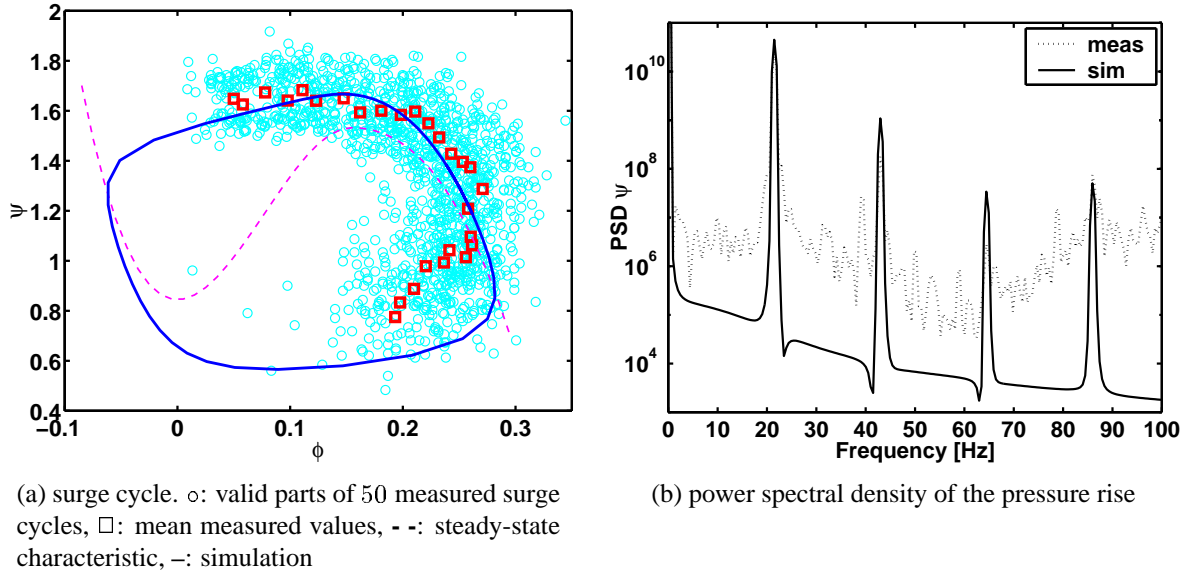
Figure 3.6: Simulation result. $L_c = 1.4$ [m], $V_p = 2.01 \cdot 10^{-2}$ [m³], $N = 20100$ [rpm], $Y_T = 0.28$

3.3 Quasi-steady compressor characteristic

In the simulations it is assumed that the compressor performance during surge follows the steady-state compressor characteristic. Due to the instability of the compression system it is difficult to determine this characteristic. Therefore, it is interesting to derive the steady-state compressor pressure rise from the surge measurements. A method to determine the (steady-state) axisymmetric compressor characteristic during surge is known from *Koff and Greitzer [44]*. In this approach one 'subtracts off' that part of the pressure rise due to flow accelerations (or decelerations) during a surge cycle.

$$\psi_{TS} = (\psi_{TS})_{data} + \frac{2\,L_c}{U}\,\left(\frac{d\phi}{dt}\right)_{data}. \tag{3.10}$$

Herein, ψ_{TS} is the inertially corrected pressure rise, i.e., the quasi-steady compressor performance, $(\psi_{TS})_{data}$ the nondimensional transient pressure rise across the compressor measured in the surge cycle, and $(d\phi/dt)_{data}$ the calculated derivative to time of the measured transient mean mass flow. The assumption is that this equation can be applied when the compressor mass flow transient time scale, $\tau_{trans} = 1/f_{surge}$, is larger than the blade passage performance response timescale, τ_{blade}. (τ_{blade} = blade chord/throughflow velocity at instability point, is assumed to be of the order of the time required to convect a vortex through the blade passage.) In the case of the centrifugal compressor: $f_{surge} \approx 20$ [Hz], blade chord ≈ 0.16 [m], and the throughflow velocity at instability point ≈ 10 [m/s]. So, $\tau_{trans} \approx 5 \cdot 10^{-2}$ [s] is larger than $\tau_{blade} \approx 1.6 \cdot 10^{-2}$ [s]. Furthermore, it is assumed that the mass flow change through the compressor is more rapid than the time for rotating stall formation, τ_{form}.

The transient compressor pressure rise depends on the term $2\,L_c/U\,(d\phi/dt)_{data}$, which depends on the compressor duct length, L_c. The larger L_c the larger the difference between the plenum

pressure, $(\psi_{TS})_{data}$, and ψ_{TS}. Furthermore, the influence of this term is mainly seen where $d\phi/dt$ is large, i.e., in the region in which a maximum pressure rise is obtained and the mass flow changes quickly from a positive flow to a negative flow. In Equation (3.10) the measured plenum pressure rise and the measured compressor mass flow is required. As explained above, the mass flow measurement is determined from a one-point velocity measurement at the inlet. Therefore, it is difficult to determine a reliable $d\phi/dt$. In Figure 3.7 simulations applied to the valid surge points with the reversed flow model for $L_c = 0.16$ [m] and $L_c = 1.4$ [m] are shown.

(a) $L_c = 0.2$ [m]   (b) $L_c = 1.4$ [m]
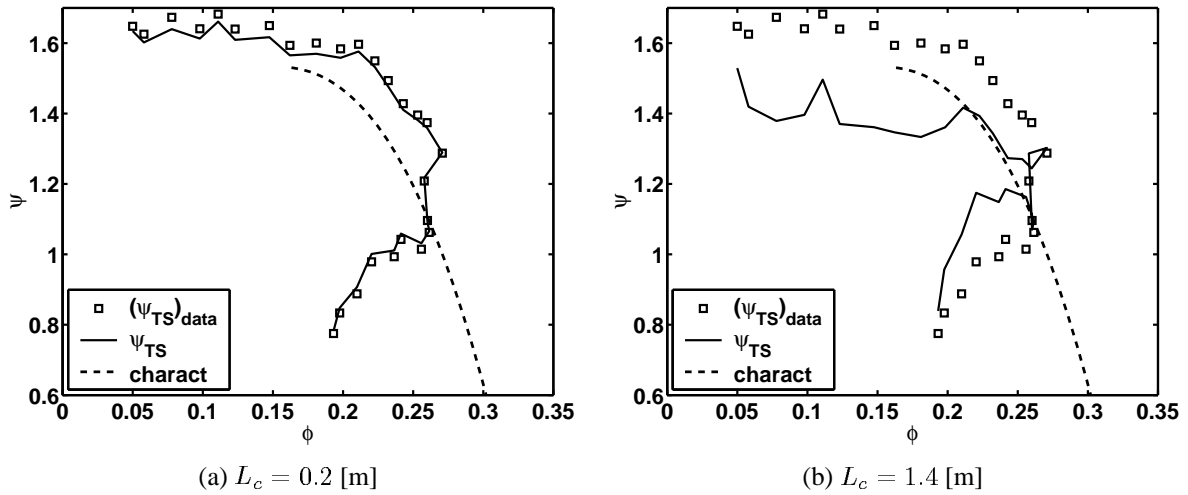
Figure 3.7: Inertially corrected surge data for two duct lengths. $N = 20100$ [rpm], $Y_T = 0.28$

It is seen that for a short compressor duct length the simulated compressor pressure rise hardly differs from the measured plenum pressure rise. With respect to the steady-state compressor characteristic, that is fitted to steady-state measurements, the small duct simulated compressor pressure rise only crosses the characteristic once instead of following it. The transient compressor pressure rise is larger than the steady-state compressor pressure rise, which is possible if during the transients the losses in the compressor are less than those at steady-state.

For the larger duct length the difference between the simulated compressor pressure rise and the plenum pressure rise is larger due to the contribution of the increased length in Equation (3.10). As can be seen, the simulated compressor pressure rise follows the steady-state compressor characteristic partly in the pressurization period. Nevertheless, the largest part of the simulated compressor pressure rise shows a deviation from the steady-state compressor characteristic.

Another method to obtain the compressor pressure rise during surge is to use only the measured plenum pressure rise. This method is also described in *Meuleman et al. [51]*. The rate of change of the compressor and throttle valve mass flows, Equations (3.4) and (3.5), are still applicable. The unsteady compressor pressure rise is found by substitution of Equation (3.4) and Equation (3.5) in the derivative of Equation (3.6):

$$\psi_c = \frac{d^2\psi}{d\tilde{t}^2} + \left\{ 1 + \frac{1}{G} \right\} \psi - \frac{1}{G} \psi_T \;.$$

However, note that the second derivative of the measured plenum compressor pressure rise, $d^2\psi/d\tilde{t}^2$, is difficult to determine accurately from the measurements.

In Figure 3.4 the higher order harmonics of the measured surge cycle are more than one order of magnitude smaller than the first harmonic. Therefore, the measured plenum pressure is approximated by a sinusoidal function based on the first harmonic of the surge cycle. This results in a periodic sinusoidal behaviour of the simulated compressor pressure rise (ψ_c), which only differs slightly from the measured plenum pressure (ψ_p), see Figure 3.8. Instead of a quasi-steady compressor performance this method also yields an unsteady compressor performance.

(a) simulated surge cylces. ∘: valid parts of 50 measured surge cycles, □: mean measured values, - -: steady-state characteristic

(b) time traces. symbols: valid / invalid parts of measurement, –: approximated plenum pressure rise and simulated mass flow

Figure 3.8: Simulation of compressor pressure rise during surge. $N = 20100$ [rpm], $Y_T = 0.28$, $L_c = 0.16$ [m], $V_p = 2.39 \cdot 10^{-2}$ [m^3], ψ_p: approximated, ψ_c, ϕ: simulated

To extract the steady-state compressor characteristic from the transient surge measurements using the lumped parameter model appears to be unsuccessful. Therefore, the assumption that the compressor performance can be modelled to react quasi-steady to flow changes seems not applicable. At least, the transient behaviour of the compressor performance should be taken into account.

3.4 Departure from steady-state compressor performance

In literature, a relaxation equation is added to the set of equations that describe the compressor response to departure from steady-state. For details see Appendix C.3. The approximation for the transient compressor response is written as:

$$\tau \frac{d\Delta p_c}{dt} = \Delta p_{c_{ss}} - \Delta p_c , \qquad (3.11)$$

with $\Delta p_{c_{ss}}$ denoting the steady-state measured compressor curve. The physical idea behind this is that during the surge cycle the compressor is not at all time working according to the quasi-steady compressor characteristic. Originally, the equation is used to describe the influence of the development of a stall cell on the compressor performance, e.g., *[31]* and *[2]*. Then, τ is the time constant associated with the circumferential development of a stall cell. *Hansen et al. [34]* used the relaxation equation to match simulation results with experimental data. In that case, the dynamic compressor performance is lumped on Equation (3.11) and it has no physical meaning. Furthermore, the equation is applied to describe the pressure build-up delays determined by the blade passage response time (Strouhal number) in a centrifugal compressor, *[23]*. This response time suggests that a disturbance developed during a surge cycle is not necessarily convected before a new cycle starts. Since no formation of stall cells during the surge cycle are measured it is assumed that the blade passage response time, $\tau_{blade} \approx 1.6 \cdot 10^{-2}$ [s], should be applied to the experimental system.

The relaxation Equation (3.11) mainly has its influence on the momentum equation for the duct, Equation (3.1), since only in this equation the steady-state compressor performance is used. The response times of the Equations (3.1), (3.2), and (3.3) are, respectively:

$$\tau_c \approx 5 \cdot 10^{-4} \quad [s] , \tag{3.12}$$

$$\tau_T \approx 7 \cdot 10^{-4} \quad [s] , \tag{3.13}$$

$$\tau_p \approx 1 \cdot 10^{-2} \quad [s] . \tag{3.14}$$

Herein, the different time scales of the surge cycle are seen: At the beginning of a surge cycle a fast drop of mass flow on the order of the compressor and throttle, response times, τ_c, and τ_T, respectively, takes place. This response time is also found when the flow recovers from a negative to a positive flow. A slow drop of pressure in the plenum for the negative flow period and a slow repressurization of the plenum for the positive flow period are represented by the plenum response time, τ_p.

If, to a certain extent, the response time is expected to have an influence on the compressor duct equation it should be on the order of τ_c. So, $\tau \sim 1 \cdot 10^{-3} - 1 \cdot 10^{-4}$ [s], which is an order of magnitude smaller than the determined blade passage response time $\tau_{blade} \approx 1.6 \cdot 10^{-2}$ [s]. The simulation for two different response times are shown in Figure 3.9. For $\tau = 1 \cdot 10^{-4}$ [s] it is seen that the relaxation has an influence on the period in which a fast mass flow change takes place. Here, the time-dependent compressor pressure, ψ_c, differs from the steady-state compressor pressure, ψ_{css}. If both pressures are studied versus time ψ_c would always be behind ψ_{css}. The chosen time scale is too small to show an influence on the period in which the plenum pressure drops or repressurizes. For a larger relaxation time, $\tau = 5 \cdot 10^{-4}$ [s], the difference between ψ_c and ψ_{css} becomes larger. The large excursions of the time-dependent compressor pressure at the extreme mass flows are due to a transitional stage from a fast time scale to a slow time scale, that becomes more and more dominant as τ is increased.

Although it hardly can be seen in Figure 3.9, the effect of the relaxation equation in the model is that in the simulation the maximum pressure rise is lower than without this equation. This means that it works in the opposite direction of what is necessary to simulate the surge cycle as it is measured. Therefore, the relaxation equation does not suit the present problem.

(a) simulated surge cylces. $\tau = 1 \cdot 10^{-4}$ [s], ○: valid parts of 50 measured surge cycles, □: mean measured values, - -: ψ_{css}, steady-state characteristic

(b) simulated surge cylces: $\tau = 5 \cdot 10^{-4}$ [s], ○: valid parts of 50 measured surge cycles, □: mean measured values, - -: ψ_{css}, steady-state characteristic

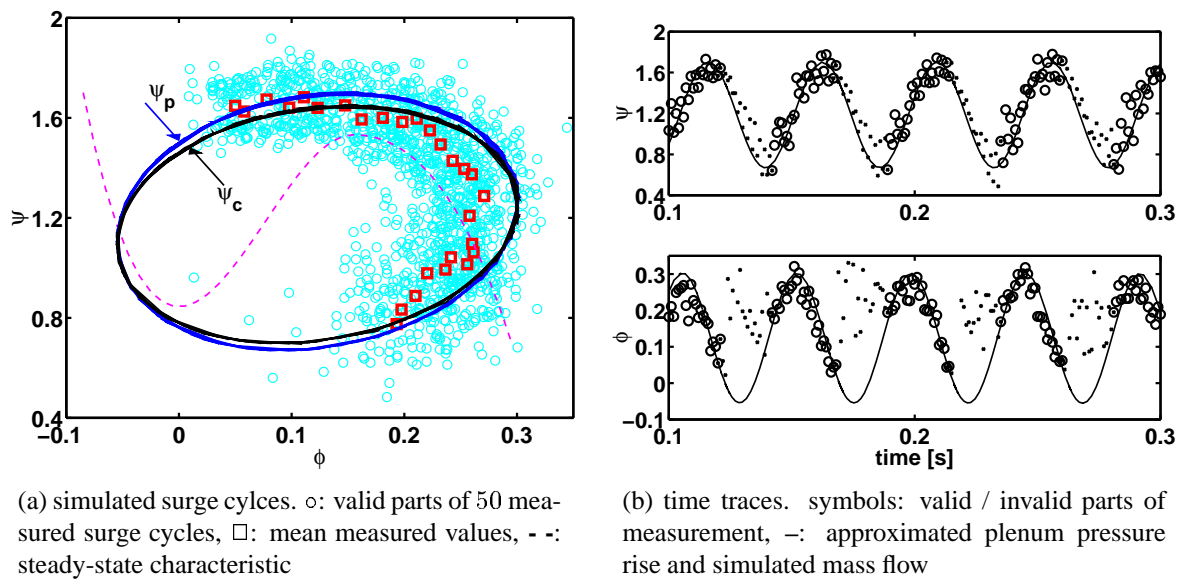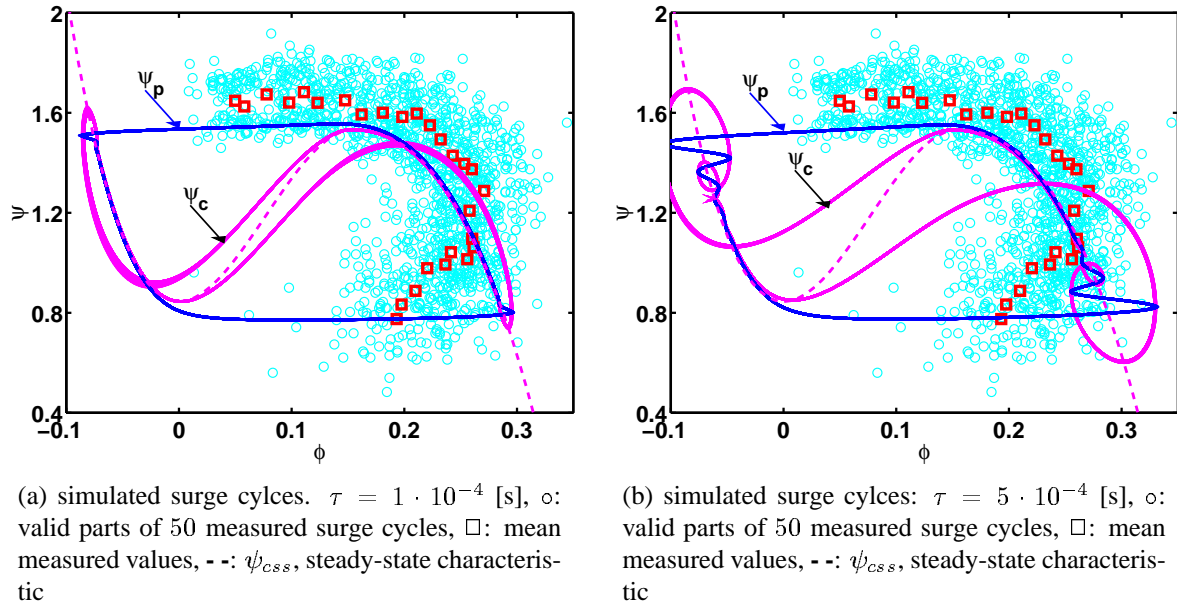Figure 3.9: Simulation of compressor pressure rise during surge. $N = 20100$ [rpm], $Y_T = 0.28$, $L_c = 0.16$ [m], $V_p = 2.39 \cdot 10^{-2}$ [m^3]

3.5 Discussion

In this chapter it is shown that the parameters in the lumped parameter method are difficult to determine from the geometrical data of the system. By varying the compressor duct length and plenum volume different surge cycles can be simulated. Nevertheless, no combination is found that exactly seems to describe the surge cycle as it is measured. Therefore, an other component of the model is focussed upon. The use of a steady-state compressor characteristic for a simulation of transient flow is questioned. The two presented methods to reveal a quasi-steady characteristic from the measurement data are not successful. On one hand, it is difficult to use the measurement data in the differential equations which are solved to obtain the quasi-steady compressor performance. On the other hand, it is credible that the compressor flow during the surge cycle is related to a time-dependent performance. Therefore, the use of a steady-state representation of the compressor performance is insufficient to simulate the system during surge.

Application of a system relaxation equation to account for the transient performance of the compressor does not provide the desired effect. Therefore, to be able to model the unsteady compressor flow based on physical grounds, the unsteady momentum equation of the duct is studied in detail in the next chapter. A correction on a quasi-steady performance assumption is derived by means of an analytical consideration of an infinitely long straight channel with a laminar flow. Hereafter, in Chapter 5, a model experiment is presented in which the correction is applied to two different water channels. In Chapter 6 the correction is put into practice on the experimental compression system.

Chapter 4

Unsteady fully-developed flow

In the conventional lumped parameter model the compressor and its ducting are replaced by an actuator disk, to account for the pressure rise due to the compressor and a constant area pipe with a certain length to account for the dynamics of the fluid in the compressor duct. The pressure rise of the compressor is taken to occur quasi-steady.

In this chapter, a representation of the unsteady compressor performance obtained through a physical model is presented. The model is made by considering the difference between an exact solution of the unsteady momentum equation and a solution obtained with a quasi-steady approach of the viscous contribution. A view on how this difference can be included in the lumped parameter model is obtained by considering an analytical solvable unsteady flow problem.

An example of an unsteady internal flow is that occurring in a channel when the fluid is driven by periodic changes in pressure, see *Schlichting [65]*. This flow is realised by a periodically moving piston. (In Appendix E the results are presented for a pipe flow.)

4.1   Exact solution of an oscillating channel flow

The channel is assumed to be infinitely long, with the $x-$axis lying in the centre, see Figure 4.1. Since the channel is assumed to be long, a fully developed incompressible flow, which motion is independent of x, is studied. From the incompressible Navier-Stokes equations a linear equation
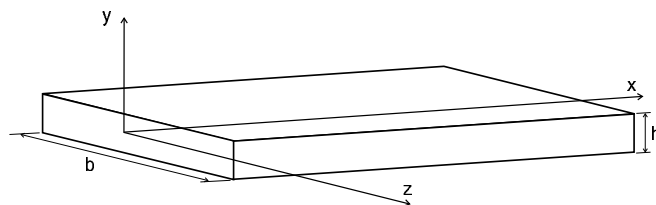
Figure 4.1: Infinitely long channel.

is obtained:

$$\frac{\partial u}{\partial t} = -\frac{1}{\rho}\frac{dp}{dx} + \nu\frac{\partial^2 u}{\partial y^2}, \tag{4.1}$$

with boundary conditions $u = 0$ at $y = \pm h/2$.

The pressure gradient is assumed to be set by a harmonically moving piston:

$$-\frac{1}{\rho}\frac{dp}{dx} = \mathcal{K}\sin(nt)\,,$$

in which $\mathcal{K}$ is a constant, and $n = 2\pi f$, with f the frequency of the oscillation. To solve the linear differential equation a complex notation of the pressure gradient is used:

$$-\frac{1}{\rho}\frac{dp}{dx} = -i\,\mathcal{K}\,e^{int}\,, \tag{4.2}$$

where only the real part has physical significance. Writing the velocity in the form $u(y,t) = U(y)\,e^{int}$, the following ordinary differential equation is found for the amplitude $U(y)$:

$$U'' - \frac{in}{\nu}\,U = i\frac{\mathcal{K}}{\nu}\,.$$

This leads to the exact unsteady velocity profile:

$$u(y,t) = -\frac{\mathcal{K}}{n}\left\{1 - \frac{\cos(\alpha_i \frac{y}{h/2})}{\cos(\alpha_i)}\right\}e^{int}\,, \tag{4.3}$$

in which

$$\alpha_i = \alpha\,\sqrt{-i}\,,$$

and the dimensionless α:

$$\alpha = \frac{h}{2}\,\sqrt{\frac{n}{\nu}}$$

is a Stokes number, that characterizes the relative importance of the time-dependent inertia term with respect to the viscous term.

The exact time-dependent mass flow is obtained by multiplying the velocity profile by the density ρ and integrating it over the height and width of the channel:

$$\begin{aligned}
\dot{m}(t) &= \int_{-b/2}^{b/2}\int_{-h/2}^{h/2}\rho\,u(y,t)\,dy\,dz\,,\\
&= \frac{i\,\rho\,\mathcal{K}\,h^2\,A}{4\,\nu\,\alpha_i^2}\,e^{int}\left\{1 - \frac{\tan(\alpha_i)}{\alpha_i}\right\}.
\end{aligned} \tag{4.4}$$

in which $A = b\,h$ is the area of the channel.

The momentum Equation (4.1) can be integrated such that it gives an equation for the derivative of the mass flow according to:

$$\int_{-b/2}^{b/2} \int_{-h/2}^{h/2} \rho \, \frac{\partial u}{\partial t} \, dy \, dz \; = \quad \int_{-b/2}^{b/2} \int_{-h/2}^{h/2} - \rho \, \frac{1}{\rho} \frac{dp}{dx} \, dy \, dz \; + $$

$$\int_{-b/2}^{b/2} \int_{-h/2}^{h/2} \rho \, \nu \, \frac{\partial^2 u}{\partial y^2} \, dy \, dz \; ,$$

$$\frac{d\dot{m}}{dt} \; = \; -A \, \frac{dp}{dx} \; + \; 2 \, b \, \rho \, \nu \, \left. \frac{\partial u}{\partial y} \right|_w . \tag{4.5}$$

Herein, is $\rho \, \nu \, \partial u/\partial y|_w = \tau_w$ the wall shear stress, with $\partial u/\partial y|_w$ the derivative of the velocity at the wall (at $y = h/2$). The exact wall shear stress can be determined with Equation (4.3):

$$\tau_w = \frac{i \, \rho \, \mathcal{K} \, h}{2} \frac{\tan(\alpha_i)}{\alpha_i} \, e^{int} . \tag{4.6}$$

Integration of Equation (4.5) over a length L in x-direction gives the exact momentum equation expressed in terms of the mass flow:

$$\frac{d\dot{m}}{dt} \; = \; - \, A \, \frac{\Delta p}{L} \; + \; 2 \, b \, \tau_w . \tag{4.7}$$

4.2   Quasi-steady approach of the viscous contribution

For very small values of n, i.e., low frequency motions, in Equation (4.3), $\cos(\phi) = 1 - \phi^2/2! + $ ... is expanded up to the quadratic term. Then a quasi-steady velocity profile is obtained:

$$u_{qs}(y,t) \; = \; - i \, \frac{\mathcal{K}}{2\nu} \left\{ \frac{h^2}{4} - y^2 \right\} \; e^{int} \qquad (n \rightarrow 0) . \tag{4.8}$$

So, for slow oscillations the velocity distribution has the same phase as the pressure gradient that forces it. Furthermore, the velocity distribution is parabolic as in the steady flow case.

The quasi-steady mass flow is obtained by determining the mass flow with:

$$\dot{m}_{qs}(t) \; = \; \int_{-b/2}^{b/2} \int_{-h/2}^{h/2} \rho \, u_{qs}(y,t) \, dy \, dz \; ,$$

$$= \; - \frac{i \, \rho \, \mathcal{K} \, h^2 \, A}{12 \, \nu} \, e^{int} . \tag{4.9}$$

The quasi-steady wall shear stress $\tau_{w_{qs}} = \rho \, \nu \, \partial u_{qs}/\partial y|_w$ can be determined from the quasi-steady velocity distribution Equation (4.8):

$$\tau_{w_{qs}} \; = \; \frac{i \, \rho \, \mathcal{K} \, h}{2} \, e^{int} ,$$

which can be made a function of the mass flow with use of Equation (4.9):

$$\tau_{w_{qs}} = -\frac{6\,\nu}{h\,A}\,\dot{m}_{qs}\ .$$

(4.10)

For this fully-developed laminar flow case the quasi-steady wall shear stress is found to depend linearly on the quasi-steady mass flow.

Following the conventional lumped parameter method with a quasi-steady viscous contribution the quasi-steady momentum equation can be formulated if the relation of the wall shear stress and the mass flow, as obtained in Equation (4.10), with an unsteady mass flow, is used:

$$
\begin{aligned}
\frac{d\dot{m}}{dt} &= -A\,\frac{\Delta p}{L} + 2\,b\,\tau_{w_{qs}}\ , \\
&= -A\,\frac{\Delta p}{L} - \frac{12\,\nu}{h^2}\,\dot{m}\ .
\end{aligned}
$$

(4.11)

In Figure 4.2 the approximated mass flow determined from the quasi-steady momentum Equation (4.11) is compared with the exact mass flow solution, Equation (4.4), for different Stokes numbers, α. Herein, the amplitude, Λ_m, represents the ratio of the amplitude of the approximated mass flow and the exact mass flow oscillation, characterised by the ratio of the standard deviations, according to:

$$\Lambda_m = \frac{\text{std}\,(\dot{m})}{\text{std}\,(\dot{m}_{ex})}\ .$$

(4.12)

This ratio becomes equal to unity at small and large Stokes numbers.

The phase, $\Delta\theta_m$, is the difference between the approximated mass flow oscillation phase, θ_m, and the exact mass flow oscillation phase, $\theta_{m,ex}$. It indicates the phase lead of the approximated mass flow relative to the exact mass flow:

$$\Delta\theta_m = \theta_m - \theta_{m,ex}\ .$$

(4.13)

The geometrical and physical values used are shown in Table 4.1 and are based on the experiments presented in Chapter 5. As can be seen in Figure 4.2, the quasi-steady approach overestimates the mass flow amplitude for $0.5 < \alpha < 80$. Furthermore, compared to the exact mass flow the quasi-steady approximated mass flow leads for $1 \cdot 10^{-1} < \alpha < 3$ in phase, while for $3 < \alpha < 2 \cdot 10^2$ it is lagging.

4.3 Determination of the correction term

4.3.1 error made with a quasi-steady approach

The error χ made with the assumption of a quasi-steady viscous term equals the difference between Equation (4.7) and Equation (4.11). This error is determined below. The quasi-steady
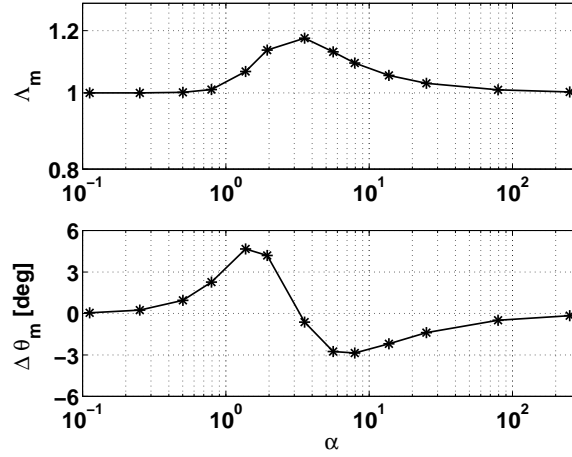
Figure 4.2: Quasi-steady approach compared to the exact solution.

Table 4.1: Channel dimensions and physical values.

h	[m]	0.02
b	[m]	0.20
L	[m]	0.50
$\mathcal{K}$	[m/s^2]	1.0
ν	[m^2/s]	$1.0 \cdot 10^{-6}$
ρ	[kg/m^3]	$1.0 \cdot 10^3$

equation then will be improved by an approximation of this χ according to:

$$\frac{d\dot{m}}{dt} = -A\frac{\Delta p}{L} + 2b\left\{\tau_{w_{qs}} + \chi\right\} . \tag{4.14}$$

In which χ is the error between the exact wall shear stress, Equation (4.6), and the quasi-steady wall shear stress, as meant in Equation (4.11) with the exact mass flow, Equation (4.4):

$$\begin{aligned}
\chi &= \tau_w - \tau_{w_{qs}} , \\
&= \frac{i\,\rho\,\mathcal{K}\,h}{2}\left\{\frac{\tan(\alpha_i)}{\alpha_i} + \frac{3}{\alpha_i^2}\left(1 - \frac{\tan(\alpha_i)}{\alpha_i}\right)\right\} e^{int} .
\end{aligned} \tag{4.15}$$

To get a simpler expression of this error a series expansion around $\alpha_i = 0$ is used:

$$\chi = \frac{i\,\rho\,\mathcal{K}\,h}{2}\left\{-\frac{1}{15}\,\alpha_i^2 - \frac{1}{35}\,\alpha_i^4 - \frac{11}{945}\,\alpha_i^6 + O(\alpha_i^7)\right\} . \tag{4.16}$$

The momentum equation 4.14 cannot be solved conveniently by using this χ. Therefore, an other expression is suggested.

4.3.2 approximation of the error

The error, χ, represents the difference between the unsteady and the quasi- steady wall shear stress. Therefore, it is suggested to express this error by the time derivative of the quasi-steady wall shear stress. Since the quasi-steady wall shear stress is a function of the time-dependent mass flow it can be written as:

$$\frac{d\tau_{w_{qs}}}{dt} = \frac{d\tau_{w_{qs}}}{d\dot{m}} \frac{d\dot{m}}{dt} \; . \tag{4.17}$$

In this analytical case the derivative of the quasi-steady wall shear stress is constant. From Equation (4.10) it is seen that:

$$\frac{d\tau_{w_{qs}}}{d\dot{m}} = -\frac{6\,\nu}{h\,A} \; .$$

The derivative of the exact mass flow to time is determined with Equation (4.4):

$$\frac{d\dot{m}}{dt} = -i\,A\,\rho\,\mathcal{K}\,e^{int} \left\{ 1 - \frac{\tan(\alpha_i)}{\alpha_i} \right\} \; .$$

The series expansion of the derivative of the exact mass flow is:

$$\frac{d\dot{m}}{dt} = i\,A\,\rho\,\mathcal{K} \left\{ \frac{1}{3}\,\alpha_i^2 + \frac{2}{15}\,\alpha_i^4 + \frac{17}{315}\,\alpha_i^6 + O(\alpha_i^7) \right\} \; .$$

So,

$$\frac{d\tau_{w_{qs}}}{dt} = -\frac{i\,6\,\nu\,\rho\,\mathcal{K}}{h} \left\{ \frac{1}{3}\,\alpha_i^2 + \frac{2}{15}\,\alpha_i^4 + \frac{17}{315}\,\alpha_i^6 + O(\alpha_i^7) \right\} \; . \tag{4.18}$$

The first (quadratic) term in Equation (4.16) and Equation (4.18) are made equal by determining a constant, C_1, according to:

$$\frac{d\tau_{w_{qs}}}{dt}\bigg|_{1^{st}} C_1 = \chi\big|_{1^{st}} \; ,$$

$$-\frac{i\,6\,\nu\,\rho\,\mathcal{K}}{h} \frac{1}{3}\,\alpha_i^2 \, C_1 = -\frac{i\,\rho\,\mathcal{K}\,h}{2} \frac{1}{15}\,\alpha_i^2 \; ,$$

$$\rightarrow$$

$$C_1 = \frac{1}{60} \frac{h^2}{\nu} \; .$$

The second term (with α_i^4) is with this C_1 unequal to the term needed for the correction:

$$-\frac{i\,\rho\,\mathcal{K}\,h}{2} \frac{1}{35}\,\alpha_i^4 \neq -\frac{i\,6\,\nu\,\rho\,\mathcal{K}}{h} \frac{2}{15}\,\alpha_i^4 \, C_1 = -i\,\rho\,\mathcal{K}\,h \frac{1}{75}\,\alpha_i^4 \; .$$

This second term can be corrected by the second derivative of the wall shear stress to time:

$$\frac{d^2\tau_{w_{qs}}}{dt^2} = \frac{d^2\tau_{w_{qs}}}{d\dot{m}^2} \left(\frac{d\dot{m}}{dt} \right)^2 + \frac{d\tau_{w_{qs}}}{d\dot{m}} \frac{d^2\dot{m}}{dt^2} \; .$$

Since in this analytical case, the wall shear stress is linear with the mass flow the first term on the right hand side is zero. The series expansion of the second derivative of the mass flow to time is:

$$\frac{d^2 \dot{m}}{dt^2} = \frac{i\,A\,\rho\,\nu\,\mathcal{K}}{h^2} \left\{ -\frac{4}{3}\,\alpha_i^4 \;-\; \frac{8}{15}\,\alpha_i^6 \;-\; O(\alpha_i^7) \right\} \; .$$

So,

$$\frac{d^2 \tau_{w_{qs}}}{dt^2} = -\frac{i\,6\,\nu^2\,\rho\,\mathcal{K}}{h^3} \left\{ -\frac{4}{3}\,\alpha_i^4 \;-\; \frac{8}{15}\,\alpha_i^6 \;-\; O(\alpha_i^7) \right\} \; .$$

A second constant, C_2, can now be determined:

$$C_2 \left.\frac{d^2 \tau_{w_{qs}}}{dt^2}\right|_{1st} \;+\; C_1 \left.\frac{d\tau_{w_{qs}}}{dt}\right|_{2th} \;=\; -\frac{i\,\rho\,\mathcal{K}\,h}{2}\,\frac{1}{35}\,\alpha_i^4 \;,$$

$$\rightarrow$$

$$C_2 \;=\; -\frac{1}{8400}\,\frac{h^4}{\nu^2} \; .$$

This can be continued to fit the complete expansion in Equation (4.16). The error χ now can be written as:

$$\chi \;=\; \frac{1}{60}\,\frac{h^2}{\nu}\,\frac{d\tau_{w_{qs}}}{d\dot{m}}\,\frac{d\dot{m}}{dt} \;-\; \frac{1}{8400}\,\frac{h^4}{\nu^2}\,\frac{d\tau_{w_{qs}}}{d\dot{m}}\,\frac{d^2\dot{m}}{dt^2} \;+\; \dots \; . \tag{4.19}$$

In the remainder of this thesis the error is approximated by taking into account only the first derivative of the mass flow and will be called the correction term. This means that this correction term is expected to be valid for α smaller than for which the higher order term

$$-h^2/(8400\,\nu)\,d^2\dot{m}/dt^2 < 1/60\;d\dot{m}/dt \; .$$

This is the case for $\alpha < 6$.

In Figure 4.3 the mass flows determined from the corrected Equation (4.14) (new) and the quasi-steady Equation (4.11) (old) are shown both compared to the exact mass flow solution of Equation (4.3.2) for different Stokes numbers. As can be seen, the new approximation gives better results than the old approximation for $0.5 < \alpha < 2$.

4.3.3 Stokes numbers for which the correction is applicable

The exact error, Equation (4.15), and the correction term:

$$\chi_{app} \;=\; \mathcal{C}\,\frac{h^2}{\nu}\,\frac{d\tau_{w_{qs}}}{d\dot{m}}\,\frac{d\dot{m}}{dt} \qquad \left(\mathcal{C} \;=\; \frac{1}{60}\right), \tag{4.20}$$

are dependent on the Stokes number. In Figure 4.4(a) the response on the imposed pressure gradient of the exact error and the correction term is shown. Herein, the amplitude, Λ_χ, represents the ratio of the amplitude of the approximated or exact error, χ, and the pressure gradient, dp/dx, according to:
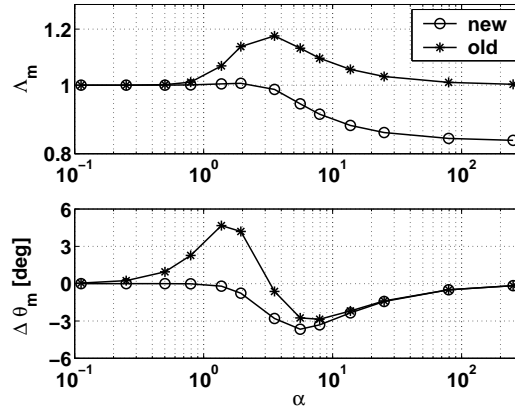
$$\Lambda_\chi \;=\; \frac{\chi}{dp/dx} \; .$$

Figure 4.3: Effect of the correction. $\mathcal{C} = \dfrac{1}{60}$

The phase, $\Delta\theta_\chi$, is the difference in phase between the approximated or exact error and the pressure gradient:

$$\Delta\theta_\chi = \theta_\chi - \theta_{dp/dx} .$$

It is seen in Figure 4.4(a), that the presented correction applies for $\alpha < 2$. In the remainder of
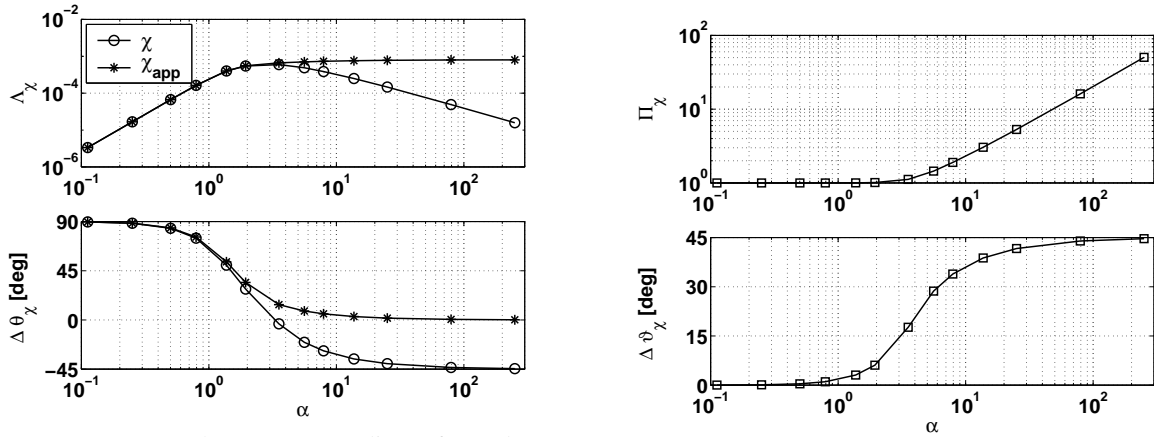
(a) response on the pressure gradient of χ and χ_{app}

(b) ratio of and phase between χ and χ_{app}

Figure 4.4: Error χ and correction χ_{app} as function of α.

this thesis the restricted value of $\alpha = 2$ will be denoted by α_{co}.

In Figure 4.4(b) the difference between the two responses are shown. Herein, the amplitude, Π_χ, represents the ratio of the amplitude of the correction term, χ_{app}, and the exact error, χ_{ex}, according to:

$$\Pi_\chi = \frac{\chi_{app}}{\chi_{ex}} .$$

The phase, $\Delta\vartheta_\chi$, represents the difference between $\Delta\theta_{\chi,app}$ and $\Delta\theta_{\chi,ex}$ that is equal to:

$$\Delta\vartheta_\chi = \theta_{\chi,app} - \theta_{\chi,ex} .$$

For $\alpha > 2$ the correction should become smaller and eventually for large α should become zero.

4.3.4   relaxation of the correction term for larger Stokes numbers

To achieve that the correction becomes smaller and eventually for large α becomes zero a relaxation equation of the correction term is suggested according to:

$$
\begin{aligned}
\frac{d\dot{m}}{dt} &= -\frac{A}{L}\,\Delta p \;+ 2\,b\,\left\{\tau_{w_{qs}} + \chi\right\}\,, \\
\tau\,\frac{d\chi}{dt} &= \mathcal{C}\,\frac{h^2}{\nu}\,\frac{d\tau_{w_{qs}}}{d\dot{m}}\,\frac{d\dot{m}}{dt} \;- \chi\,.
\end{aligned}
\tag{4.21}
$$

The time scale τ is determined from α, Equation (4.1):

$$
\tau = \frac{h^2\pi}{2\,\nu\,\alpha^2}\,.
$$

In Figure 4.5 the mass flow determined from the corrected and relaxated Equation (4.21) (new) and the quasi-steady Equation (4.11) (old) is shown versus the exact mass flow solution. (For definition of Λ_m and $\Delta\theta_m$ see Equations (4.12 and 4.13).) Time scales belonging to two extremes in Figure 4.4(b), $\alpha = 2$ and $\alpha = 200$, are applied and shown in Figures 4.5(a) and 4.5(c). For the large time scale the old solution without correction is obtained, for the small time scale the correction has a positive influence on the solution compared with Figure 4.3. The amplitude can become closer to one over the total α-range if the time scale is chosen in between the two extremes. This is shown in Figure 4.5(b). For $\alpha = 20$ a good result is obtained for the amplitude and only a small difference from zero (maximum of 2 degree) in the phase. In the remainder of this thesis the value $\alpha = 20$, determining the relaxation time, will be denoted by α_r.

4.4   Discussion

In the preceding section a correction on a quasi-steady viscous approach is proposed to include the unsteady character of the laminar flow in an infinitely long rectangular channel. In Appendix E the same theory is applied to the laminar flow in an infinitely long pipe. The characteristic data obtained from these analytical cases are summarized in Table 4.2. It is found that the correction constant $\mathcal{C}$ depends on the geometry in which the flow is studied and is larger for the pipe flow. Furthermore, the amplitude and phase deviation between the exact solution and quasi-steady approximated solution are larger for the pipe flow. An important parameter in this study is found to be the Stokes number, α. There can be indicated a certain α-range, $0.5 < \alpha < 80$, in which a correction on a quasi-steady approach is desirable. In the case $\alpha \leq \alpha_{co}$ the correction with $\mathcal{C}$ can be applied without using the relaxation equation. In the case $\alpha > \alpha_{co}$ the relaxation equation should be used and the relaxation time is determined from α_r.

In the correction term the first derivative of the quasi-steady wall shear stress with respect to time is used, which can be determined easily for this analytical case but is difficult to determine

(a) $\tau = 157$ [s] corresponding to $\alpha = 2$

(b) $\tau = 1.6$ [s] corresponding to $\alpha = 20$

(c) $\tau = 157 \cdot 10^{-4}$ [s] corresponding to $\alpha = 200$
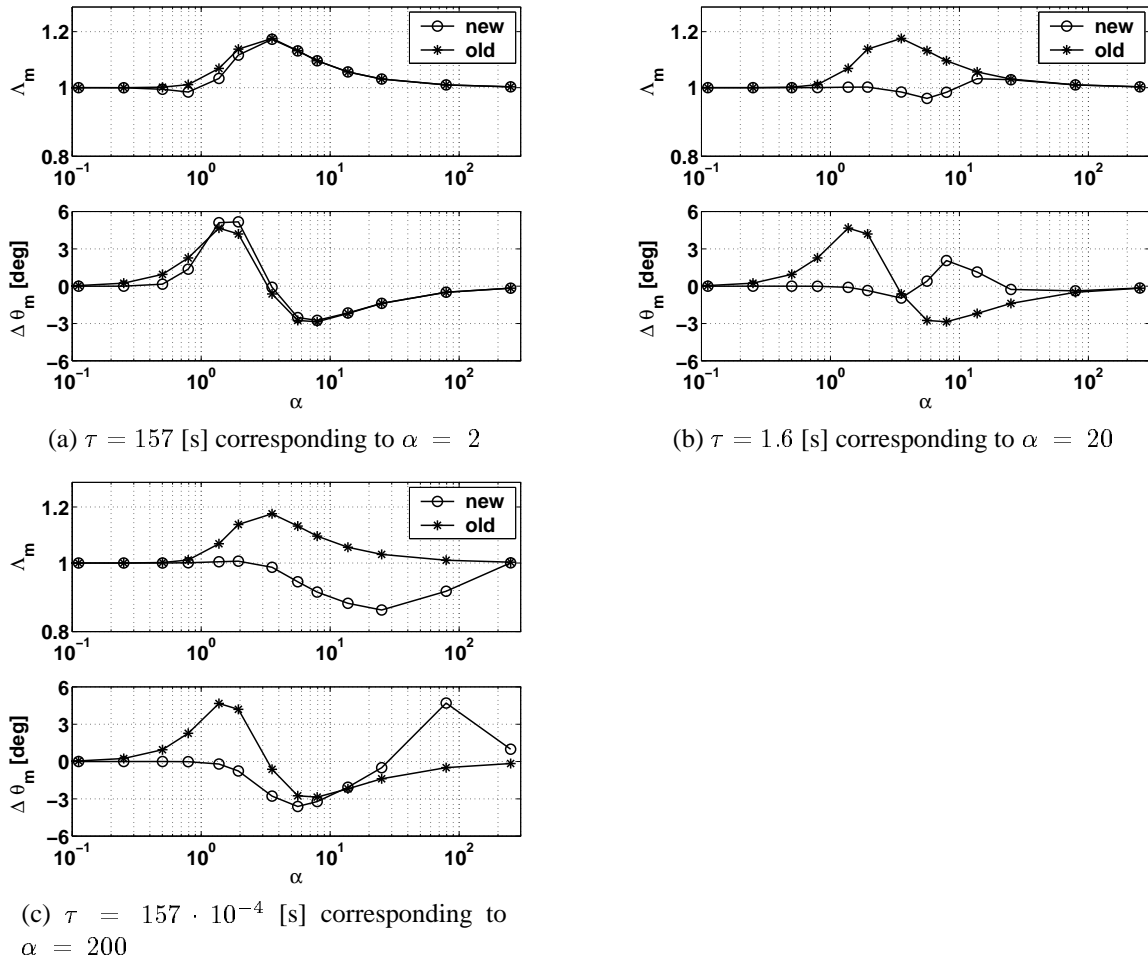
Figure 4.5: Effect of the correction with relaxation.

Table 4.2: Summary of analytically obtained data.

	Channel	Pipe	Remarks
$\mathcal{C}$	$1/60$	$1/24$	
α	$0.5 - 80$	$0.5 - 80$	correction range
α_{co}	2	2	maximum α without relaxation
α_r	20	20	α relaxation determining τ

for any other flow. Therefore, it is common to use the relation between the quasi-steady wall shear stress and the quasi-steady pressure rise, which is:

$$\tau_{w_{qs}} = \frac{A}{2\,b\,L}\Delta p_{qs} \,. \tag{4.22}$$

Using this in Equation (4.7) the momentum equation used for the compressor duct in Chapter 3 is found:

$$\frac{d\dot{m}}{dt} = -\frac{A}{L}\left\{\Delta p - \Delta p_{qs}\right\} \,.$$

The dynamics of the system under investigation can be divided in four ranges of α. For $\alpha < 0.5$ the parabolic velocity profile is obtained and the flow can be treated quasi-steady. In other words, here Equation (4.21) can be applied with a quasi-steady approach of the channel flow and without the correction term χ.

For $\alpha > 80$ the oscillating boundary-layer thickness is thin, so that most of the flow can be treated as inviscid. For Equation (4.21) this means that it is dominated by:

$$\frac{d\dot{m}}{dt} = -\frac{A}{L}\{\Delta p\}$$

and the viscous contribution by means of the quasi-steady representation of the channel flow, $A/L\ \Delta p_{qs}$, and the correction term, χ, are minor. The relation between the pressure oscillation and the mass flow is mainly based on the inertia of the inviscid fluid.

For intermediate $0.5 < \alpha \leq 80$ the viscous, convective, unsteady, and pressure terms are of the same order of magnitude. In this case the correction term should be used in the model. For $0.5 < \alpha < \alpha_{co}$, the momentum equation with the correction term expressed in terms of the wall shear stress is found by combining Equation (4.14) and Equation (4.20):

$$\frac{d\dot{m}}{dt} = -A\frac{\Delta p}{L} + 2b\left\{\tau_{w_{qs}} + \mathcal{C}\frac{h^2}{\nu}\frac{d\tau_{w_{qs}}}{dt}\right\}.$$

Next, the wall shear stress is translated to a quasi-steady pressure rise with Equation (4.22):

$$\frac{d\dot{m}}{dt} = -\frac{A}{L}\left\{\Delta p - \Delta p_{qs} - \mathcal{C}\frac{h^2}{\nu}\frac{d\Delta p_{qs}}{dt}\right\}. \tag{4.23}$$

This equation shows that the suggested correction on a quasi-steady approach of the pressure rise in an unsteady flow is the first term of a series expansion of this quasi-steady pressure rise with a time constant equal to:

$$\mathcal{C}\frac{h^2}{\nu}.$$

This constant depends on the geometry and the viscosity of the flow that can be determined for any flow.

For $\alpha_{co} < \alpha < 80$ the momentum equation with correction and relaxation, Equation (4.21), translated to a quasi-steady pressure rise should be applied:

$$\frac{d\dot{m}}{dt} = -\frac{A}{L}\{\Delta p - \Delta p_{qs}\} + 2b\chi,$$
$$\tau\frac{d\chi}{dt} = \mathcal{C}\frac{h^2}{\nu}\frac{A}{2bL}\frac{d\Delta p_{qs}}{d\dot{m}}\frac{d\dot{m}}{dt} - \chi. \tag{4.24}$$

with

$$\tau = \frac{h^2\pi}{2\nu\alpha_r^2}.$$

Comparing the relaxation equation with the relaxation equation as suggested in Equation (3.11), it is seen that here the derivative of the quasi-steady pressure rise is used. In the next chapter the correction will be tested for a turbulent inlet flow with and without an adverse pressure gradient. The Stokes range is chosen such that α_{co} and α_r can be evaluated.

Chapter 5

Measurement and simulation of flow in a water channel

In the previous chapter a correction on the conventional duct model is derived analytically for a laminar fully-developed channel flow. The developed improved model takes into account the unsteady character of the boundary-layer flow, which in the conventional model is taken to react quasi-steady to flow changes.

In this chapter the improved model is applied to a more complex flow, i.e. a turbulent inlet flow in two water channels. Measurements of channel flow with and without an adverse pressure gradient are discussed. A large advantage of the water channel is that it is easy accessible for measurements of velocities and pressures. Both channels are scaled such that the Strouhal number is $3 \cdot 10^{-2} < \mathcal{S} < 1$ and the Stokes number is $0.7 < \alpha < 7.5$. The Stokes number is in the interval in which the corrected model should be applied ($0.5 < \alpha < 80$). Simulations of the channel flows are performed with both the conventional model for a duct flow presented in Chapter 3 and the improved model derived in Chapter 4.

5.1   Experimental water channel set-up

A discussion on the water channel set-up and its measurement system is found in Appendix F. The experimental set-up consists of two reservoirs, see Figure 5.1. In between these reservoirs the test-section (3), which is made of 6 [mm] thick perspex, is mounted. A circulation pump pumps the necessary volume flow from the outlet to the inlet reservoir. The oscillations are applied at the outlet reservoir. With the use of a direct current motor and a variable power supply an oscillation frequency between $0 - 1$ [Hz] is produced. The rotation of the motor is converted into a linear movement with the use of an acentric positioned rod, which drives a plate.
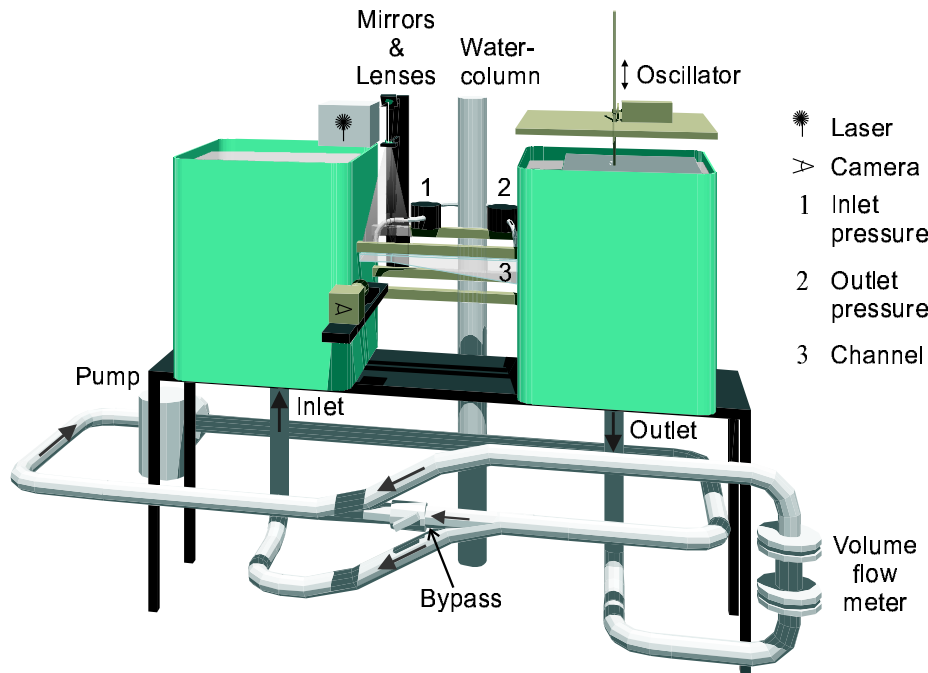
Figure 5.1: Experimental water channel set-up.

5.1.1   channels

Two different channels are tested. A straight channel and a channel with a divergence of $8 [^o]$. The dimensions of the straight and divergent channel are shown in Table 5.1 and Figure 5.2 . To obtain a 2-dimensional flow, the width of the channels is one order of magnitude larger than the height. The characteristic length of the channels is the distance between the two pressure measurement positions. The inlet and outlet of the channels are positioned inside the reservoirs.

(a) straight channel   (b) divergent channel
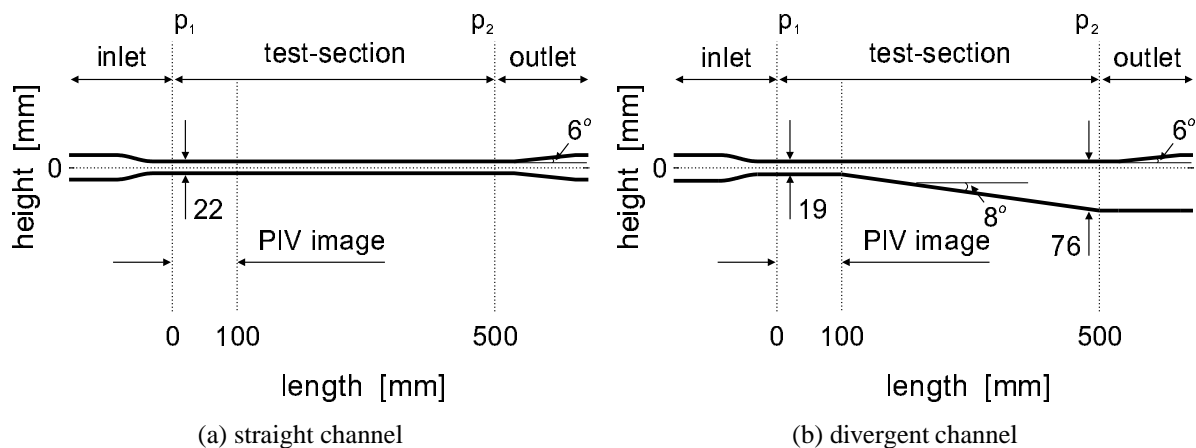
Figure 5.2: Dimensions of the diverging test-sections.

At the inlet of the channels a straightener, that consists of multiple small square channels, is used to provide a smooth inlet flow. Furthermore, the inlet is conditioned by a contraction and the outlet by a straight expansion with a divergence angle of $6 [^o]$. The outlet of the divergent test-

Table 5.1: Test-section dimensions and physical values.

			straight	divergent
d	height (PIV-area)	[m]	0.022	0.019
b	width	[m]	0.2	0.2
L	length	[m]	0.50	0.50
$\overline{u}$	mean velocity	[m/s]	0.5	$0.03 - 0.5$
ν	kinematic viscosity	[m^2/s]	$1.0 \cdot 10^{-6}$	
ρ	density	[kg/s]	$1.0 \cdot 10^{3}$	

section is at the top equal to the straight test-section, at the bottom a straight outlet is applied.

5.1.2 measurement system

An extensive discussion on the measurement system is found in Appendix F. The position of the measurement sensors is indicated in Figure 5.1 and Figure 5.2. The static pressure difference between the outlet (2) and the inlet (1) of the channel is measured with two pressure difference sensors. The steady-state volume flow is measured downstream of the outlet reservoir with a volume flow meter (VFM). The unsteady velocity profile over the height of the channel is determined with particle image velocimetry (PIV) measurements. In Figure 5.3(a) a typical velocity profile oscillation is shown. As can be seen, the shape of the velocity profile depends on the phase of the oscillation. At some instances the flow near the walls becomes negative and backflow occurs. Integration of the profile over the height and multiplication by the density gives the time-dependent mass flow, $\dot{m}$, in the channel. The resulting mass flow oscillation is shown in Figure 5.3(b). The measured pressure difference oscillation is shown as well.

(a) velocity profile   (b) pressure difference and mass flow
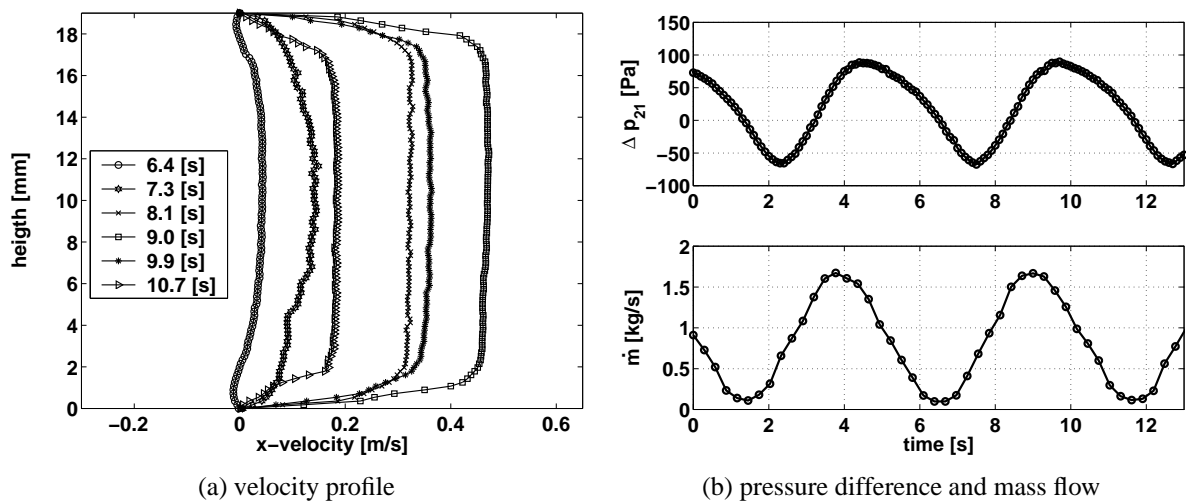
Figure 5.3: Oscillating divergent channel flow. $f = 0.20$ [Hz]

The mean velocity at the PIV-area is determined from the mean mass flow according to:

$$\overline{u} = \frac{\overline{\dot{m}}}{\rho\, A}\;.$$

In which $A = b\, d$ is the throughflow area.

5.1.3   uncertainty of the measurements

The uncertainty of the measured mass flow and pressure difference is determined from the steady-state measurement. The steady-state mean pressure difference is determined from 100 data points acquired with a 20 [Hz] sample frequency. The steady-state mean mass flow is determined from 10 PIV-determined velocity profiles acquired with a 13.75 [Hz] sample frequency.

Assuming that the measurement samples can be considered to consist of independent observations obtained at the same conditions of measurement, the uncertainty of the pressure difference measurement and mass flow measurement is determined by the normalized standard deviation (std) of the samples. In Figure 5.4 the uncertainties

$$s_p \;=\; \frac{\text{std}\,(\Delta p_{21})}{\Delta p_{21}} \;\times\; 100\;, \quad \text{and}$$

$$s_m \;=\; \frac{\text{std}\,(\dot{m})}{\overline{\dot{m}}} \;\times\; 100\;,$$

are shown versus the mean mass flow. As can be seen, the uncertainty of the mass flow is for
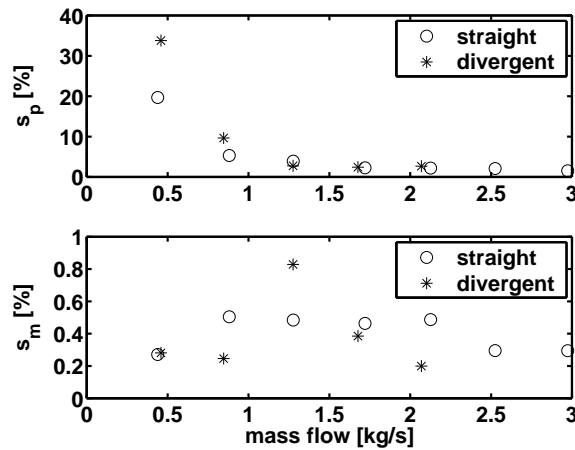
Figure 5.4: Uncertainty of the mass flow and pressure difference measurement.

the whole mass flow range smaller than 1 [%]. This is a rather low value, which could arise due to the low number of data points available to determine the uncertainty.

The uncertainty of the pressure difference is large for small mean mass flows, i.e. 20 [%] for the straight channel and 34 [%] for the divergent channel for $\overline{\dot{m}} = 0.45$ [kg/s]. For $\overline{\dot{m}} > 1.5$ [kg/s] the uncertainty of the pressure difference is smaller than 2.5 [%].

The unsteady measurements with an oscillating plate are performed mostly at a mean mass flow $\overline{\dot{m}} = 2.1$ [kg/s]. Here the uncertainties are: for the straight channel, $s_p = 2.2$ [%], $s_m = 0.5$ [%] and for the divergent channel, $s_p = 2.7$ [%], $s_m = 0.2$ [%].

5.2 Water channel measurements results

The objective of the measurements is to determine the relation between the mass flow and pressure difference in a turbulent inlet flow for oscillation frequencies that correspond to Stokes numbers in the range of $0.5 < \alpha < 80$.

5.2.1 steady-state measurements

The steady-state performance of the channels is required in the simulations. Therefore, the steady-state performance of both channels is measured, see Figure 5.5. The mass flow is measured with the volume flow meter and determined from the measured velocity distributions obtained with the PIV method. In the straight channel the VFM-mass flow is consequently smaller than the PIV-mass flow, while in the divergent channel they agree much better. The systematic difference is likely to be caused by a small error in the evaluation of the PIV images of the straight channel.

The static pressure difference between the outlet (2) and the inlet (1) of the channel is found to depend on the mass flow according to:

$$\Delta p_{ss21} = C_{ss} \, \dot{m}^2 \; .$$

Herein, is C_{ss} a constant which for the straight channel $C_{ss} = -18.3$ [(kg m)$^{-1}$] and for the divergent channel $C_{ss} = 24.0$ [(kg m)$^{-1}$]. The difference in sign is explained by the fact that a static pressure difference is measured instead of a total pressure difference, which is the sum of the static and dynamic pressure:

$$\Delta p_{21t} = \Delta p_{21} \; + \; \frac{1}{2} \, \rho \, \left(u_2^2 \, - \, u_1^2 \right) \; .$$

Since in the straight channel the velocities at both positions are approximately equal, the measured static pressure difference gives an indication of the total pressure loss of the channel. In the divergent channel $u_2 < u_1$, which introduces a static pressure rise at the outlet of the channel. Therefore, the measured static pressure difference in the divergent channel not only shows the total pressure loss of the channel but also the static pressure rise due to the adverse pressure gradient in the channel. Since $C_{ss} > 0$ in the present divergent channel, the static pressure rise is larger than the total pressure loss.

5.2.2 unsteady measurements

The relation between the pressure and mass flow is studied for oscillation frequencies $0 < f_o < 1$ [Hz]. Most experiments are performed at a mean mass flow of $\overline{\dot{m}} = 2.1$ [kg/s]. In the divergent

(a) straight channel   (b) divergent channel
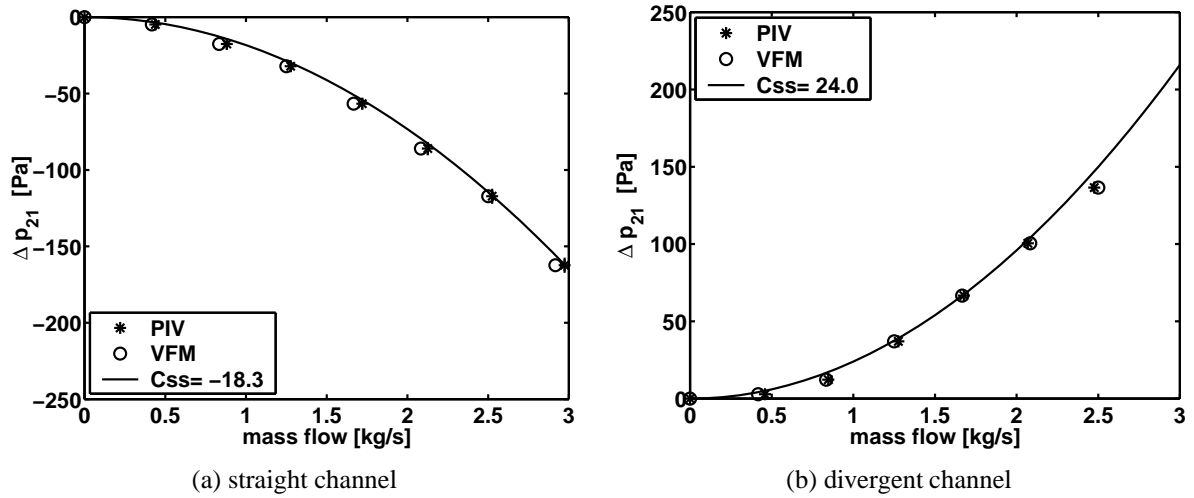
Figure 5.5: Channel characteristics.

channel a few measurements are performed at lower mean mass flows. To compare the different mass flow oscillation experiments the Strouhal number,

$$\mathcal{S} = \frac{\overline{u} f_o}{L} \, ,$$

is used. The amplitude ratios of the pressure difference and mass flow are defined as (the standard deviation is denoted by 'std'):

$$
\begin{aligned}
M &= \frac{\mathrm{std}\,(\dot{m})}{\overline{\dot{m}}} \, , \\
P &= \frac{\mathrm{std}\,(\Delta p_{21})}{\overline{\Delta p_{21}}} \, .
\end{aligned}
$$

In Figure 5.6 these measured amplitude ratios are shown for different Strouhal numbers. Note, that the number of measured periods of the mass flow with the PIV method is low. Dependent on the oscillation frequency the number of periods is between $2 - 5$. The number of measured pressure periods depends on the oscillation frequency and is between $15 - 206$ periods.

The pressure ratio is seen to depend on the Strouhal number. For low Strouhal numbers the outlet and inlet reservoirs are communicating through the channel. This introduces a smaller pressure oscillation amplitude in the channel. For $\mathcal{S} > 0.1$ the pressure amplitude ratio is nearly constant. The pressure amplitude ratio shows a slight increase at a mean mass flow of 2.1 [kg/s] and a Strouhal number > 1. On the basis of experiments with varying length of the connection tubes between the channel and the pressure sensor, it is concluded that a resonance of the connection tubes is measured. Therefore, the smallest possible tube lengths are used to avoid resonance in the oscillation frequency range of interest.

The mass flow ratio reacts for low Strouhal numbers as the pressure ratio in this Strouhal domain. For $\mathcal{S} > 0.1$ the mass flow amplitude is seen to decrease with increasing Strouhal number.

(a) straight channel. $\overline{\dot{m}} = 2.1$ [kg/s]   (b) divergent channel for various mean mass flows
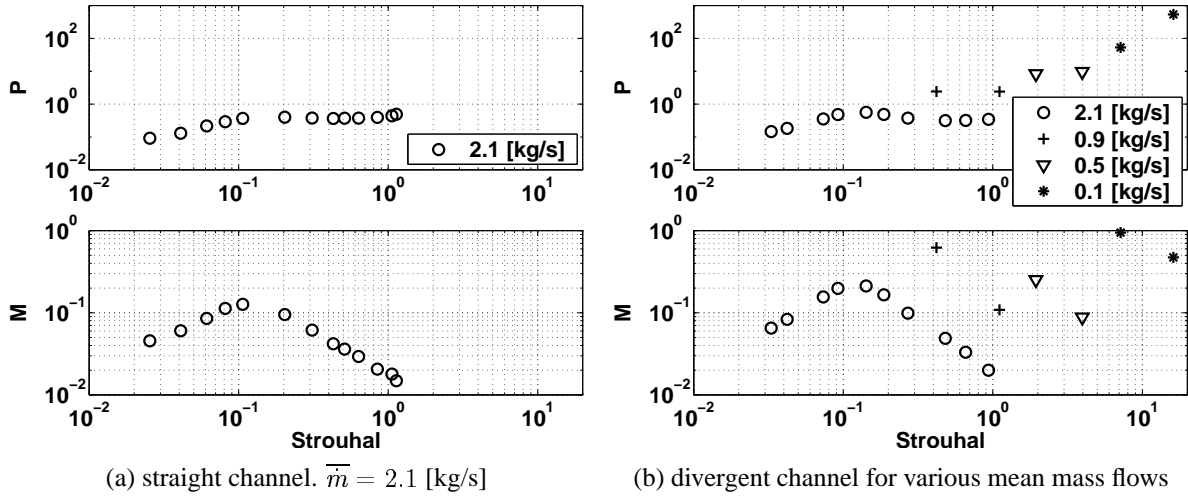
Figure 5.6: Measured amplitude ratios of pressure and mass flow for different Strouhal numbers.

To obtain an idea of the performance of the channel, the pressure trace is shown versus the mass flow trace for different Strouhal numbers in Figure 5.7 for the straight channel and in Figure 5.8 for the divergent channel. The amplitude of the oscillating plate at the outlet reservoir is the same for both channels. In the divergent channel the absolute pressure difference amplitude is larger than in the straight channel, which also results in a larger mass flow oscillation. For $\mathcal{S} \leq 0.04$ both channels show a quasi-steady behaviour along the steady-state characteristic. For $0.04 < \mathcal{S} \leq 0.11$ the mass flow and the pressure difference oscillation amplitude increases. Furthermore, a cycle around the quasi-steady characteristic is described. For larger $\mathcal{S}$, the mass flow oscillation amplitude decreases. Also, it is seen that the phase of the mass flow oscillation with respect to the pressure difference changes.

The relation between the pressure and mass flow amplitudes and phases can be shown best in a Bode plot in which the system response is shown, see Figure 5.9. The amplitude represents the ratio of the amplitude of the mass flow and the pressure oscillation, characterised by the ratio of the standard deviations, and is nondimensionalised by the derivative of the channel characteristic according to:

$$\Lambda = \frac{\text{std}\,(\dot{m})}{\text{std}\,(\Delta p_{21})} \left. \frac{d\,\Delta p_{ss21}}{d\dot{m}} \right|_{\overline{\dot{m}}} . \tag{5.1}$$

This ratio becomes equal to unity at low oscillation frequencies. In other words, at low oscillation frequencies the unsteady performance is quasi-steady and follows the steady-state characteristic. The uncertainty of the amplitude is indicated with a solid line and is only larger than the symbol size in the case of a mean mass flow ≤ 0.5 [kg/s].

The phase, $\Delta\theta$, is the difference between the mass flow oscillation phase, θ_m, and the pressure difference oscillation phase, θ_p. It indicates the phase lead of the mass flow with respect to the pressure difference:

$$\Delta\theta = \theta_m - \theta_p . \tag{5.2}$$
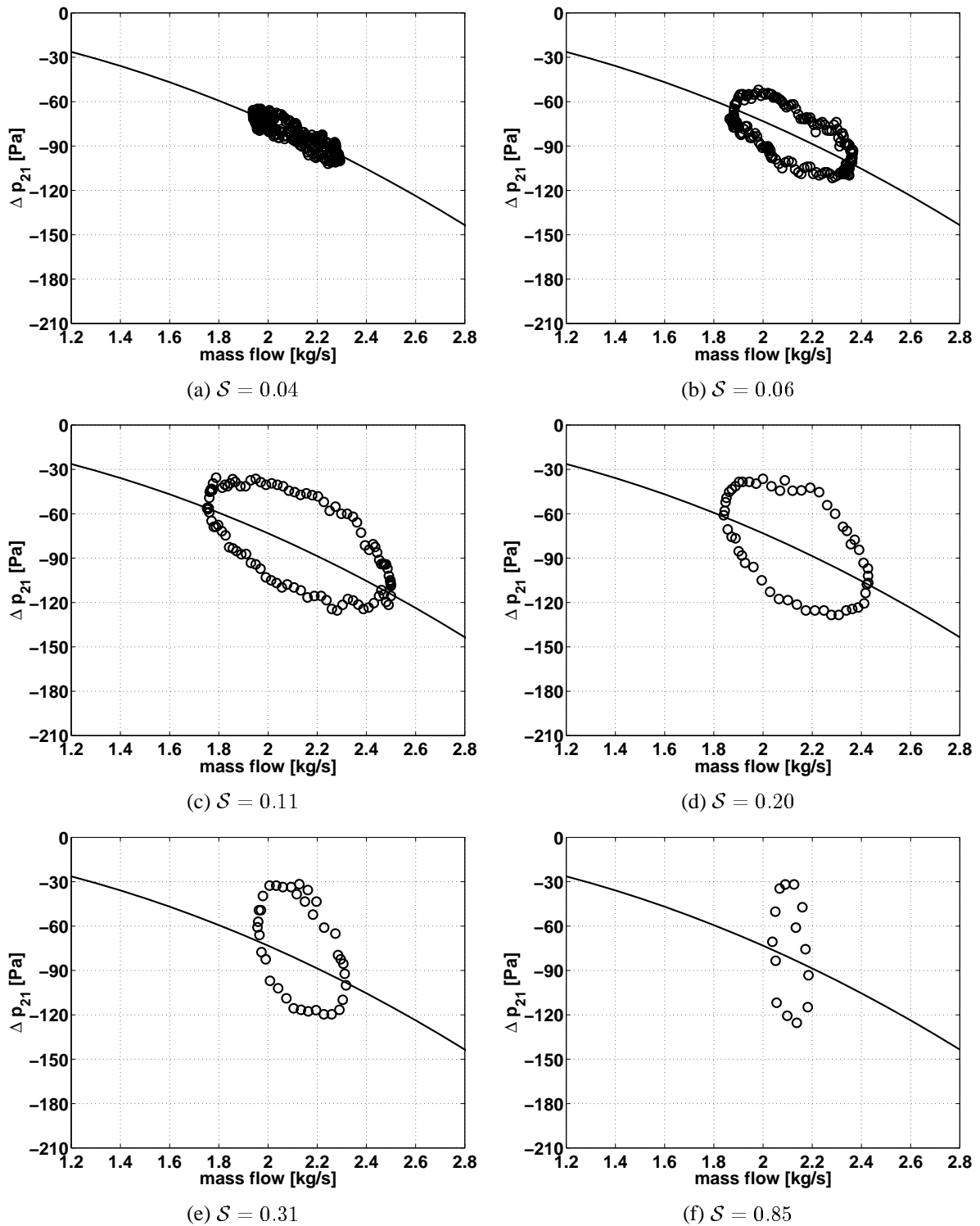
Figure 5.7: Unsteady performance of the straight channel for different Strouhal numbers. $\overline{\overline{m}} = 2.1$ [kg/s], $-$: steady-state characteristic
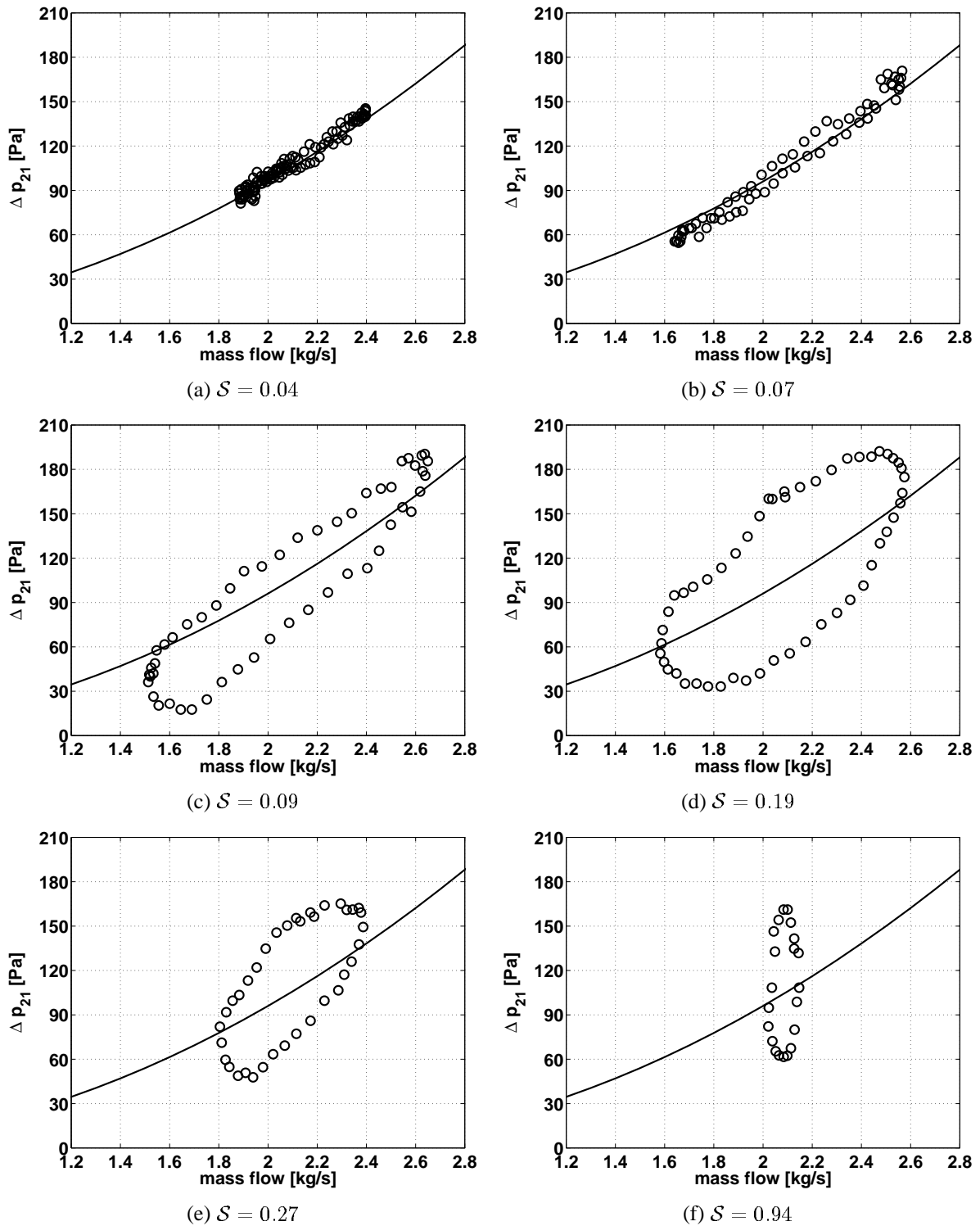
Figure 5.8: Unsteady performance of the divergent channel for different Strouhal numbers. $\overline{\dot{m}} = 2.1$ [kg/s], $-$: steady-state characteristic

The accuracy of the phase, which is discussed in Appendix F, is indicated with a solid line. Both channels show a first order response with corner Strouhal numbers that are of the same order of magnitude. The measurements performed at different mean mass flows can be scaled with the Strouhal number. The phase of the two channels is for low Strouhal numbers 180 [deg] apart. This is due to the difference in the sign of the measured static pressure gradient of the two channels.

(a) straight channel.
$\overline{\dot{m}} = 2.1$ [kg/s], $-$: uncertainty

(b) divergent channel for various mean mass flows.
$-$: uncertainty
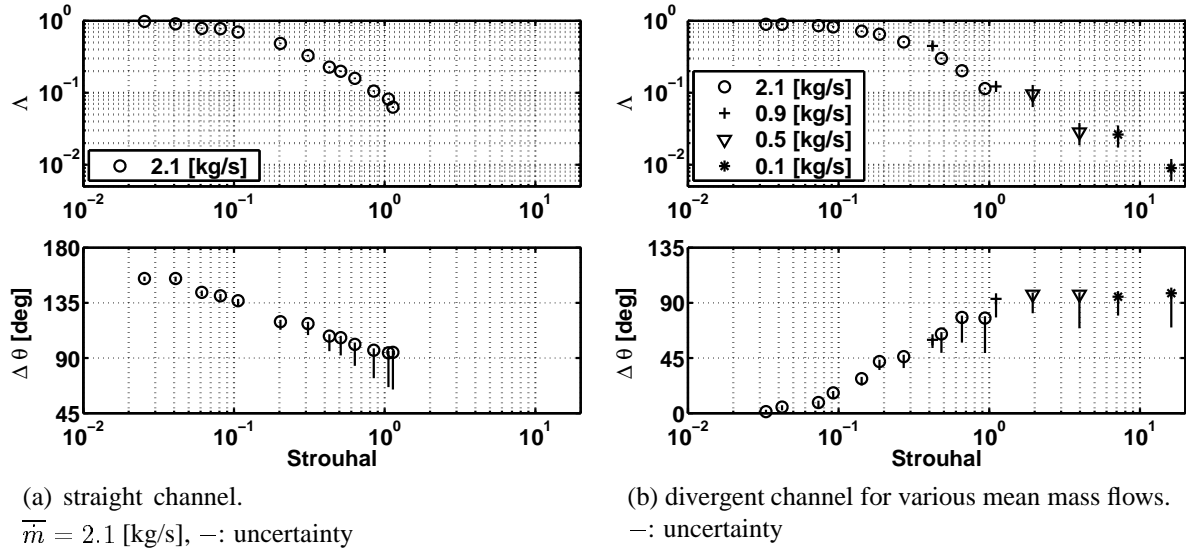
Figure 5.9: Measured system response based on Strouhal number.

5.3   Water channel flow modelling

5.3.1   conventional model

The unsteady pressure difference in the channel is simulated with a model based on a momentum balance of flow in the channel. As in the conventional model used in Chapter 3 for the compressor flow, the unsteady viscous term is replaced by the steady-state characteristic according to:

$$\frac{d\dot{m}(t)}{dt} = -\frac{A}{L} \left\{ \Delta p_{21}(t) - \Delta p_{ss21}\left(\dot{m}(t)\right) \right\} \tag{5.3}$$

The measured mass flow $\dot{m}$ is sampled such that it has values at the same time instances as the pressure difference measurement, Δp_{21}. The steady-state characteristic, Δp_{ss21}, is determined in the preceding section. Furthermore, two geometrical parameters are used: A, which is the throughflow area of the channel, and L, which is the length between the two pressure measurement positions. The throughflow area is chosen to be the smallest area of the channel. This means that also for the divergent channel the area at the PIV measurement is used. For reasons of convenience the simulations are performed with the mass flow as a known variable from the measurement. This means that the time-dependent pressure difference, Δp_{21}, is calculated.

5.3.2 improved model

The improved model, developed in Section 4.3, is applied to the water channel. For a fully-developed flow, the Stokes number can be related to half the height of the channel. The water channel flow is an inlet flow in which the boundary-layer is developing in flow direction and only occupies part of the channel height. Therefore, the Stokes number is related to the (steady) boundary-layer thickness, δ_s, according to:

$$\alpha = \delta_s \sqrt{\frac{n}{\nu}} \, .$$

Equation (4.21) then is rewritten to:

$$
\begin{aligned}
\frac{d\dot{m}}{dt} &= -\frac{A}{L} \left\{ \Delta p - \Delta p_{ss} \right\} + \chi \, , \\
\tau \frac{d\chi}{dt} &= \mathcal{C}' \frac{h^2 \, A}{\nu \, L} \frac{d\Delta p_{ss}}{d\dot{m}} \frac{d\dot{m}}{dt} - \chi \, ,
\end{aligned}
$$

with

$$
\begin{aligned}
\mathcal{C}' &= \mathcal{C} \frac{\delta_s^2}{(d/2)^2} \, , \\
\tau &= \frac{2\pi \, \delta_s^2}{\alpha_r^2 \, \nu} \, .
\end{aligned}
\tag{5.4}
$$

In Chapter 4 and Appendix E the value for α_r and $\mathcal{C}$ are determined for a fully-developed channel and a fully-developed pipe flow, see Table 4.2. The Stokes number belonging to the relaxation time τ is found to be the same for both flows, i.e., $\alpha_r = 20$, and is expected to be applicable to the present water channel flow model. The constant $\mathcal{C}$ is of the same order of magnitude for both flows, i.e., for the channel flow $\mathcal{C} = 1/60$ and for the pipe flow $\mathcal{C} = 1/24$. Since the tested water channel geometry best suits the channel flow, the constant $\mathcal{C} = 1/60$ is assumed to be valid in the water channel flow model.

5.4 Water channel simulation results

In this section the simulation and measurement results are shown for different Strouhal numbers by means of Λ, Equation (5.1), and $\Delta\theta$, Equation (5.2). The comparison between the measurements and simulations is made by means of a relative pressure amplitude that is determined by:

$$\Pi = \frac{\Lambda_{\text{simulation}}}{\Lambda_{\text{measurement}}} = \frac{\text{std}\,(\Delta p_{21})|_{\text{measurement}}}{\text{std}\,(\Delta p_{21})|_{\text{simulation}}} \, .$$

The phase, $\Delta\vartheta$, represents the difference between $\Delta\theta_{\text{simulation}}$ and $\Delta\theta_{\text{measurement}}$:

$$
\begin{aligned}
\Delta\vartheta &= \Delta\theta_{\text{simulation}} - \Delta\theta_{\text{measurement}} \\
&= \theta_{\Delta p_{21},\text{measurement}} - \theta_{\Delta p_{21},\text{simulation}} \, .
\end{aligned}
$$

5.4.1 straight channel

conventional model

Simulations of the straight channel with the conventional model (old) and the improved model (new) are shown in Figures 5.10. With respect to the conventional model, hardly any difference with the measured pressure amplitude ratio and $\Delta\theta_{\text{measurement}}$ is found. Overall, the simulated pressure difference amplitude is a little bit smaller than it is measured and the difference in phase is equal to zero within the interval it can be determined.

improved versus conventional model

Simulations with the improved model require the characteristic boundary-layer of the flow, which is used in Equation (5.4). The boundary-layer thickness in the straight channel is determined from the velocity profile shown in Figure F.4(a) and is about $\delta_s = 1.5 \cdot 10^{-3}$ [m]. So, for the straight channel, with $\alpha_r = 20$:

$$\mathcal{C}' = 3.1 \cdot 10^{-4},$$
$$\tau = 3.5 \cdot 10^{-2} \text{ [s]}.$$

The simulation results with the correction (new) for the straight channel are shown in Figure 5.10. In Figure 5.10(b) it is seen that compared to the conventional simulation results (old), a slight improvement of the pressure difference amplitude is seen for the improved model (new) results (i.e., the amplitude is near 1). The phase is not influenced by the new approach.

(a) result measurement, conventional simulation, and improved simulation

(b) comparison measurement and conventional simulation, and measurement and improved simulation
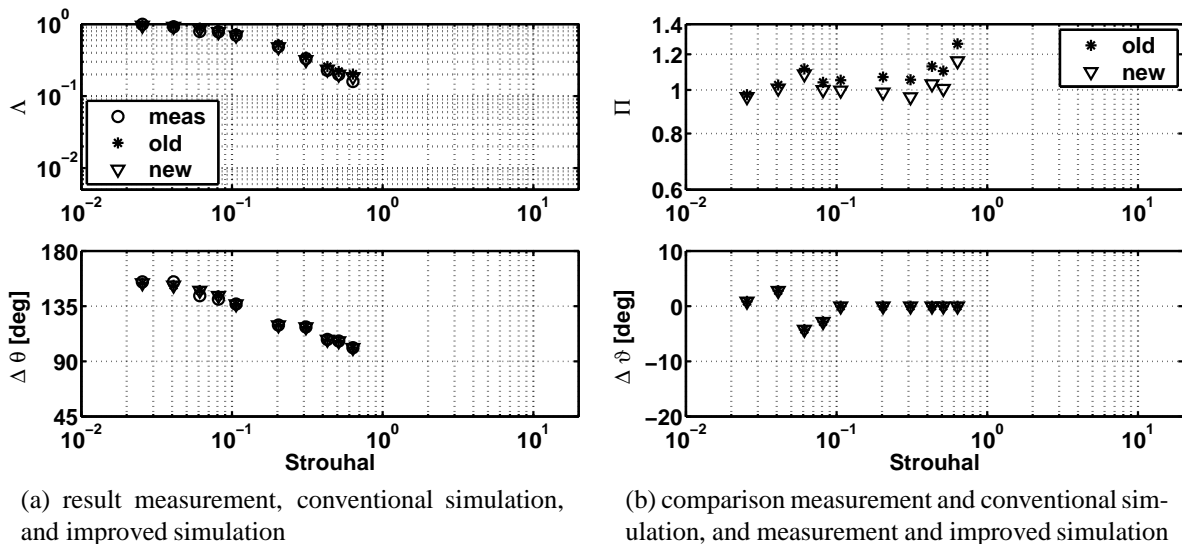
Figure 5.10: Conventional (old) simulation and improved (new) simulation of the straight channel flow. $\overline{\overline{m}} = 2.1$ [kg/s] , $\mathcal{C}' = 3.1 \cdot 10^{-4}, \tau = 3.5 \cdot 10^{-2}$ [s]

In Figure 5.11 a time trace of the simulated pressure differences is shown for $\overline{\overline{m}} = 2.1$ [kg/s]

and $\mathcal{S} = 0.20$. Hardly any difference is found between the conventional and improved model compared to the measured pressure difference.
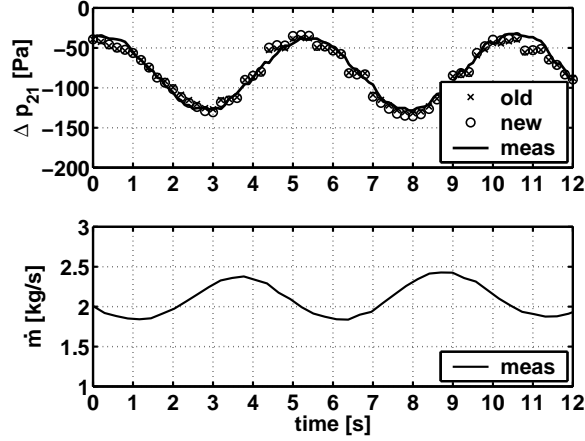
Figure 5.11: Simulation of the straight channel flow. $\overline{\dot{m}} = 2.1$ [kg/s], $f_o = 0.20$ [Hz], and $\mathcal{S} = 0.20, \mathcal{C}' = 3.1 \cdot 10^{-4}, \tau = 3.5 \cdot 10^{-2}$ [s]

5.4.2   divergent channel at $\overline{\dot{m}} = 2.1$ [kg/s]

conventional model

Simulations of the flow in the divergent channel with the conventional model (old) are shown in Figures 5.12 for $\overline{\dot{m}} = 2.1$ [kg/s]. For $0.07 < \mathcal{S} < 0.7$, the simulated amplitude of the pressure difference is larger than the measured pressure difference and the phase of the simulation lags the measurement.

improved model

The boundary-layer of the divergent channel flow develops, due to the adverse pressure gradient, from the inlet to the outlet more rapidly than the straight channel boundary-layer. It, therefore, is difficult to determine the boundary-layer thickness that should be used in the divergent channel. At one oscillation frequency, for $\overline{\dot{m}} = 2.1$ [kg/s] and $\mathcal{S} = 0.27$, the $\mathcal{C}'$ and τ are fitted such that the simulation with the improved model agrees with the experimental result. In Figure 5.13(a) it is seen that for

$$\mathcal{C}' = 1.7 \cdot 10^{-3} \text{ and } \tau = 1.4 \cdot 10^{-1} \text{ [s]}$$

the new simulation agrees, concerning the amplitude and phase of the pressure difference, better than the old simulation with the measurement. The fitted $\mathcal{C}'$ and τ, with $\alpha_r = 20$, correspond to an equivalent boundary-layer thickness of $\delta_s = 3.0 \cdot 10^{-3}$ [m], which is physically realistic.

Next, the fitted $\mathcal{C}'$ and τ are applied to the available data at the other oscillation frequencies. As an example, in Figure 5.13(b) the time trace for $\overline{\dot{m}} = 2.1$ [kg/s] and $\mathcal{S} = 0.14$ is show. It

(a) ○: measurement, ●: conventional simulation

(b) comparison measurement and conventional simulation
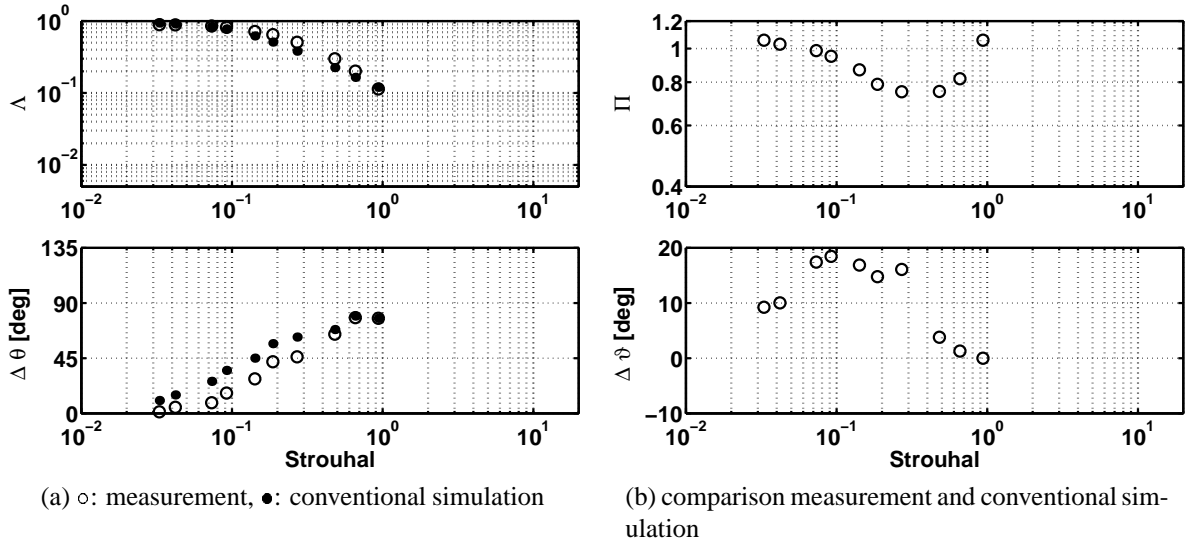
Figure 5.12: Measurement and conventional model results of the divergent channel flows. $\overline{\dot{m}} = 2.1$ [kg/s]

(a) fitted simulation. $f_o = 0.30$ [Hz], $\mathcal{S} = 0.27$

(b) $f_o = 0.15$ [Hz], $\mathcal{S} = 0.14$
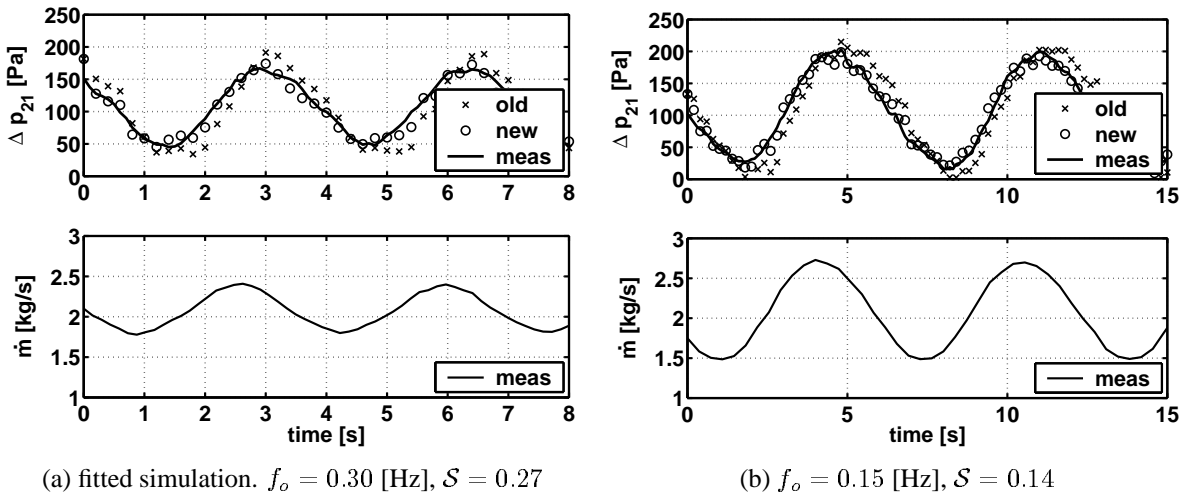
Figure 5.13: Simulations of the divergent channel flow. $\overline{\dot{m}} = 2.1$ [kg/s], $C' = 1.7 \cdot 10^{-3}$, $\tau = 1.4 \cdot 10^{-1}$ [s]

is seen that the improved model also works at this frequency. In Figure 5.14 the simulation results at all Strouhal numbers are shown. Compared to the conventional model, the pressure difference amplitude ratio is much closer to one and the phase is closer to the measured phase for $0.1 < \mathcal{S} < 0.8$. For $\mathcal{S} < 0.1$, especially the phase is adjusted with the new method, while the pressure difference amplitude ratio is hardly influenced. For $\mathcal{S} > 0.9$ the measured pressure difference is uncertain, due to a resonance in the connection tube positioned between the pressure sensor and the channel. So, for this range, no conclusion on the simulation result can be drawn.
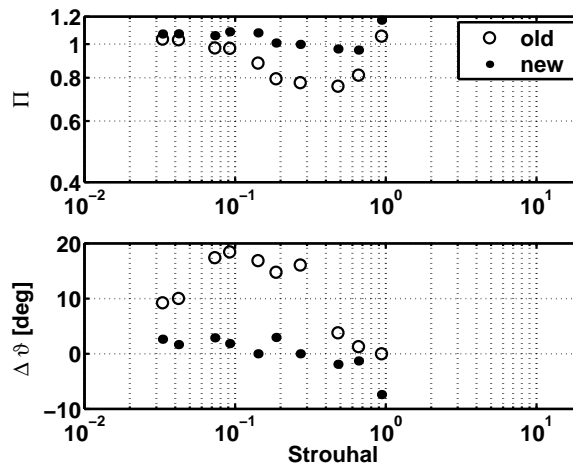
Figure 5.14: Comparison measurement and simulation for the divergent channel. $\dot{m} = 2.1$ [kg/s], $C' = 1.7 \cdot 10^{-3}, \tau = 1.4 \cdot 10^{-1}$ [s]

5.4.3 divergent channel at $\overline{\dot{m}} < 2.1$ [kg/s]

conventional model

In Figure 5.15 the simulation results with the conventional model for various mass flows are shown. An evaluation of the Π-values at the different mass flows shows that they do not correlate
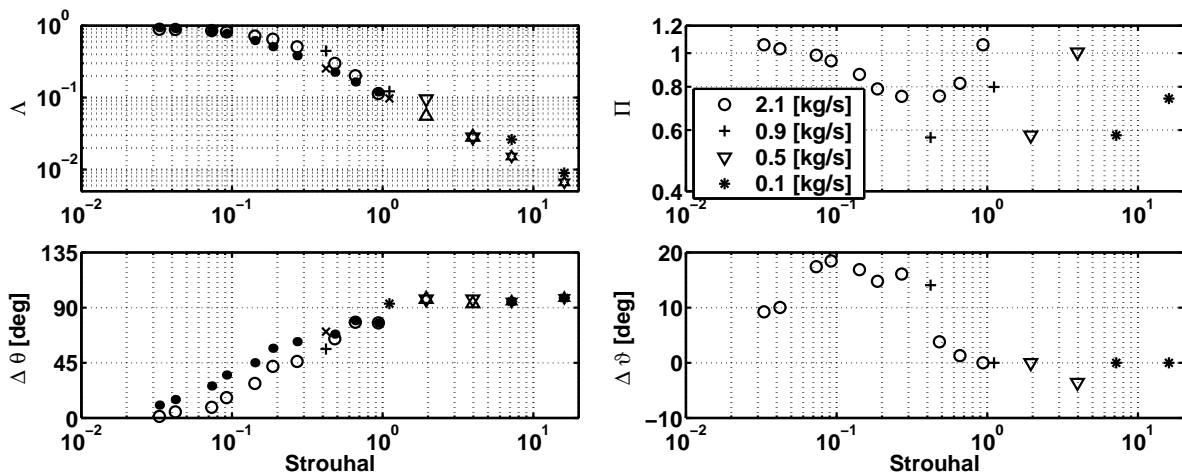
(a) result measurement and conventional simulation.

(b) comparison measurement and conventional simulation

$\overline{\dot{m}}$ **[kg/s]**	2.1	0.9	0.5	0.1
measurement	○	+	▽	∗
conventional simulation	●	×	△	⋆

Figure 5.15: Measurement and conventional model results of the divergent channel flows for various mass flows.

with the Strouhal number. On the other hand, the $\Delta\vartheta$-values do correlate with the Strouhal number. Three causes of the deviation of the Π-values can be indicated:

First, the Strouhal scaling might not be the right parameter to compare the simulated pressure difference with the measured pressure difference. Therefore, in Figure 5.16(a) the comparison of the simulation with the measurement is shown versus the frequency. As can be seen, some amplitude ratios, for $\dot{m} = 0.9$ [kg/s] and $f_o = 0.5$ [Hz], and $\dot{m} = 0.5$ [kg/s] and $f_o = 1$ [Hz], coincide with the amplitude ratios of $\dot{m} = 2.1$ [kg/s]. Others, turn out with a smaller Π than for $\dot{m} = 2.1$ [kg/s]. So, not all data correlates with the frequency.

Second, for measurements at about $f_o = 1$ [Hz] the mass flow fluctuation becomes very small and the number of data points obtained with the PIV method is small. This introduces an uncertainty in the measured mass flow at the largest frequencies. Since the derivative of the measured mass flow is used as input to the model it is expected to affect the simulation results significantly. This might explain the deviation of the $\dot{m} = 0.1$ [kg/s] and $f_o = 1.0$ [Hz] point. Furthermore, for $f_o \geq 1.0$ [Hz] a resonance in the pressure sensor ducts exists, which influences the pressure difference measurement.

Third, a physical argument can be given for data points for which the mass flow amplitude ratio M is nearly 1. Here the oscillation amplitude of the mass flow is as large as the mean mass flow and flow patterns, as large scale separation, can exist. These are not taken into account in the model. In Figure 5.16(b) Π is shown versus M. In Table 5.2 the division of the data points

<p align="center">Table 5.2: Division of data points based on M and Π.</p>

	$\overline{\dot{m}}$ [kg/s]	f_o [Hz]
M $<$ 0.2 then	2.1	all
0.7 $<$ Π $<$ 1.2	0.9	0.5
	0.5	1.0
M $>$ 0.2 then	0.9	0.2
Π $<$ **0.7**	0.5	0.5
	0.1	0.5
(exceptional Π $>$ **0.7**)	(0.1)	(1.0)

based on M and Π is summarized. Overall, it is seen that the value of Π depends on M. For small M-values, $M < 0.2$, the pressure difference amplitude ratio is $0.7 < \Pi < 1.2$, while for the larger M-values, $M > 0.2$, the pressure difference amplitude ratio is $\Pi < 0.7$. (An exception exists for $\dot{m} = 0.1$ [kg/s] and $f_o = 1.0$ [Hz].)

In Figure 5.16(b) it is seen that the phase difference, $\Delta\vartheta$, does not depend on M. In Figure 5.16(a) and Figure 5.15(b) it is seen that the phase difference depends on either the frequency of the oscillation or the Strouhal number. Due to the inaccuracy in determining the phase this cannot be made up.

It is concluded that the difference between the conventional simulation phase and the measured phase is determined by the Strouhal number (or frequency), while the difference in amplitude of the pressure difference is determined by the frequency as well as by the flow in the channel, which is expressed by the quantity M.

(a) versus frequency

(b) versus M, ratio of the amplitude of the mass flow and the mean mass flow
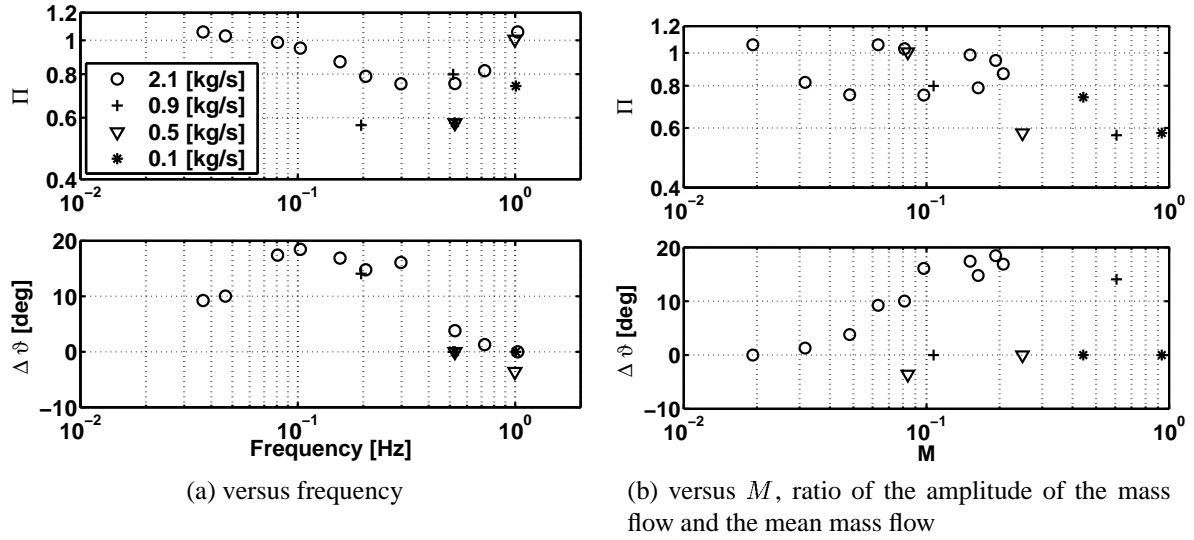
Figure 5.16: Comparison between measurement and conventional simulation for the divergent channel for various mass flows.

More experiments at different mass flows should be performed to exactly define the parameters that determine the variation in amplitude ratio and $\Delta\theta_{\text{measurement}}$ at different mean mass flow oscillations.

improved model

To be able to apply the new approach to the other mean mass flows in the divergent channel, it should be noted that the (steady) boundary layer thickness depends on the velocity of the flow. To take into account, to a certain extent, this dependence the turbulent boundary-layer thickness at a certain x-position for a flat plate, according to ([64]):

$$\delta_s = 0.37\, x^{4/5} \left(\frac{\nu}{\overline{u}}\right)^{1/5},$$

is used. The boundary-layer thicknesses for the other mean mass flows are determined from the boundary-layer thickness, $\delta_1 = 3.0 \cdot 10^{-3}$ [m] and velocity $\overline{u}_1 = 0.5$ [m/s] at $\overline{m} = 2.1$ [kg/s] according to:

$$\delta_s = \delta_1 \left(\frac{\overline{u}_1}{\overline{u}}\right)^{1/5}.$$

In Figure 5.17 the resulting turbulent boundary-layer thickness nondimensionalised with half the channel height, $d/2$, is shown with respect to the mean mass flow. For mass flow of $\approx$ 0.1 [kg/s] the boundary-layer thickness almost covers half the channel height. The boundary-layer thickness becomes thinner as the mass flow increases.

The values for $\mathcal{C}'$ and τ are functions of δ_s and are calculated according to Equation (5.4). The simulation results with the correction for the other mean mass flows in the divergent channel
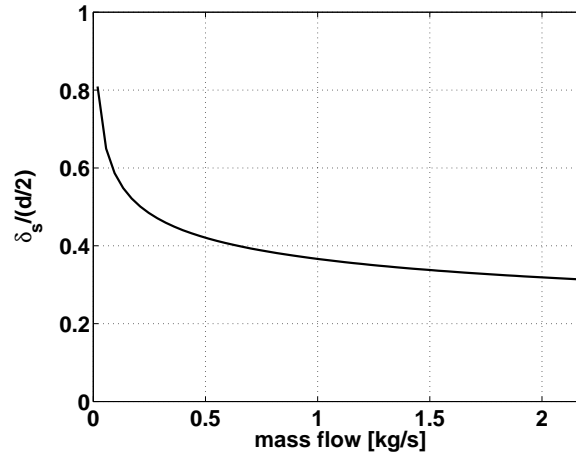
Figure 5.17: Turbulent boundary-layer thickness with respect to the mean mass flow in the case of a flat plate.

for different Strouhal numbers are shown in Figure 5.18(a) and reveal a small improvement of the amplitude and phase. In Figure 5.18(b) the comparison is shown versus the mass amplitude ratio, M. As can be seen, for $M \leq 0.2$, the pressure difference amplitude ratio, Π, is for the new simulation improved such that the pressure difference amplitude becomes almost equal to the measured pressure difference amplitude. A time trace for $\overline{m} = 0.9$ [kg/s], $\mathcal{S} = 1.1$, $M = 0.11$ is shown in Figure 5.19(a), which shows that the conventional (old) model already is close to the measured pressure difference. Nevertheless, according to Figure 5.18 the improved (new) model simulates a pressure difference that is even closer to the measured pressure difference.

For $M > 0.2$ the correction in the improved model is not enough to become equal to the measured pressure difference amplitude (i.e. $\Pi = 1$). In Figure 5.19(b) a time trace for $\overline{m} = 0.9$ [kg/s], $\mathcal{S} = 0.42$, $M = 0.61$ is shown. The overpredicted pressure difference amplitude is clearly seen.

5.5   Discussion

In this chapter a model developed for a fully-developed laminar flow is applied to a turbulent inlet flow. With simulations, for both a straight and a divergent channel, it is shown that the measurements can be simulated better if a correction on the conventional momentum equation is used. Especially, for the divergent channel, in which the flow is exposed to an adverse pressure gradient, the simulations show an adjustment of the amplitude ratio and a well-captured phase between the oscillating mass flow and pressure. This improvement depends on the mass flow amplitude ratio, M, and works best for small M.

The correction needed in the straight channel is small. This is explained by the fact that the Stokes number for the straight channel is between $0.7 < \alpha < 3.8$, which is mainly smaller than the Stokes number $\alpha_{co} = 2$, for which no relaxation equation is needed. This is also seen in the small time constant, $\tau = 3.5 \cdot 10^{-2}$ [s], which suggests that a correction without the relaxation
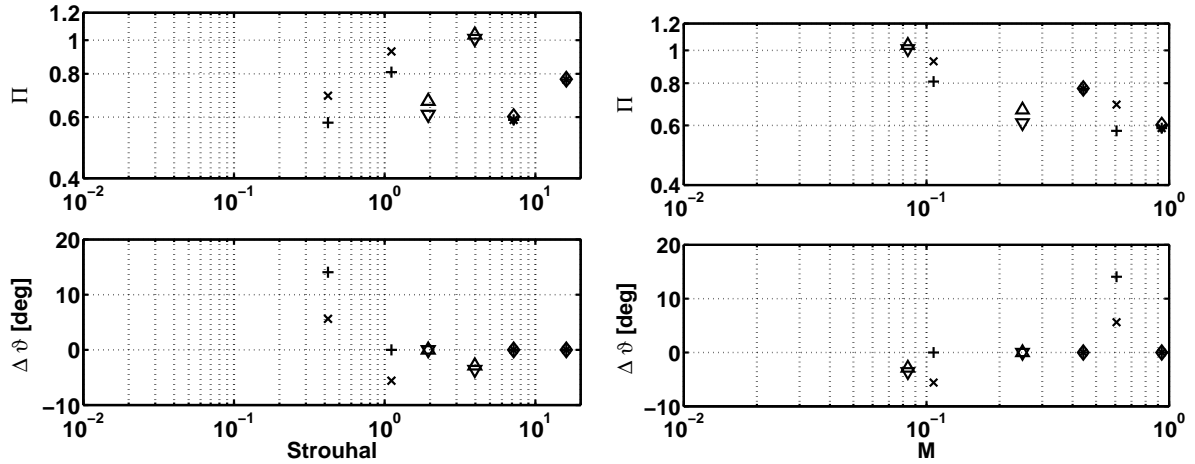
$\overline{\dot{m}}$ [kg/s]	0.9	0.5	0.1
old	$+$	$\triangledown$	$*$
new	$\times$	$\triangle$	$\diamond$

Figure 5.18: Comparison measurement and simulation for the divergent channel for $\overline{\dot{m}} < 2.1$ [kg/s]. C', τ depend on mean mass flow.
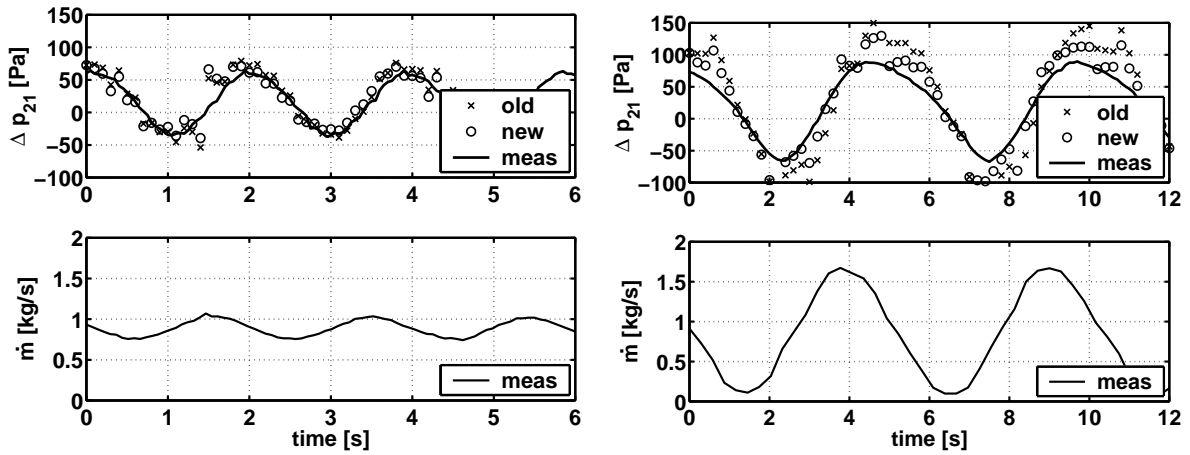
Figure 5.19: Simulations of the divergent channel flow. $\overline{\dot{m}} = 0.9$ [kg/s], $C' = 2.3 \cdot 10^{-3}$, $\tau = 1.9 \cdot 10^{-1}$ [s]

equation of the correction term can be solved, i.e,:

$$\frac{d\dot{m}}{dt} = -\frac{A}{L} \{\Delta p - \Delta p_{ss}\} + D \frac{d\dot{m}}{dt},$$

$$D = \mathcal{C} \frac{\delta_s^2}{(d/2)^2} \frac{h^2 A}{\nu L} \frac{d\Delta p_{ss}}{d\dot{m}}. \tag{5.5}$$

This can be rewritten to:

$$\frac{d\dot{m}}{dt} \;=\; -\frac{A}{L\,(1-D)} \;\{\Delta p \,-\, \Delta p_{ss}\} \; .$$

This result shows that the introduced correction can be translated to an adjustment of the geometrical parameter A or L. In the case of the straight channel the maximum value of $D = -0.1$, which means that simulations with the conventional approach would become close to the measurements if L is taken 10 % larger or A is taken 10 % smaller. This adjustment of a geometrical parameter is a well-known practice in compressor surge modelling, *[1], [30], [70]*. Often the length of the compressor duct is taken as a fit parameter and is adjusted such that the surge frequency of the simulations matches the measured surge cycle. A drawback of the resulting 'duct length' is that it is no longer a geometrically determined quantity and cannot be physically appointed anymore. The success of the fitting suggests that the Stokes numbers of these compression systems are small and that the relaxation equation in the correction equation can be omitted. The Stokes number for the divergent channel is between $1.5 < \alpha < 7.5$, which means that for this channel the relaxation equation cannot be omitted.

For the divergent channel measurements and simulations are performed at different mean mass flows, $\overline{\dot{m}} \leq 2.1$ [kg/s]. It is seen that the improved model, with $\alpha_r = 20$ and an appropriate value for the boundary-layer thickness, simulates the measured pressure difference better than the conventional model if the mass flow amplitude ratio, $M \leq 0.2$. Although, more experiments are required to determine the exact cause of the variation in pressure difference amplitude ratio and phase at different mean mass flow oscillations a suggestion is given based on the data available. The correction that is developed and applied in the improved model represents the contribution of the unsteady viscous term in the unsteady momentum equation. Omitted is the contribution of the non-linear convective term, which can become important in a pressure gradient flow. Especially, for mass flow amplitudes that become as large as the mean mass flow the non-linear character of the convective term becomes important to model. The current models do not take into account the unsteady contribution of the convective term and might therefore produce incorrect results for oscillations with a larger mass flow amplitude ratio.

In Chapter 3 the compressor flow is simulated with the conventional model. It is concluded that the simulated maximum pressure rise is lower compared to the measured maximum pressure rise. In this chapter it is seen that the improved model has an influence on the amplitude of the simulated pressure. Therefore, it seems a promising tool to be used in the simulations of the compression system. In the next chapter the improved approach is applied to the compression system.

Chapter 6

Improved model applied to the compression system

In Chapter 3 the simulation with a lumped parameter model, in which a quasi-steady compressor performance is assumed, shows a larger surge frequency and a lower maximum pressure rise than the measurement. Due to the short duct length the inertia of the system is small and, during the pressurization period, the steady-state characteristic is followed. This results in a lower simulated maximum pressure rise. If the compressor performance is extracted from measured transient surge data, it is found that the unsteady compressor performance only slightly differs from the measured plenum pressure data. Therefore, to obtain better simulation results, the assumption of a quasi-steady compressor performance should be abandoned and an unsteady compressor performance representation should be used. In this chapter the correction method developed in Chapter 4 is applied to the compression system.

6.1 Governing equations

The need to apply the correction to the model depends on the Stokes number of the studied system (Equation (4.1)):

$$\alpha = \frac{h}{2} \sqrt{\frac{2\pi f_s}{\nu}} \,.$$

In Chapter 2 it is shown that the measured surge frequency is between $18 < f_s < 23$ [Hz]. The kinematic viscosity in the compressor is $\nu = 1.5 \cdot 10^{-5}$ [m^2/s] and the boundary-layer thickness is assumed to equal the half width of the outlet of the compressor (Table 2.1), $h = 7 \cdot 10^{-3}$ [m]. The Stokes number now is:

$$9.6 < \alpha < 10.9 \,.$$

Since the Stokes number is in the correction range $0.5 < \alpha < 80$, see Table 4.2, the correction should be applied to this compression system. In addition, the relaxation equation is required since the Stokes number is larger than $\alpha_{co} = 2$.

The set of equations that describes the compression system consists of the rate of change of the compressor and throttle valve mass flows, represented by conservation of momentum for an incompressible flow in a duct, Equations (3.1) and (3.2), and the rate of change of the plenum pressure, represented by a mass balance in the plenum, Equation (3.3). These are extended with the correction Equation (4.21) and Equation (4.22) to account for an unsteady compressor performance:

$$
\begin{aligned}
\frac{d\dot{m}_c}{dt} &= -\frac{A_c}{L_c}\left\{p_p - p_0 - \Delta p_c\right\} + \chi, \\
\frac{d\dot{m}_T}{dt} &= -\frac{A_T}{L_T}\left\{p_0 - p_p + \Delta p_T\right\}, \\
\frac{dp_p}{dt} &= \frac{a_p^2}{V_p}\left\{\dot{m}_c - \dot{m}_T\right\}, \\
\tau\frac{d\chi}{dt} &= \mathcal{C}'\,\frac{h^2\,A_c}{\nu\,L_c}\,\frac{d\Delta p_c}{d\dot{m}_c}\,\frac{d\dot{m}_c}{dt} - \chi.
\end{aligned}
\tag{6.1}
$$

The geometry values A_c, L_c, A_T, L_T, and V_p are shown in Table 3.2. The compressor and throttle characteristic Δp_c and Δp_T are determined in Chapter 3 and Chapter 2, respectively. The remaining parameters to be determined are $\mathcal{C}'$ and τ.

6.2   Parameters $\mathcal{C}'$ and τ

The geometry of the centrifugal compressor produces a complex flow field. Since the parameters $\mathcal{C}'$ and τ depend on boundary-layer thickness of the compressor they are difficult to determine in such a flow field. The growth of the boundary-layer in the compressor depends on the flow path through the compressor *[59]*. First, the flow path through the compressor changes from one frame of reference to another. Second, the flow is curved from axial to radial direction, which introduces secondary flow movement of fluid. Third, there exists an adverse pressure gradient, which quickens the growth of the boundary-layer thickness. Starting from the idea that the compressor can be modelled as a rectangular duct, and a turbulent boundary-layer growth as on a flat plate can be applied, the thickness would increase from zero at the inlet to $\delta_{0.16} = 5.8 \cdot 10^{-3}$ [m] at the outlet of the compressor. This thickness exceeds the smallest half width at the outlet of the compressor $h/2 = 3.5 \cdot 10^{-3}$ [m]. Therefore, it is assumed that the boundary-layer fluid occupies the whole width at the compressor outlet, i.e., $\delta = h/2$, *[10]*.

The parameters $\mathcal{C}'$ and τ depend on the relevant boundary-layer thickness according to Equation (5.4). Assuming that the relevant boundary-layer thickness equals the half width of the smallest passage in the compressor the parameters become:

$$
\begin{aligned}
\mathcal{C}' &= \mathcal{C}\,\frac{\delta_s^2}{(h/2)^2} &&= 1/60, \\
\tau &= \frac{2\pi\,\delta_s^2}{\alpha_r^2\,\nu} &&= 1.28 \cdot 10^{-2} \text{ [s]}.
\end{aligned}
\tag{6.2}
$$

Herein, $C = 1/60$ and $\alpha_r = 20$ are taken to be equal to the value found for the analytically solved channel flow, which is tabulated in Table 4.2.

In Section 3.2 two criteria are used to determine whether the measured surge cycle is approached well by the simulation, that are the simulated surge frequency and maximum pressure rise. In Figure 6.1 the two criteria are shown with respect to the parameters C' and τ. Since the combination of C' and τ as suggested in Equation (6.2) does not give the right surge frequency and maximum pressure rise, the simulations are performed at a small C' (which gives good results for the τ-value) and a large C'. Generally, it is seen that for a certain τ the surge frequency decreases and the maximum pressure rise increases for increasing C'. The effect of an increasing τ for a certain C' is opposite. Comparing these results with results presented in Figure 3.5 an increase of C' or a decrease of τ has the same effect on the frequency and maximum pressure rise as increasing the duct length, L_c, or decreasing the volume, V_p. Nevertheless, the surge

(a) surge frequency for small C'

(b) maximum pressure for small C'

(c) surge frequency for large C'

(d) maximum pressure for large C'
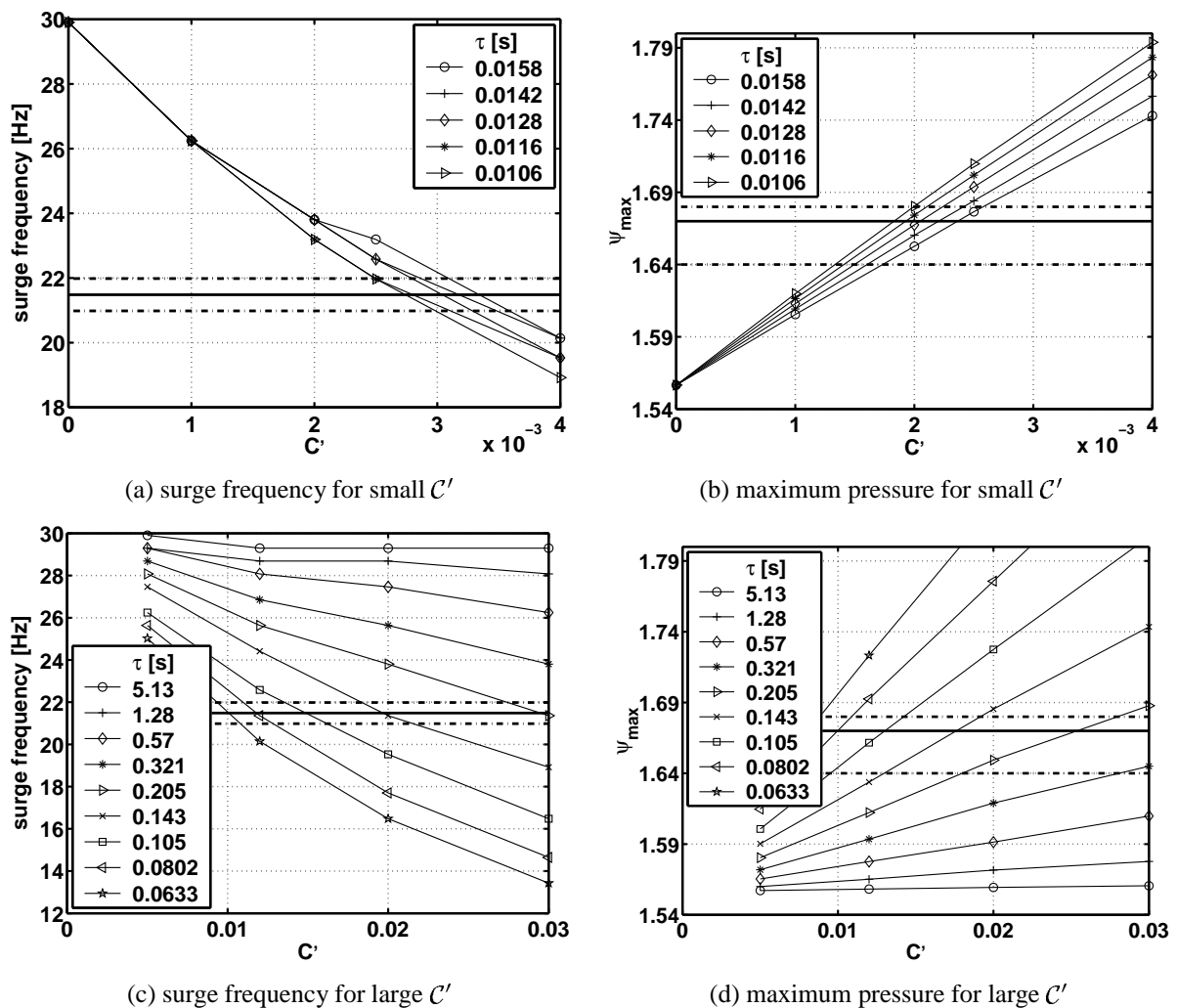
Figure 6.1: Simulation parameters versus the parameter C' for different τ. $L_c = 0.16$ [m], $V_p = 2.39 \cdot 10^{-2}$ [m^3], $N = 20100$ [rpm], $Y_T = 0.28$, –: measured value with uncertainty indicated by $\cdots$

(a) surge cycle. $\mathcal{C}' = 2.5 \cdot 10^{-3}, \tau = 1.28 \cdot 10^{-2}$ [s]
($\mathcal{C}'/\tau = 0.20$ [s^{-1}])

(b) surge cycle. $\mathcal{C}' = 2.0 \cdot 10^{-2}, \tau = 1.43 \cdot 10^{-1}$ [s]
($\mathcal{C}'/\tau = 0.14$ [s^{-1}])
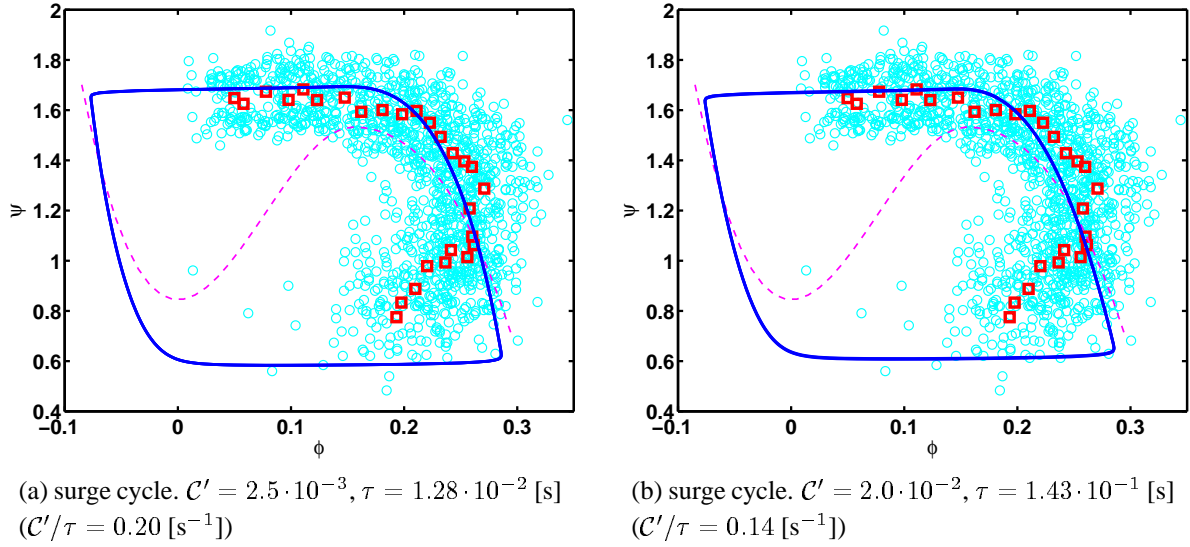
Figure 6.2: Simulation results for two different sets of values for $\mathcal{C}'$ and τ. $L_c = 0.16$ [m], $V_p = 2.39 \cdot 10^{-2}$ [m^3], $N = 20100$ [rpm], $Y_T = 0.28$, ○: valid parts of 50 measured surge cycles, □: mean measured values, - -: steady-state characteristic, –: simulation

cycle does not change from a deep surge cycle to a classic surge cycle in the case $\mathcal{C}'$ is increased or τ is decreased. In Figure 6.2 it is seen that an increase of $\mathcal{C}'$ results in practically the same cycles. So, the correction parameters do not influence the inertia of the system as the duct length does. The measurement results are shown for reference and will be discussed in the next section.

The points of intersection of the simulated lines with the measured values in Figure 6.1 are shown in Figure 6.3. Remarkable is that there exists a relation between the parameters $\mathcal{C}'$ and τ. A linear fit is plotted for the intersection points of both surge frequency, f_s, and maximum pressure rise, ψ_{max}. Both ratios are nearly the same, $\mathcal{C}'/\tau|_{f_s} = 0.12$ [s^{-1}] and
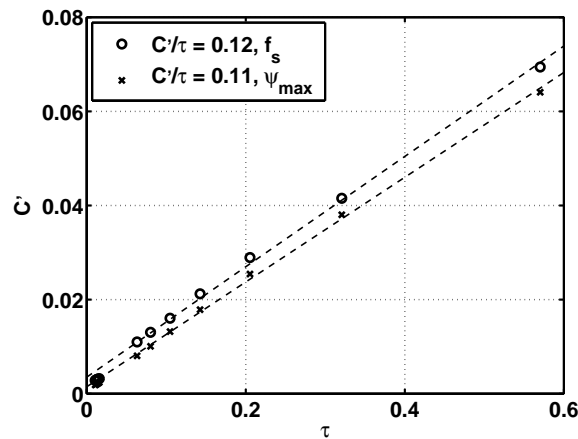
Figure 6.3: Points of intersection of the simulated and measured surge frequency and maximum pressure rise. $L_c = 0.16$ [m], $V_p = 2.39 \cdot 10^{-2}$ [m^3], $N = 20100$ [rpm], $Y_T = 0.28$

$\mathcal{C}'/\tau\big|_{\psi_{max}} = 0.11 \ [\text{s}^{-1}]$.

The ratio $\mathcal{C}'/\tau$ can be determined analytically, with Equation (6.2):

$$\left. \frac{\mathcal{C}'}{\tau} \right|_a = \frac{\mathcal{C} \, \alpha_r^2 \, \nu}{(h/2)^2 \, 2\pi} \ ,$$

and is independent of the boundary-layer thickness δ. Using: $\mathcal{C} = 1/60$, $\alpha_r^2 = 20$, $\nu = 1.5 \cdot 10^{-5} \ [\text{m}^2/\text{s}]$, $h = 7 \cdot 10^{-3} \ [\text{m}]$, this analytical ratio becomes $\mathcal{C}'/\tau\big|_a = 1.3 \ [\text{s}^{-1}]$. This is one order of magnitude larger than the value obtained from the simulations. This difference could be brought about by the interpretation of the length scale h, which is taken to be the smallest passage at the outlet of the compressor. Another length scale that can be used is, e.g., based on the (mean) hydraulic diameter of the compressor passage. This diameter will be larger than the smallest passage of the compressor and thus a smaller $\mathcal{C}'/\tau\big|_a$ will be obtained.

Furthermore, $\mathcal{C}$ and α_r^2 are based on values derived for a fully-developed oscillating laminar flow in a straight channel. In the compressor the flow is turbulent and rather complex that influences the specification of $\mathcal{C}$ and α_r^2. For example, in the definition of α_r^2 and the ratio $\mathcal{C}'/\tau\big|_a$ the laminar kinematic viscosity is used which actually should be represented by the value for the 'turbulent-viscosity' appropriate for the compressor. To know more about these parameters in compressors they should be studied in various kind of machines.

6.3 Results improved model

In this section, the simulations are compared with measurements explained in Section 2.6 for two rotational speeds. The reference measurements are shown in Figure 2.16(b) for $N = 20100$ [rpm] and Figure 2.18(b) for $N = 23200$ [rpm]. First, the simulation results for $N = 20100$ [rpm] are discussed. Figure 6.4(a) shows the surge cycle in the compressor map obtained with the conventional model in which the compressor performance is taken to be quasi-steady. Figure 6.4(b) shows the surge cycle obtained with the correction method. If in Equation (6.1) χ is added to the steady-state compressor performance Δp_c, an adjusted characteristic is obtained:

$$\Delta p_{c \ adjusted} = \Delta p_c + \frac{\chi \, L_c}{A_c} \ .$$

Herein, is χ a measure for the correction that is needed to account for the difference between the steady-state performance and the (real) unsteady performance of the compressor. As can be seen, the adjusted compressor characteristic is mainly larger at the pressure rise extremes of the steady-state characteristic. Apparently, at the maximum pressure rise the losses for the transient flow are smaller than for the fully-developed flow.

The simulation with correction, with $\mathcal{C}'/\tau = 0.14 \ [\text{s}^{-1}]$, shows that the pressure follows during the pressurization and pressure drop period the adjusted compressor characteristic instead of the steady-state characteristic. Compared to the simulation without correction the pressure rise extremes are larger and approaches the measured maximum pressure rise better.

The time traces of the simulation without and with correction are shown in Figure 6.4(c) and 6.4(d), respectively. First, it is seen that with the correction the measured surge frequency

(a) surge cycle **without** correction. ○: valid parts of 50 measured surge cycles, □: mean measured values, - -: steady-state characteristic, –: simulation

(b) surge cycle **with** correction. ○: valid parts of 50 measured surge cycles, □: mean measured values, - -: steady-state characteristic, ⋯: adjusted characteristic, –: simulation

(c) time trace of the pressure rise and mass flow **without** correction. symbols: valid / invalid parts of measurement, –: simulation

(d) time trace of the pressure rise and mass flow **with** correction. symbols: valid / invalid parts of measurement, –: simulation

Figure 6.4: Comparison of simulation results **without** and **with** correction ($\mathcal{C}' = 2.0 \cdot 10^{-2}$, $\tau = 1.43 \cdot 10^{-1}$ [s], $\mathcal{C}'/\tau = 0.14$ [s^{-1}]). $N = 20100$ [rpm], $Y_T = 0.28$, $L_c = 0.16$, $V_p = 2.39 \cdot 10^{-2}$ [m^3]

is found. Furthermore, the pressure trace with correction shows a good similarity with the measurements for the pressurization as well as for the pressure drop period. The measured mass flow trace is rather uncertain and therefore it is difficult to determine whether it is better simulated with or without correction.

The results of simulations for $N = 23200$ [rpm] are shown in Figure 6.5. The time traces show that the simulated surge frequency, $f_s = 18.9$ [Hz], is not exactly equal to the measured surge frequency, $f_s = 20.5$ [Hz]. The pressure rise trace is, especially at its extremes, rather good. Nevertheless, in the compressor map at the top of the compressor performance the relatively low

pressure is not captured and the maximum pressure rise is a little higher than the measured one. To be able to model the flow at the pressure dip in the maximum pressure rise area, more should be known about the flow phenomenon that causes it. This requires detailed measurements of the compressor flow field.
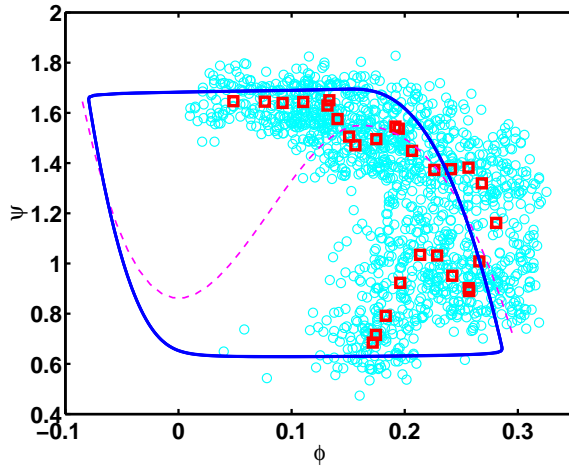
(a) surge cycle. $\mathcal{C}'/\tau = 0.14$ [s^{-1}], $\circ$: valid parts of 50 measured surge cycles, $\square$: mean measured values, - -: steady-state characteristic, -··-: adjusted characteristic, –: simulation
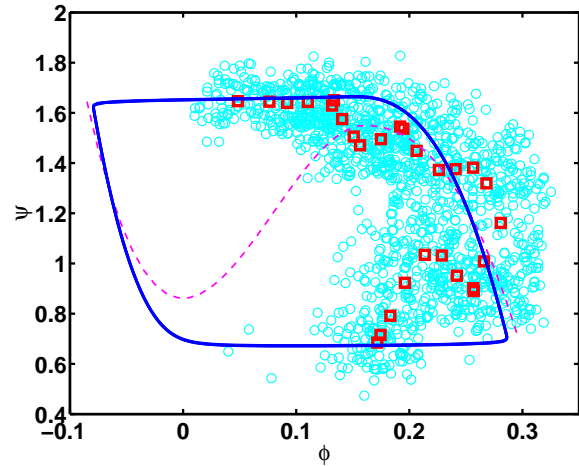
(b) surge cycle: $\mathcal{C}'/\tau = 0.11$ [s^{-1}], $\circ$: valid parts of 50 measured surge cycles, $\square$: mean measured values, - -: steady-state characteristic, -··-: adjusted characteristic, –: simulation
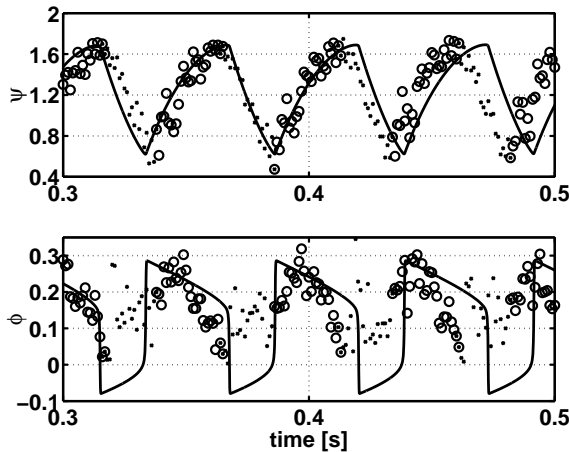
(c) time trace of the pressure rise and mass flow. $\mathcal{C}'/\tau = 0.14$ [s^{-1}], symbols: valid / invalid parts of measurement, –: simulation
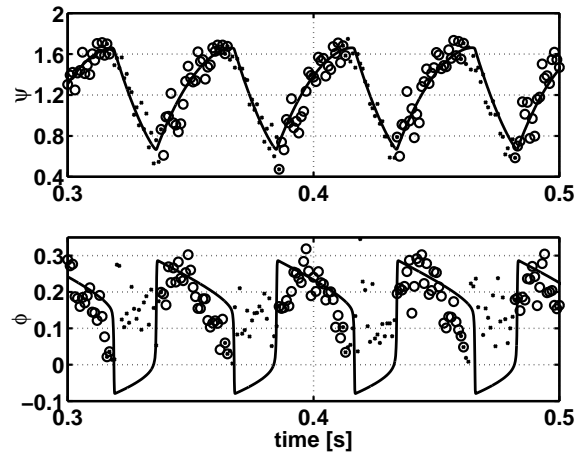
(d) time trace of the pressure rise and mass flow. $\mathcal{C}'/\tau = 0.11$ [s^{-1}], symbols: valid / invalid parts of measurement, –: simulation

Figure 6.5: Simulation results **with** correction. $N = 23200$ [rpm], $Y_T = 0.29$, $L_c = 0.16$ [m], $V_p = 2.39 \cdot 10^{-2}$ [m^3]

In Section 6.2 it is shown that the simulated frequency and maximum pressure rise depend on the parameters $\mathcal{C}'$ and τ. To improve the simulation for $N = 23200$ [rpm], the parameter $\mathcal{C}'$ is adapted. With $\mathcal{C}' = 1.5 \cdot 10^{-2}$ ($\tau = 1.43 \cdot 10^{-1}$ [s]) the frequency and maximum pressure rise are in better agreement with the measurements, see Figure 6.5. The ratio of the parameters then is changed from $\mathcal{C}'/\tau = 0.14$ [s^{-1}] to $\mathcal{C}'/\tau = 0.11$ [s^{-1}], which is within the range this ratio

can be determined. This shows that the characteristics of the simulated surge cycles are very sensitive to the value of the ratio $\mathcal{C}'/\tau$.

6.4 Discussion

In Table 6.1 a summary of the presented models with respect to fully-developed surge simulation is shown. These values are mainly determined for $N = 20100$ [rpm], $Y_T = 0.28$. In this thesis the surge cycle shape, surge frequency, and maximum pressure ratio are three criteria to determine whether the measured surge cycle is approached well by the simulation. All variations on the conventional lumped parameter model, i.e., with physical based parameters, matched parameters, and with a transient compressor response, show for some criteria a similarity with the measured surge cycle, but not for all three.

Table 6.1: Comparison of the discussed models with respect to the measured surge cycles .

Model	Parameters	$\frac{L_c}{V_p}$ [m^{-2}]	$\frac{\mathcal{C}'}{\tau}$ [s^{-1}]	Equation	Figure	Surge cycle shape	Surge frequency	Max surge pressure ratio
Conventional								
(a)	physical	6.7	-	(3.1), (3.2), (3.3)	3.4	OK	too large	too small
(b)	matched	70	-	as *(a)*	3.6	dis-similar	OK	OK
(c)	physical	6.7	-	as *(a)* + (3.11)	3.9	OK	too large	smaller than *(a)*
Improved								
(d)	physical	6.7	0.1− 0.2	(6.1)	6.2, 6.5	OK	OK	OK

(a)	conventional lumped parameter model
(b)	conventional lumped parameter model with matched L_c and V_p
(c)	conventional lumped parameter model with transient compressor response
(d)	improved lumped parameter model

On the other hand, the improved lumped parameter model with a quasi-steady compressor performance and a correction, to take into account the dynamic character of the compressor performance, captures the dynamics of the pressurization period of the flow during surge and the surge frequency. Instead of matching geometrical parameters like the compressor duct length or the plenum volume, which have to be determined for every compression system, one single parameter, $\mathcal{C}'/\tau$, is found. This ratio, which is obtained on physical grounds, represents the correction that is needed to account for the transient performance of the compressor itself and depends solely on the geometrical dimensions, the gas viscosity and the relaxation frequency.

Therefore, this ratio depends on the compressor instead of on the compression system in which the compressor operates. The ratio has to be determined only once after which it can be used in every compression system set-up. In principle, the ratio depends on the geometry of the compressor. Nevertheless, a small variation of the ratio is found for different rotational speeds. To find out which geometrical parameters determine the unsteady flow field in the compressor and which parameters determine the ratio more research should be performed on various kinds of compressors.

Due to an unsteady flow the performance of the compressor becomes steeper, especially, near its pressure rise extremes. This influences the stability prediction of the system, which is interesting in the case surge initiation is studied. Since, surge is commonly encountered during speed transients and set point changes, the correction term will influence the stability of the system. Moreover, the correction term depends on the time scale of the transient. Therefore the stability of the system will depend on the time scale associated with the set point change. It is of interest to investigate the initiation of surge with the developed model. Since, if the initiation of surge is captured correctly in a simulation, surge controllers can be designed to control the surge before the disturbances in the system grow into undesired large pressure oscillations.

Chapter 7

Conclusions and recommendations

7.1 Conclusions

In this thesis compression system surge is studied by means of experiments on a laboratory gas turbine installation and with use of a lumped parameter model. In the modelling special attention is paid to the unsteady performance of the compressor. The simulation results with the new developed correction term are, compared to the conventional model results, in better agreement with measurements.

Pressure measurements at the outlet of the compressor show that the surge frequency of the compression system increases with decreasing throttle valve setting. Furthermore, for a certain throttle valve setting a small influence of the rotational speed is found, i.e., the surge frequency decreases as the rotational speed is increased. The dependence of the surge frequency on the operating condition of the compression system shows that the system experiences classic or deep surge, which is determined by the whole compression system.

To compare the simulated surge cycles with the measured surge cycles the maximum pressure rise amplitude and surge frequency can be used the best. Furthermore, with hot-wire measurements in the inlet of the compressor an impression of the positive flow period of the surge cycles is obtained. This impression can be used as an extra verification of the simulated surge cycles.

In the conventional model difficulties arise in determining the geometrical data of the compression system and the quasi-steady compressor characteristic such that the measured surge cycle frequency and maximum pressure rise are simulated. It is found that by fitting the equivalent duct length and the plenum volume the measured maximum pressure rise and surge frequency are reproduced. Then, the ratio of the compressor duct length and the plenum volume needs to be increased with a factor ten compared to the physical length and volume. Nevertheless, the shape of the surge cycle at the maximum pressure rise is simulated incorrectly. To simulate the measured constant pressure rise during decreasing mass flow a small compressor duct length is required, but then the maximum pressure rise is simulated lower compared to measurement.

To describe the compressor response to departure from steady-state, a relaxation of the compressor performance as suggested in literature by *Greitzer [31]* is applied . It is found that simulations with this relaxation equation show a lower maximum pressure rise than the simula-

tions without this equation. Apparently, this representation of the dynamics of the compressor flow is not applicable to the present flow problem.

The study of an oscillating fully-developed laminar channel flow yields a representation of unsteady flow performance based on physical arguments. Herein, a correction on a quasi-steady viscous approach is derived by extracting the quasi-steady solution from the exact solution obtained from the unsteady one-dimensional momentum equation. An important parameter in this study is the Stokes number (α), which characterizes the relative importance of the time-dependent inertia terms with respect to viscous terms. If this Stokes parameter is in the range $0.5 < \alpha < 80$ the correction on a quasi-steady approach should be applied.

Since only part of a Taylor series expansion is used for the correction, the correction should vanish for large Stokes numbers. Therefore, a relaxation equation is added for $\alpha > \alpha_{co} = 2$. The resulting model introduces two new parameters ($\mathcal{C}'$, τ) that depend on the Stokes number, and can be determined straightforwardly from the characteristic parameters of the channel flow. In addition, the relaxation time τ is a function of an appropriate Stokes number that appeared to be $\alpha_r = 20$.

The correction term is applied to a turbulent inlet flow, with and without an adverse pressure gradient. To be able to evaluate the simulations, experiments in a water channel facility are performed. The studied water channel flow has an inlet flow character which means that the flow is not fully-developed. Therefore, the length scale in the Stokes number is not equal to the channel height. Instead, the steady boundary-layer thickness is used. Although, it is difficult to determine this thickness for a developing flow, it is found that the length scale that gives the best simulation result is of the order of magnitude of the measured steady boundary-layer thickness. Besides, also here $\alpha_r = 20$ appears to be appropriate.

Especially, for the adverse pressure gradient flow a difference between the simulations with the conventional model and experiments is found. Dependent on the mass flow amplitude ratio, M, the simulations with the improved model result in an amplitude ratio and a phase, of the mass flow and pressure that agree with the experimental results. For $M > 0.2$ both the conventional model and the improved model simulate a larger pressure difference amplitude compared to the measured oscillation pressure difference.

Generally speaking, the water channel experiments and modelling show that the derived correction for a relatively simple configuration and a laminar flow can be applied to a flow at a higher Reynolds number and with an inlet flow character. In addition to the dependence on the Stokes number, a dependence on the mass flow amplitude ratio is found.

The improved model is applied to the compression system flow. In the model the physical parameters of the compression system are used. The two new parameters, $\mathcal{C}'$ and τ, are difficult to determine in the compressor. It is found that for the current compressor both parameters reduce to one parameter $\mathcal{C}'/\tau \approx 0.1$ [s^{-1}]. This parameter represents the correction that is needed to account for the transient performance of the compressor and is independent of the system in which the compressor operates. The value of this parameter is for the simulations one order of magnitude smaller than if it is derived analytically. This difference is not surprisingly since it can be brought about by the assumptions that are made for the boundary-layer thickness, the fluid viscosity and the relaxation time.

Application of the improved model on the experimental compression system revealed a surge frequency and a maximum pressure rise that agree with measurement. Additionally, the measured constant pressure rise during decreasing mass flow is captured.

7.2 Recommendations

This study contributes to the understanding of flow instabilities that can occur in a compression system. It focusses on the unsteady character of compressor flow. The dynamics of the compression system instability are captured reasonably by a lumped parameter approach of the entire system. Therefore, the influence of unsteady flow on the compressor performance is incorporated in this model.

In this study, cubic polynomials are used to describe the steady compressor performance. The coefficients are determined from measurements. Especially in the unstable region this performance is hard to determine, since no measurement data is available. Therefore, it seems worthwhile to investigate the possibility to determine the compressor characteristic from energy considerations and compressor geometry as proposed by *Gravdahl and Egeland [29]*.

The verification of the simulated surge cycles is mainly based on the measured surge frequency and measured maximum pressure rise. In addition, the relation between the mass flow and pressure rise is of interest in the understanding of compressor surge. Therefore, this relation should be verified as well. Although, pressure measurements can be performed quite easily in the compressor, measurement techniques to obtain unsteady mass flow measurements are less easy. In this study a single hot-wire probe was positioned in the inlet of the compressor. It is found that during surge the hot-wire probe measurements only give a measure for the mass flow if there exists a forward flow and an increasing pressure in the compressor. A promising technique to accurately measure the unsteady flow in the compressor during surge is Digital Particle Imaging Velocimetry (DPIV), *Wernet et al. [69]*. This measurement technique captures the velocity vectors in a plane obtained by a pulsed laser light sheet that illuminates a flow field seeded with tracer particles small enough to follow the flow.

Parameters that appear are $\mathcal{C}'$ and τ, which are physical parameters that depend on the relevant boundary-layer thickness. In the compressor it is difficult to determine this thickness. Nevertheless, the parameters are expected to depend on the flow type and therefore, for various centrifugal compressors expected to be of the same order of magnitude. A study of these parameters for different compressors is necessary to validate this assumption.

The correction term depends on the time scale of a transient. Since, surge is commonly encountered during speed transients and set point changes, the correction term will influence the stability of the system. That is, the stability of the system will depend on the time scale of the set point change. In the framework of the companion project: *Compressor surge control*, *Willems [70]*, it is of interest to investigate the initiation of surge with the new developed model. If the initiation of surge is captured correctly in a simulation, surge controllers can be designed to control the surge before the disturbances in the system grow into undesired large pressure oscillations that can lead to severe damage of the compressor.

Throughout this study the development or existence of rotating stall cells is not taken into ac-

count. These two-or three-dimensional distortions of the flow through the compressor can be part of the flow instability surge. Experiments on the compression system showed that for low rotational speeds the development of a fully-developed surge is most possibly preceded by rotating stall. To be able to predict rotating stall and its influence on the axial as well as the circumferential flow of the compressor a two-dimensional model of the compressor flow is required. A model developed for this purpose is the Moore-Greitzer model *[53]*. The suggested correction on a quasi-steady compressor performance could be incorporated in this model to obtain better results for the surge dynamics in that model. The influence on the rotating stall and the necessity for a correction on the rotating stall flow could then be studied.

Bibliography

[1] G.L. Arnulfi, P. Giannattasio, C. Giusto, A.F. Massardo, D. Micheli, and P. Pinamonti. Multistage centrifugal compressor surge analysis: Part I - experimental investigation. *ASME paper*, (98-GT-68), 1998.

[2] G.L. Arnulfi, P. Giannattasio, C. Giusto, A.F. Massardo, D. Micheli, and P. Pinamonti. Multistage centrifugal compressor surge analysis: Part II - numerical simulation and dynamic control parameters evaluation. *ASME paper*, (98-GT-69), 1998.

[3] K. Bammert and A. Mobarak. in discussion of E.M. Greitzer, Surge and rotating stall in axial flow compressors, Part II: Experimental results and comparison with theory. *Transactions of the ASME, Journal of Engineering for Power*, 98(2):213–215, April 1976.

[4] R.J.M. Bastiaans. Cross-correlation PIV: Theory, implementation and accuracy. Report 99-W-001, Eindhoven University of Technology, 1999. ISBN 90-386-2851-x.

[5] K.K. Botros. Transient phenomena in compressor stations during surge. *Transactions of the ASME, Journal of Engineering for Gas Turbines and Power*, 116:133–142, January 1994.

[6] T. Breuer and S. Servaty. Stall inception and surge in high-speed axial flow compressors. In *Loss Mechanisms and Unsteady Flows in Turbomachines*. Agard PEP 85th Symposium, 8-12 May 1995.

[7] H.H. Bruun. *Hot Wire Anemometry: principles and signal analysis*. Oxford University Press Inc., New York, 1995.

[8] M.P. Buse, F.M. de Jongh, and F.H. Vial. Performance improvement of low volume flow centrifugal compressor stages. In *Proceedings of the 6th European Congress on Fluid Machinery for Oil, Petrochemical and Related Industries*, number C508/033/96, pages 155–167, The Hague, The Netherlands, June 1996. IMechE.

[9] A.M. Cargill and C. Freeman. High-speed compressors surge with application to active control. *Transactions of the ASME, Journal of Turbomachinery*, 113:303–311, 1991.

[10] M.V. Casey. The effect of Reynolds number on the efficiency of een centrifugal compressor stage. *Transactions of the ASME, Journal of Engineering for Gas Turbines and Power*, 107:541–548, 1985.

[11] H. Cohen, G.F.C. Rogers, and H.I.H. Saravanamuttoo. *Gas Turbine Theory*. Longman Scientific & Technical, fourth edition, 1996.

[12] W.W. Copenhaver and T.H Okiishi. Rotating stall performance and recoverability of a high-speed 10-stage axial flow compressor. *Transactions of the ASME, Journal of Propulsion and Power*, 9(2):281–292, March-April 1993.

[13] N.A. Cumpsty. *Compressor Aerodynamics*. Longman Scientific & Technical, 1989.

[14] R. D'Andrea, R.L. Behnken, and R.M. Murray. Active control of rotating stall using pulsed air injection: Experimental results on a low speed, axial flow compressor. In *SPIE Int'l. Symp. on Aerospace/defence sensing & control and dual-use Photonics*, April 1995.

[15] I.J. Day. Stall inception in axial flow compressors. *Transactions of the ASME, Journal of Turbomachinery*, 115:1–9, January 1993.

[16] I.J. Day. Axial compressor performance during surge. *Transactions of the ASME, Journal of Propulsion and Power*, 10(3):329–336, May-June 1994.

[17] I.J. Day. The fundamentals of stall and surge in axial compressors. In F.A.E. Breugelmans, editor, *Unsteady Flow in Turbomachines*, volume 1996-05 of *Lectures Series 1996-05*. VKI, 11-15 March 1996.

[18] R.C. Dean and L.R. Young. The time domain of centrifugal compressor and pump stability and surge. *Transactions of the ASME, Journal of Fluids Engineering*, 99:53–63, March 1977.

[19] H.W. Emmons, C.E. Pearson, and H.P. Grant. Compressor surge and stall propagation. *Transactions of the ASME*, 77(4):455–469, May 1955.

[20] H.A. van Essen. Design of a laboratory gas turbine installation. Technical Report WOC-WET 95.012, Stan Ackermans Institute, Eindhoven University of Technology, March 1995. ISBN 90-5282-452-5.

[21] H.A. van Essen. *Modelling and Model based control of turbomachinery*. PhD thesis, Eindhoven University of Technology, December 1998. ISBN 90-386-0830-6.

[22] A. Fatsis, , S. Pierret, and R. Van den Braembussche. Three-dimensional unsteady flow and forces in centrifugal impellers with circumferential distortion of the outlet static pressure. *Transactions of the ASME, Journal of Turbomachinery*, 119:94–102, January 1997.

[23] D.A. Fink, N.A. Cumpsty, and E.M. Greitzer. Surge dynamics in a free-spool centrifugal compressor system. *Transactions of the ASME, Journal of Turbomachinery*, 114:321–332, April 1992.

[24] C. Freeman, A. Wilson, I. Day, and M. Swinbanks. Experiments in active control of stall on an aeroengine gas turbine. *Transactions of the ASME, Journal of Turbomachinery*, 120(4):637–647, 1998.

[25] P. Frigne and R. Van den Braembussche. Distinction between different types of impeller and diffuser rotating stall in a centrifugal compressor with vaneless diffuser. *Transactions of the ASME, Journal of Engineering for Gas Turbines and Power*, 106:468–474, April 1984.

[26] A. Goto. Suppression of mixed-flow pump instability and surge by the active alteration of impeller secondary flow. *Transactions of the ASME, Journal of Turbomachinery*, 116(4):621–628, 1994.

[27] J.T. Gravdahl and O. Egeland. A Moore-Greitzer axial compressor model with spool dynamics. In *Proceedings of the 36th IEEE Conference on Decision and Control*, pages 4714–4719, San Diego, CA, 1997.

[28] J.T. Gravdahl and O. Egeland. Speed and surge control for a low order centrifugal compressor model. In *Proceedings of the 1997 International Conference on Control Applications*, pages 344–349, Hartford, CT, 1997.

[29] J.T. Gravdahl and O. Egeland. Centrifugal compressor surge and speed control. *IEEE Control Systems Technology*, 7(5):567–579, 1999.

[30] J.T. Gravdahl, F. Willems, B. de Jager, and O. Egeland. Modeling for surge control of centrifugal compressors: Experimental validation. *submitted*.

[31] E.M. Greitzer. Surge and rotating stall in axial flow compressors, Part I: Theoretical compression system model. *Transactions of the ASME, Journal of Engineering for Power*, 98(2):190–198, April 1976.

[32] E.M. Greitzer. Surge and rotating stall in axial flow compressors, Part II: Experimental results and comparison with theory. *Transactions of the ASME, Journal of Engineering for Power*, 98(2):199–217, April 1976.

[33] E.M. Greitzer. The stability of pumping systems-the 1980 Freeman scholar lecture. *Transactions of the ASME, Journal of Fluids Engineering*, 103(2):193–242, June 1981.

[34] K.E. Hansen, P. Jørgensen, and P.S. Larsen. Experimental and theoretical study of surge in a small centrifugal compressor. *Transactions of the ASME, Journal of Fluids Engineering*, 103(3):391–395, September 1981.

[35] H. Harada. Study of a surge-free centrifugal compressor with automatically variable inlet and diffuser vanes. In *International Gas Turbine and Aeroengine Congress & Exhibition*, number 96-GT-153, Birmingham, UK, June 1996. ASME.

[36] U. Haupt, U. Seidel, A.N. Abdel-Hamid, and M. Rautenberg. Unsteady flow in a centrifugal compressor with different types of vaned diffusers. *Transactions of the ASME, Journal of Turbomachinery*, 110:293–302, July 1988.

[37] G.J. Hendricks, J.S. Sabnis, and M.R. Feulner. Analysis of instability inception in high-speed multistage axial-flow compressors. *Transactions of the ASME, Journal of Turbomachinery*, 119:714–722, October 1997.

[38] G.V. Hobson, A.J.H. Williams, and H.J.G. Rickel. Laser-doppler velocimetry measurements in a cascade of compressor blades at stall. *Transactions of the ASME, Journal of Turbomachinery*, 120(1):170–179, 1998. ASME paper (96-GT-484).

[39] D.A. Hoying. Stall inception in a multistage high-speed axial compressor. *Transactions of the ASME, Journal of Propulsion and Power*, 11(5):915–922, September-October 1995.

[40] R. Hunziker and G. Gyarmathy. The operational stability of a centrifugal compressor and its dependence on the characteristics of subcomponents. *Transactions of the ASME, Journal of Turbomachinery*, 116:251–259, April 1994.

[41] B. de Jager. Rotating stall and surge control: a survey. In *34th IEEE Conference on Decision and Control*, volume 2, pages 1857–1862, New Orleans, LA, December 1995.

[42] D. Jin, H. Hasemann, U. Haupt, and M. Rautenberg. The flow rotation characteristics of a centrifugal compressor during surge. *ASME Paper*, (94-GT-154), 1994.

[43] N. Kämmer and M. Rautenberg. A distinction between different types of stall in a centrifugal compressor stage. *Transactions of the ASME, Journal of Engineering for Gas Turbines and Power*, 108:83–92, January 1986.

[44] S.G. Koff and E.M. Greitzer. Axisymmetrically stalled flow performance for multistage axial compressors. *Transactions of the ASME, Journal of Turbomachinery*, 108:216–223, October 1986.

[45] P.B Lawless and S. Fleeter. Rotating stall acoustic signature in a low-speed centrifugal compressor: Part 1– vaneless diffuser. *Transactions of the ASME, Journal of Turbomachinery*, 117:87–96, January 1995.

[46] S. Lieblein. Loss and stall analysis of compressor cascades. *Transaction of the ASME, Journal of Basic Engineering*, pages 387–400, September 1959.

[47] W.J.P.M. Maas. Metingen in de inlaat van een centrifugaal compressor ten behoeve van surge-onderzoek. Technical Report WET 98.028, Eindhoven University of Technology, Faculty of Mechanical Engineering, Section Energy Technology, 1998.

[48] A.F. Massardo, F. Ghiglino, and L. Bolognese. Dynamic simulation of axial multistage compressors utilizing experimental or theoretical stage performances curves. In *2rd European Conference on Turbomachinery - Fluid Dynamics and Thermodynamics*, pages 153–161, Antwerpen, Belgium, March 1997. ImechE.

[49] C. Meuleman. Surge dynamics in a centrifugal compressor system at Stork Hengelo. Technical Report WET 98.031, Eindhoven University of Technology, Mechanical Engineering, 1998.

[50] C. Meuleman. Compressor flow instabilities. Report WET 99.020, Eindhoven University of Technology, Faculty of Mechanical Engineering, Section Energy Technology, August 1999.

[51] C. Meuleman, R. de Lange, and A. van Steenhoven. Surge dynamics in a centrifugal compressor system. In *3rd European Conference on Turbomachinery - Fluid Dynamics and Thermodynamics*, pages 895–904, London, UK, 3-5 March 1999. ImechE.

[52] C. Meuleman, F. Willems, R. de Lange, and B. de Jager. Surge in a low-speed radial compressor. *ASME Turbo Expo '98*, (98-GT-426), June 1998.

[53] F.K. Moore and E.M. Greitzer. A theory of post-stall transients in axial compression systems: Part I - development of equations. *Transactions of the ASME, Journal of Engineering for Gas Turbines and Power*, 106:68–76, January 1986.

[54] Y. Nishihara. Surging behaviour of gas turbines. *JSME International Journal*, 36(3):567–576, 1993.

[55] R. Ovink. *Flamelet Modelling for Partially Premixed Turbulent Jet Diffusion Flames*. PhD thesis, Eindhoven University of Technology, December 1999. ISBN 90-386-2761-0.

[56] R.C. Pampreen. *Compressor surge and stall*. Concepts ETI, Inc, first edition, 1993.

[57] J.E. Pinsley, G.R. Guenette, A.H. Epstein, and E.M. Greitzer. Active stabilization of centrifugal compressor surge. *Transactions of the ASME, Journal of Turbomachinery*, 113(4):723–732, October 1991.

[58] C.A. Poensgen and H.E. Gallus. Rotating stall in a single-stage axial compressor. *Transactions of the ASME, Journal of Turbomachinery*, 118:189–196, April 1996.

[59] M. Pouagare, J.M. Galmes, and B. Lakshminarayana. An experimental study of the compressor rotor blade boundary layer. *Transactions of the ASME, Journal of Engineering for Gas Turbines and Power*, 107:364–373, April 1985.

[60] M. Raffel, C. Willert, and J. Kompenhans. *Particle Image Velocimetry; a Practical Guide*. Berlin: Springer, 1998. ISBN 3-540-63683-8.

[61] B. Ribi and G. Gyarmathy. Impeller rotating stall as a trigger for the transition from mild to deep surge in a subsonic centrifugal compressor. *ASME Paper*, (93-GT-234), 1993.

[62] B. Ribi and G. Gyarmathy. The behaviour of a centrifugal compressor stage during mild surge. *VDI Berichte*, (1186), 1995.

[63] W. Rieß and M. Walbaum. Initiation and propagation of flow instabilities in multi-stage axial compressors. In *Loss Mechanisms and Unsteady Flows in Turbomachines*. Agard PEP 85th Symposium, 8-12 May 1995.

[64] H. Schlichting. *Grenzschicht-Theorie*. G. Braun, Karlsruhe, third edition, 1958.

[65] H. Schlichting and K. Gersten. *Boundary-Layer Theory*. Berlin: Springer, 8th rev. and enlarged edition, 2000. ISBN 3-540-66270-7.

[66] K. Toyama, P.W. Rundstadler, Jr., and R.C. Dean, Jr. An experimental study of surge in centrifugal compressors. *Transactions of the ASME, Journal of Fluids Engineering*, pages 115–131, March 1977.

[67] M. Tryfonidis, O. Etchevers, J.D. Paduano, A.H. Epstein, and G.J. Hendricks. Prestall behavior of several high-speed compressors. *Transactions of the ASME, Journal of Turbomachinery*, 117:62–80, January 1995.

[68] H.O. Wang, R.A. Adomaitis, and E.H. Abed. Nonlinear analysis and control of rotating stall in axial flow compressors. In *Proceedings of the American control conference*, number TP13-5:20, Baltimore, Maryland, 1994.

[69] M.P. Wernet, M.M. Bright, and G.J. Skoch. An investigation of surge in a high-speed centrifugal compressor using digital PIV. *Transactions of the ASME, Journal of Turbomachinery*, 123:418–428, April 2001.

[70] F. Willems. *Modeling and Bounded Feedback Stabilization of Centrifugal Compressor Surge*. PhD thesis, Eindhoven University of Technology, June 2000. ISBN 90-386-2931-1.

[71] J. Ffowcs Williams and X. Huang. Active stabilization of compressor surge. *Journal of fluid Mechanics*, (204):245–262, 1989.

[72] A. Witfield and N.C. Baines. *Design of Radial Turbomachines*. Longman Scientific & Technical, 1990. ISBN 0-582-49501-6.

Appendix A

Aerodynamic scaling

To assess the aerodynamic properties of the compressor flow an appropriate scaling is applied. The resulting aerodynamic scaling gives, e.g., a measure for the blade loading or the incidence of the flow on the blades. The aerodynamic scaling can be found in *Cumpsty [13]*.

Pressure rise coefficient (ψ)

The enthalpy rise of a stage is related to the square of the rotational speed, $\Delta h/U^2$, where U can either be the blade tip speed or the speed at midradius, the latter being quite common for axial compressors. The tip speed in radial machines is defined as:

$$U_t = \pi d_2 \frac{N}{60} \; .$$

Herein, is d_2 the impeller outlet diameter and N the angular velocity of the shaft, also referred to as rotational speed in [rpm]. For compressors in which the pressure rise (Δp) is small compared to the absolute pressure the density may be reasonably approximated as constant. The pressure rise coefficient is then defined as:

$$\psi = \frac{\Delta p}{\frac{1}{2}\rho U^2} \; , \tag{A.1}$$

where $1/2$ is sometimes omitted and ρ is the inlet density of the compressor. The denominator gives a measure for the dynamic pressure imparted by the blades.

Flow coefficient (ϕ)

The work input to a stage depends on the flow through it. For an axial compressor the flow coefficient is defined as:

$$\phi = \frac{V_x}{U_t} \; , \tag{A.2}$$

which is the ratio of the axial velocity (V_x) to the blade speed (U_t). The flow coefficient determines the incidence into the rotor, and therefore effectively determines the performance. For radial compressors a somewhat other expression for the mass flow coefficient is used:

$$\phi = \frac{\dot{m}}{\rho A U} \; . \tag{A.3}$$

This gives a measure for the ratio of impeller inlet velocity to the blade speed. Here ρ is the inlet density and A is the inlet area of the impeller.

Reynolds number (Re)

The choice of the appropriate Reynolds number in a centrifugal compressor depends on the choice of the most relevant length scale. The most serious viscous loss source is believed to be at or near the impeller outlet, largely because the passage is narrowest here, *Casey [10]*. An appropriate choice therefore is:

$$Re_b = \frac{U_t \, b}{\nu} \; , \tag{A.4}$$

where U_t is the impeller tip speed, b is the exit impeller tip width and ν the inlet viscosity. In axial compressors the Reynolds number is based on the chord length of the blades, c, (e.g., *[46]* and *[38]*):

$$Re_c = \frac{U \, c}{\nu} \; . $$

Mach number (M)

The Mach number is determined from:

$$M = \frac{U}{a} \; . \tag{A.5}$$

This gives a measure for the ratio of the blade speed and the speed of sound, which for a calorically perfect gas is:

$$a = \sqrt{\gamma R T} \; . \tag{A.6}$$

Herein, is R the gas constant, T the temperature, and γ is the ratio of specific heats (c_p/c_v). The Mach number is used to give an indication of the compressibility of the compressor flow.

Appendix B

Rotating stall

Rotating stall consists of zones of stalled passages covering a small number of blades. The stalled flow rotates at some fraction of the rotor speed in the absolute direction of rotor rotation. It occurs in rotating and stationary blade rows and in both axial and centrifugal compressors. The rotation of the stall cells can be explained by viewing the blade row from the top in a linear cascade setting, see Figure B.1. Due to the region of stalled flow the flow is locally deflected to the front and to the back side of the stalled region. This results in an increase of the incidence angle at the rearward blade and a decrease of the incidence angle at the forward blade. The effect is such that the unstalled rearward blade will become stalled while the stalled forward blade recovers. In this way a relative motion of the stalled region is induced. The propagation of the stall cell is opposite to the rotor rotation in the relative frame of reference. As observed in the absolute frame, the cell appears to move in the direction of the rotor rotation but at a much reduced speed. Depending on the size of the stall cell(s) the rotational stall speed is between 20 and 80% of the rotor speed: larger cells rotate at a lower rotational speed than the smaller cells, *Greitzer [33]*.

Direction of Stall Cell
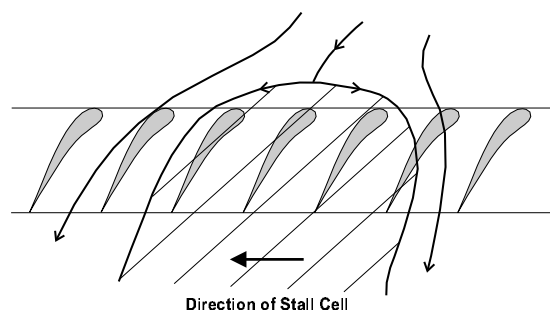
Figure B.1: Rotating stall in the relative frame of reference.

Once the compressor experiences rotating stall, the working point of the compressor moves to the so-called stall characteristic. This can happen in a *progressive stall* way, in which the pressure decreases gradually as the mass flow decreases, or in an *abrupt stall* way in which the pressure drops abrupt at a certain mass flow. These two stall phenomena are shown in Figure B.2 in a compressor characteristic. The drop of the pressure rise depends on the amount of disturbed flow in the compressor. In the case of *part-span stall* the stall cell is formed only close to the tip

(a) progressive stall   (b) abrupt stall
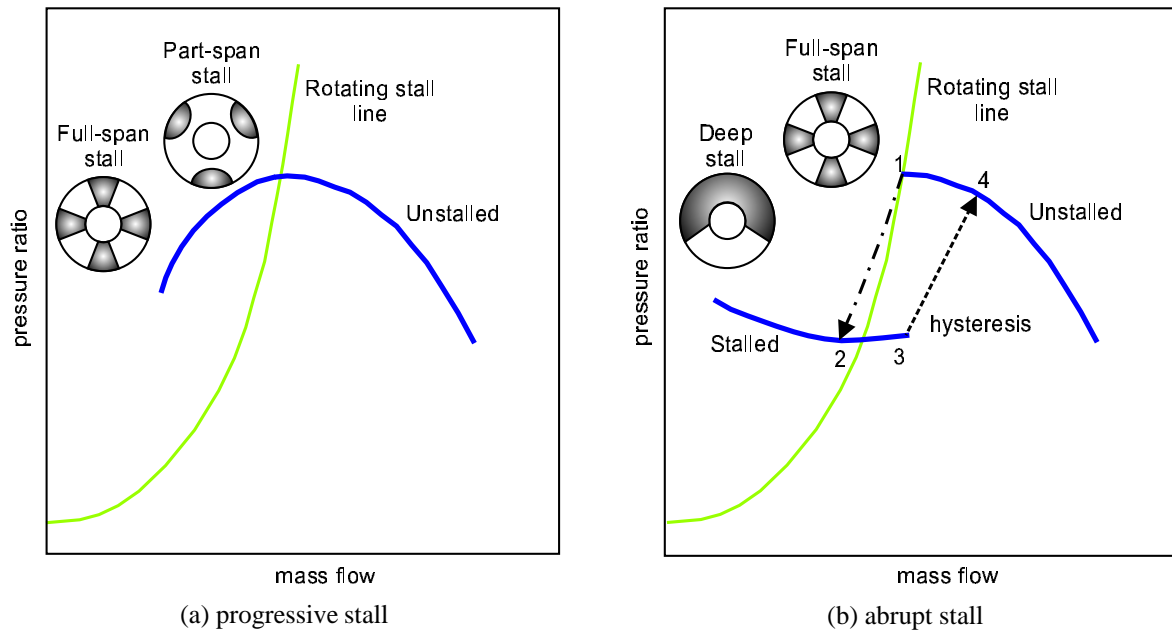
Figure B.2: Stall characteristic.

for a rotor and close to the hub for a stator. In the case of *full-span stall* the stall cell is stretched from hub to tip and the drop of pressure rise is larger than for part-span stall, *Day [17]*. The full-span stall can be progressive or abrupt. Stall usually starts with multiple cells. Then, as flow is reduced the number of cells may increase. As the flow is further reduced, the number may diminish until only a few cells are present and a *deep stall* is obtained, *Pampreen [56]*. In the case of rotating stall, reduction of the flow results in a stable operating compressor, since its operational point is positioned on the stalled characteristic. Typical for abrupt stall is the hysteresis that exists as flow is increased to unstalled conditions of the compressor. Then the flow rate is higher than the flow rate at which stall was first encountered during flow reduction, *[12]*.

Note, that the rotating stall line indicates the relation between the mass flow and pressure rise for which compressor starts to experience stall. It depends on the system in which the compressor operates whether the surge or rotating stall limit occurs. A discussion on this subject can be found in this thesis in Section 2.4 and is explained with Figure 2.8.

In literature, two mechanisms for the inception of rotating stall cells can be found. Both originate from the paper of *Emmons et al.* [19] and are discussed by *Day* [15]. The first flow mechanism results in a disturbance of a *short length scale*. In a row of highly loaded blades, a minor physical irregularity, or flow uniformity, can result in momentary overloading and flow separation. This separation will restrict the flow through the passage and will therefore divert the incoming streamlines, resulting in the rotating stall shown in Figure B.3(a). A cell that is initiated in this way only affects the flow around just a few blade passages. The second flow mechanism is based on *modal perturbation*, which may be visualised as small sinusoidal velocity fluctuations that rotate around the annulus at a steady speed, as shown in Figure B.3(b). A velocity perturbation with a wavelength equal to the circumferential length of the annulus would be referred to as a mode of order 1. The blades in Figure B.3(b) are moving to the

right and so does the perturbation, but always at a speed lower than the blade speed. When the flow is throttled toward the stall point the stability of the compressor gradually decreases. This means that the perturbation slowly grows in intensity, without abrupt change in frequency and amplitude, until a fully developed stall cell is formed. Initially, the wave amplitude would be infinitely small and not discernible above the background noise, but as the instability point is approached growth of the wave would be rapid. To the observer the compressor would appear to stall instantaneously.
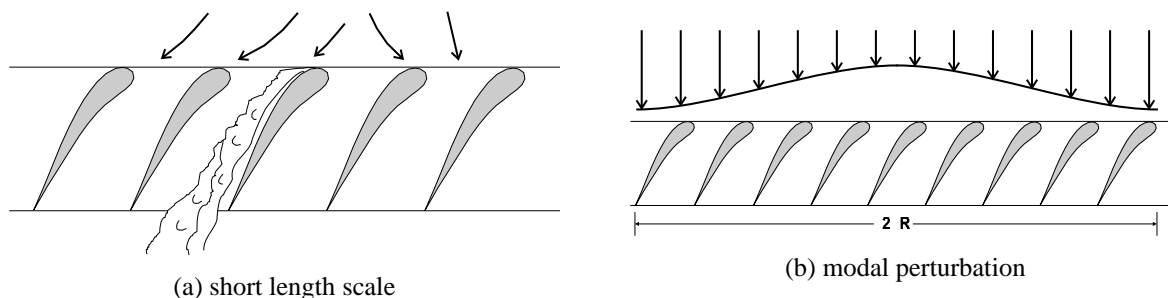

(a) short length scale

(b) modal perturbation

Figure B.3: Stall cell inception.

In the paper (*[15]*), Day makes a clear distinction between a stall cell and a modal wave. A modal wave is a 'reversible' disturbance, which can be made to come and go by slight changes in the throttle setting and may be visible in the machine for as much as 200 rotor revolutions before stall. During this time the pressure rise across the compressor will remain nearly constant. A stall cell, on the other hand, is a comparatively 'irreversible' disturbance and once formed will lead to a collapse of the pressure rise, usually within four to six rotor revolutions.

In Table B.1 the inception mechanisms found in literature are given. As can be seen, both stall inception mechanisms are detected and can even exist in the same compressor configuration. For example, *Breuer and Servaty [6]* studied stall inception in a high-speed axial flow compressor. They found that stage matching influences the type of disturbance occurring. At 60 percent of the design speed the instability started as a short length scale disturbance at the front stage. At speeds of 80 to 90 percent of the design speed the instability emerges from a modal disturbance. Then, at design speed the disturbance starts as a short length scale disturbance at the last stage. All articles show the possibility to detect either a modal wave disturbance or a short length

Table B.1: Initiation of stall in (multi-) axial compressors.

	short length scale	modal perturbation
Day et al. [15]	x	-
Rieß and Walbaum [63]	x	-
Breuer and Servaty [6]	x	x
Hoying [39]	x	x
Poensgen and Gallus [58]	-	x
Tryfonidis et al.[67]	-	x

scale disturbance before well-developed (length and rotational speed is settled) rotating stall is obtained. Unfortunately, the cause of the disturbance is still not clear. Especially, the cause of

the initiation of a modal wave disturbance is not understood. The short scale disturbance could be caused by some disturbance in the flow. Think of inlet distortion and mismatching of the flow from one stage to the next one.

Experimental evidence of the initiation of stall in centrifugal compressor is less extensive than in axial compressors, *[56]*. Mostly, the studies are concentrated on the interaction between the impeller, the vaneless diffuser, and the vaned diffuser, see e.g., *[25]*, *[43]*, *[36]*, *[45]*, *[8]*.

Appendix C

Lumped parameter modelling

A compression system model developed by *Greitzer [31]* is discussed below. The oscillations in the system are modelled in a manner analogous to those in a Helmholtz resonator. The assumptions of a Helmholtz resonator imply that all the kinetic energy of the oscillations is associated with the motion of the fluid in the compressor and ducts. The potential energy of the fluid is associated with the compression of the gas in the plenum. Furthermore, the assumptions are that the inlet Mach numbers are low and that the pressure rises are small compared to the ambient pressure. The fluid dynamic model that is used in the analysis is shown in Figure C.1.
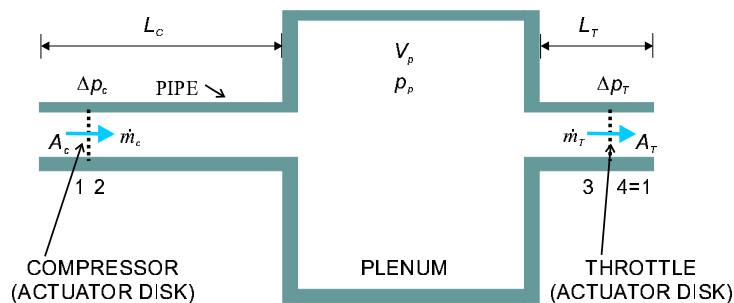
Figure C.1: Equivalent compression system used in analysis. *[Greitzer [31]]*

The compressor and its ducting are replaced by an actuator disk, to account for the pressure rise due to the compressor, and a length of a constant area pipe to account for the dynamics of the fluid in the compressor duct. Similarly, the throttle is replaced by an actuator disk, across which the pressure drops, plus a constant area duct. The actuator disk theory assumes that a blade row can be represented by a disk with an infinitesimal thickness across which the mass flow is continuous, but pressure changes can be discontinuous. The flow in the ducts can be considered incompressible, since the inlet Mach number is assumed to be low, the pressure rise is small and the frequency of the oscillations associated with surge are regarded to be low. As a consequence, the mass flow at the inlet of the duct is equal to the mass flow at the outlet of duct.

The rate of change of the mass flow in the compressor duct, represented by the axial velocity, C_{x_c}, is related to the pressure difference across the duct, $\Delta p = p_p - p_0$, and the pressure rise

across the compressor, $\Delta p_c = p_c - p_0$,

$$\rho \, L_c \, \frac{dC_{x_c}}{dt} = (p_0 - p_p) + \Delta p_c. \tag{C.1}$$

An analogous equation is written to describe the flow in the throttle duct:

$$\rho \, L_T \, \frac{dC_{x_T}}{dt} = (p_p - p_0) - \Delta p_T \,, \tag{C.2}$$

in which $\Delta p_T = p_T - p_0$ is the pressure rise across the throttle. Equations (C.1) and (C.2) are essentially the first integrals of the one-dimensional momentum equation. Since the flow in the ducts is assumed incompressible the equations can be written as:

$$\frac{L_c}{A_c} \, \frac{d\dot{m}_c}{dt} = -\Delta p + \Delta p_c \,, \tag{C.3}$$

$$\frac{L_T}{A_T} \, \frac{d\dot{m}_T}{dt} = \Delta p - \Delta p_T \,. \tag{C.4}$$

The geometry of the equivalent ducts, L_c and L_T, is determined by requiring that a given rate of change of mass flow produces the same unsteady pressure difference in the actual duct as in the model, and by matching the area of the model duct with a characteristic area of the actual duct. In the compressor this can be the inlet area, and in the throttle the throughflow area in the discharge plane. This requirement leads to the relation:

$$\frac{L}{A} = \int_{actual \; ducting} \frac{ds}{A(s)} \,. \tag{C.5}$$

The integration is assumed to be carried out over all regions of the actual ducting in which the flow has significant kinetic energy. Note, that in both ducts the equation of continuity has entered implicitly in the definition of the form of the equivalent duct lengths.

In the plenum the fluid velocities are negligible. Furthermore, plenum dimensions are typically very much smaller than the wavelength of an acoustic wave having a frequency on the order of that associated with surge. Hence, the static pressure will be uniform throughout the plenum at any instance of time. During the flow transient, the mass flow through the compressor and the throttle may have different values, therefore, the continuity equation is applied to the plenum:

$$\dot{m}_c - \dot{m}_T = V_p \, \frac{d\rho_p}{dt} \,.$$

If the thermodynamic process in the plenum is isentropic, then the density change will be related to the changes in plenum pressure, which for a calorically perfect gas is:

$$p(\frac{1}{\rho})^\gamma = constant \,,$$

$$\frac{d\rho_p}{dt} = \frac{\rho_p}{\gamma p_p} \, \frac{dp_p}{dt} \,,$$

in which γ is the ratio of specific heats. In addition, Greitzer assumed that the overall pressure and temperature ratios of the compression system, *i.e.*, plenum to atmosphere, are near unity. Consequently, the quantity $\frac{\rho_p}{p_p}$ in the plenum is not significant different from $\frac{\rho}{p}$ in ambient. With use of the speed of sound, a, corresponding to ambient conditions:

$$\frac{\gamma \, p}{\rho} \;=\; a^2 \,,$$

the expression for mass conservation in the plenum becomes:

$$\dot{m}_c - \dot{m}_T = \frac{V_p}{a^2} \frac{dp_p}{dt} \;. \tag{C.6}$$

In centrifugal compressors the pressure and temperature ratios of the compression system are often larger than unity. Therefore, *Fink et al. [23]* used the speed of sound based on the plenum condition instead of the ambient condition at the steady-state operating point.

Equation (C.3), (C.4), and (C.6) are the equations for a lumped parameter approach of the dynamics of a compression system. The equations are referred to as a lumped parameter approach, since different fluid properties are lumped to a certain aspect of the compression system. The inertia of the system is lumped to a duct, the compressibility to a volume and the pressure rise to an actuator disk. The modelling of the compression system with a lumped parameter approach is widely accepted in literature, and is useful in the stabilisation of rotating stall and surge by means of active control.

Equation (C.3), (C.4), and (C.6) form the mathematical equations of the dynamics of the system, in which the pressure rise of the compressor and throttle valve, Δp_c and Δp_T, respectively, are known parameters of the system. These equations can be nondimensionalised according to the aerodynamic scaling discussed in Appendix A:

$$\frac{d\phi_c}{d\tilde{t}} \;=\; \frac{U}{2\omega_H L_c} \left(\psi_c - \psi \right) , \tag{C.7}$$

$$\frac{d\phi_T}{d\tilde{t}} \;=\; \frac{U}{2\omega_H L_c} \frac{L_c A_T}{L_T A_c} \left(\psi - \psi_T \right) , \tag{C.8}$$

$$\frac{d\psi}{d\tilde{t}} \;=\; \frac{2 A_c a^2}{U V_p \omega_H} \left(\phi_c - \phi_T \right) . \tag{C.9}$$

The time is nondimensionalised by the Helmholtz frequency of the compressor duct-volume system in absence of the compressor and throttle, $\tilde{t} = t \, \omega_H$:

$$\omega_H = a \, \sqrt{\frac{A_c}{V_p \, L_c}}. \tag{C.10}$$

Two nondimensional parameters appear, that is:

$$B \;=\; \frac{U}{2\omega_H L_c} \,, \tag{C.11}$$

$$G \;=\; \frac{L_T A_c}{L_c A_T} \;. \tag{C.12}$$

The parameter B can be given the physical significance by writing it as (*Cumpsty [13]*):

$$B = \frac{\frac{\rho\, U^2}{2} A}{\rho A L U \omega_H} \ .$$

The numerator gives a measure of the pressure rise capability of the compressor multiplied by the duct area. The denominator contains the product $\rho A L$, which is the mass of the gas in the duct, the velocity U, and the frequency of natural oscillation ω_H. The axial velocity V_x for a given axial compressor will be approximately proportional to the blade speed U. The denominator is therefore approximately equal to that $\rho A L V_x \omega_H$, which is the force required to produce small oscillations of the flow in the duct at the natural frequency. The parameter B can therefore be viewed as the ratio of the compressor pressure rise capability to the pressure rise required to induce mass flow oscillations. If B is low it is equivalent to saying that the compressor does not have much pressure rise capability compared to what is required to begin a surge. Although aircraft engines can either surge or move into rotating stall, the clear trend is, as predicted by the B-parameter, that the engine is more likely to surge as the speed is increased, see *Meuleman [50]*. However, the importance of the B-parameter is not such that it allows one to predict whether an engine will surge or stall but that it has altered the way that surge and stall are thought about. The work of Greitzer was directed at axial compressors and the magnitude of the critical B was appropriate for this type of machine. Nevertheless, the underlying idea, that surge can only occur when the pressure rise capability of the compressor is large enough in relation to the pressure difference needed to oscillate the flow in the ducts at the natural frequency of the system, is quite general to all types of compressor.

The parameter G can be interpreted as the ratio between the inertia of the fluid flow across the throttle and the compressor. If the throttle length is small compared to the compressor length or if the area of the throttle is large compared to the area of the compressor, Equation (C.8) can be omitted and only Equation (C.7) and Equation (C.9) are solved.

C.1   System stability

For small G and by considering small perturbation around the time-mean values the remaining two equations, Equation (C.7) and Equation (C.9), can be rearranged such that a single second-order ordinary differential equation is obtained. For reference see *Cumpsty [13]*. Then a static and dynamic instability of the system can be identified based on the slopes of the compressor and throttle characteristic. The single second-order ordinary differential equation for ψ is:

$$\frac{d^2\psi}{d\tilde{t}^2} \ + \ \left\{ \frac{1}{B\,T} \ - \ C\,B \right\} \frac{d\psi}{d\tilde{t}} \ + \ \left\{ 1 - \frac{C}{T} \right\} \psi \ = \ 0 \ . \tag{C.13}$$

In which $C \ = \ d\psi_c/d\phi_c$ and $T \ = \ d\psi_T/d\phi_T$ are the slopes of the compressor and throttle characteristic, respectively. Equation (C.13) shows that the compressor-duct-plenum-throttle system has an analogy with a mass-spring-damper system.

Considering the undamped part of Equation (C.13) a *static stability* limit can be identified. The damping part of Equation (C.13) is expressed in the coefficient before the first derivative of ψ.

If this coefficient is negative it is equivalent to negative damping in the mass-spring-damper analogy, which is known as a *dynamic instability*. The instability conditions occur at:

$$\frac{C}{T} > 1, \qquad \text{static instability},$$

$$\frac{1}{B\,T} - C\,B < 0, \qquad \text{dynamic instability}. \tag{C.14}$$

From the definition of the static and dynamic instability it follows that the dynamic instability depends on the whole compression system, while static instability only depends on the throttle and compressor characteristic. For most systems, dynamic instability is obtained at a larger mass flow than static instability. This means that the surge measured in compression systems normally are due to the dynamic stability limit and therefore, depend on the configuration of the system. For example, a larger volume, duct area, or a smaller duct length result in a dynamic stability limit at larger mass flows.

However, since the compressor characteristic and the geometrical parameters of a system are difficult to determine accurately the stability limit of a system is very difficult to define by considering the instability conditions in Equation (C.14).

C.2   Quasi-steady compressor modelling

The first general method to determine the steady-state compressor characteristic is by measurement. *Fink et al. [23]* and *Arnulfi et al. [2]* showed that the forward flow characteristic can be measured up to very small mass flows if a very small volume (small B-parameter) is placed in the compression system. Then, the occurrence of surge can be postponed to low mass flows or can even be prevented. The negative mass flow branch of the characteristic curve is determined by fitting the negative flow decreasing portion of the measured deep surge cycles. This is allowed since for a large volume (large B-parameter) the decreasing portion of the deep surge cycle is determined by the emptying of the volume instead of the inertia of the ducting. Then, the plenum pressure is thought to be very close to the steady-state compressor delivery pressure. *Hansen et al. [34]* measured the negative branch of the steady-state characteristic by feeding shop-air to the compressor exit to force a negative flow. Furthermore, they did not use a small volume to determine the positive flow characteristic. Instead, they assumed that the curve between the steady measurable positive flow branch and the negative flow branch can be connected by a smooth curve.

The second general method to describe the steady-state compressor characteristic is by using the typically smooth S-shaped curve, shown in Figure C.2, which follows from a cubic polynomial:

$$\psi_c(\phi) = \psi_{c_0} + H \left\{ 1 + \frac{3}{2}(\frac{\phi}{W} - 1) - \frac{1}{2}(\frac{\phi}{W} - 1)^3 \right\}. \tag{C.15}$$

Herein, is ψ_{c_0} the valley point of the characteristic located at the compressor pressure rise axis, is $2W$ the flow coefficient corresponding to the top of the characteristic, and is $2H$ the pressure rise coefficient corresponding to the top minus the bottom pressure rise coefficient of the characteristic. The parameters ψ_{c_0}, H, and W are determined from steady-state measurements of

the compressor characteristic and from transient surge data. This representation of the steady-state compressor characteristic is used in axial compressors by, e.g., *Moore and Greitzer [53]*, *Wang et al. [68]*, *D'Andrea et al. [14]*, and *Gravdahl and Egeland [27]*. In centrifugal compressors it is used by, e.g., *Botros [5]* and *Meuleman et al. [52]*.
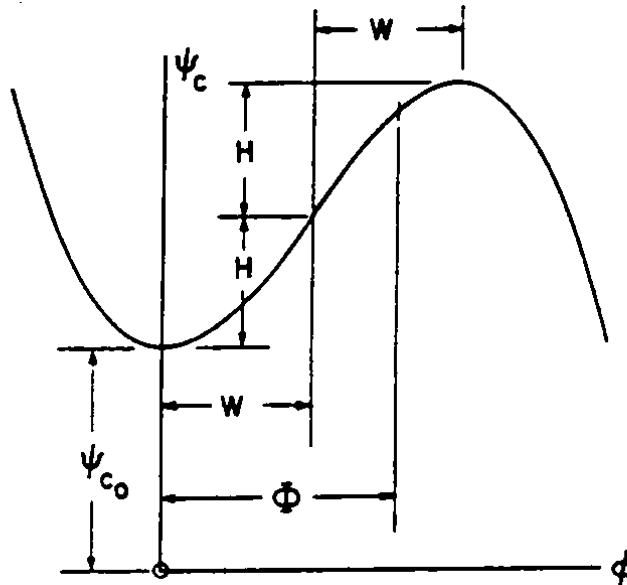

Figure C.2: Notation used in definition of cubic axisymmetric compressor characteristic. *[Moore and Greitzer [53]]*

A thermodynamic related prediction method to determine the quasi-steady centrifugal compressor characteristic is used by *Gravdahl and Egeland [28]*. Instead of modelling the compressor characteristic by describing the pressure to be a function of the mass flow and rotational speed, the compressor characteristic was modelled by an isentropic process consideration to which the losses are added. *Hendricks et al. [37]* determined the quasi-steady performance of an axial compressor from a computation of a mean line flow model.

Koff and Greitzer [44] suggested to identify the axisymmetric characteristic for an axial compressor in the low forward flow regime from transient measured compressor data. In this approach one 'subtracts off' that part of the pressure rise due to flow accelerations (or decelerations) during an axisymmetric compressor surge cycle. In Chapter 3 the quasi-steady centrifugal compressor characteristic is also derived from surge measurements. The conclusion is that the compressor performance during surge is far from being quasi-steady. So, no (axisymmetric) quasi-steady characteristic could be found.

C.3 Time lag in compressor response

Greitzer et al. [31] observed that the development of rotating stall cells took approximately seven rotor revolutions to grow to full growth. The time needed for development of the stall cell can be long enough so that the compressor mass flow undergoes a significant change during

this process. Under these conditions a quasi-steady approximation is not adequate. Therefore, a simple, first order transient response model to simulate this lag in compressor response was proposed.

The approximation for the transient compressor response is written as:

$$\tau \, \frac{d\Delta p_c}{dt} \;=\; \Delta p_{c_{ss}} \;-\; \Delta p_c \, , \tag{C.16}$$

with $\Delta p_{c_{ss}}$ denoting the steady-state measured compressor curve. The time constant τ is defined to be proportional to the time for some number, N, of rotor revolutions:

$$\tau \;=\; \frac{2\pi N R}{U} \, . \tag{C.17}$$

The nondimensional time constant, $\tilde{\tau} = \tau \omega_H$, is:

$$\tilde{\tau} \;=\; \frac{\pi N R}{L_c B} \, .$$

Greitzer found that N depends on the compressor considered. For his application $N = 2$ suited best. This first order delay of the compressor performance is used in axial compressors, e.g., by *Nishihara [54], Massardo et al. [48]*, and *Hendricks et al. [37]*. For centrifugal compressors it is used by, e.g., *Hansen et al. [34], Fink et al. [23], Botros [5]*, and *Arnulfi et al. [2]*.

As was observed by Greitzer the value for N depends on the compressor used. Hansen et al. found that $N = 0.5$ is of the order of the transport time through the impeller. A remark to this work is that they did not explicitly observe developing rotating stall cells during the surge cycle and used the first order time lag to fit the surge simulations to the measurements. Furthermore, Arnulfi et al. used $N = 4$. Remarkable is that the corresponding value of the time constant is imposed only when the compressor is operating in the stalled portion of the characteristic, namely, for a flow coefficient greater than zero and less than the stall limit value. On the contrary, when reverse flow occurs or the compressor is running on the unstalled branch of the characteristic, $\tilde{\tau}$ is set equal to a very small value that corresponds to the fast compressor response observed when rotating stall is absent.

Fink et al. used the time constant to model the lag period that is measured from the precursor of mild surge to deep surge. The time constant is based on the convection time through the impeller and vaneless diffuser. The compressor throughflow time is given approximately by:

$$\tau \;=\; \frac{L_t}{C_m} \, ,$$

in which L_t is the meridional throughflow length of the impeller and vaneless diffuser, and C_m is the meridional average flow velocity. The nondimensional throughflow time constant is:

$$\tilde{\tau} \;=\; \left(\frac{1}{2} \frac{L_t}{L_c} \right) \frac{1}{B|\phi_c|} \, .$$

Physically, this time lag has the effect of flattening the instantaneous compressor characteristic relative to the quasi-steady curve, which leads to a slower growing instability.

C.4   Model parameters

The parameters in the lumped parameter model are difficult to determine straight forward. This is shown by presenting here the model parameters as used by *Willems [70]* for the same compression system as discussed in Chapter 2 and 3.

The lumped parameter Equations (C.7), (C.8), and (C.9) are used with an additional assumption that the G-parameter is small. This means that the throttle duct length is assumed to be much smaller than the compressor duct length. A two state lumped parameter model is obtained according to:

$$\frac{d\phi_c}{d\tilde{t}} = B\left(\psi_c - \psi\right), \tag{C.18}$$

$$\frac{d\psi}{d\tilde{t}} = \frac{1}{B}\left(\phi_c - \phi_T\right), \tag{C.19}$$

$$\psi_T = \psi. \tag{C.20}$$

To be able to solve the set of equations a relation for the steady-state compressor and throttle valve pressure rise, ψ_c and ψ_T, respectively, and the geometrical parameters are determined. The steady-state throttle valve characteristic is determined as:

$$\psi_T = \left(\frac{\phi_T}{c_T Y_T}\right)^2, \qquad \text{with} \qquad c_T = 0.332.$$

The steady-state compressor pressure rise, ψ_c, is a function of the compressor flow, ϕ_c, and the rotational speed, N. The compressor characteristic is approximated by a cubic polynomial in ϕ_c as discussed in C.2. To obtain a best fit of all steady-state measurements the cubic polynomial is rewritten to:

$$\psi_c(\phi_c) = c_0(N) + c_1(N)\phi_c^2 + c_2(N)\phi_c^3,$$

with

$$c_0(N) = \psi_c(0), \quad c_1(N) = \frac{3H}{2W^2}, \text{ and } \quad c_2(N) = \frac{-H}{2W^3}.$$

For each rotational speed line in the compressor characteristic the parameters $c_0(N)$, $c_1(N)$, and $c_2(N)$ are determined. The dependence of these parameters on rotational speed N is approximated by a quadratic polynomial in N:

$$c_0(N) = -7.3130 \cdot 10^{-9} N^2 + 2.5979 \cdot 10^{-4} N - 1.0588,$$
$$c_1(N) = 7.9639 \cdot 10^{-7} N^2 - 2.504 \cdot 10^{-2} N + 2.234574 \cdot 10^2,$$
$$c_2(N) = -3.1774 \cdot 10^{-6} N^2 + 9.750 \cdot 10^{-2} N - 9.009138 \cdot 10^2.$$

As in Section 3.3 the estimated compressor pressure rise at zero flow is improved by changing the valley point of the cubic polynomial with Δ_{c0}. The resulting approximated compressor characteristic is determined with the parameters W and H, and $\psi_c(0)$ that depend on ϕ_c:

$$\phi_c \geq 2W, \quad H' = H \quad \text{and} \quad \psi_c'(0) = \psi_c(0),$$

$$\phi_c < 2W, \quad H' = H + \frac{1}{2}\Delta_{c0} \quad \text{and} \quad \psi_c'(0) = \psi_c(0) - \Delta_{c0} \ .$$

The values of the geometric parameters of the compression system as indicated in Figure 3.1 are shown in Table C.1 for the problem discussed by Willems as well as for the problem discussed in this thesis (Chapter 3). Both definitions obtain a surge frequency which is within the range it

Table C.1: Compression system parameters according to Willems and this thesis (Chapter 3).

Parameter	Willems		this thesis	
Compressor				
A_c	$7.9 \cdot 10^{-3}$	[m^2]	$6.53 \cdot 10^{-3}$	[m^2]
L_c	1.8	[m]	0.16	[m]
Throttle				
A_T	$\approx A_c$	[m^2]	$9.56 \cdot 10^{-3}$	[m^2]
L_T	0.10	[m]	0.10	[m]
Plenum				
V_p	$2.03 \cdot 10^{-2}$	[m^3]	$2.39 \cdot 10^{-2}$	[m^3]
Density ρ	1.2	[kg/m^3]	f(T,p)	[kg/m^3]
Throttle parameter c_T	0.332	[-]	0.406	[-]
Compressor characteristic shift Δ_{c0}	0.3	[-]	f(N)	[-]

can be determined from measurement. The difference is found in the shape of the surge cycle. The influence of the geometrical parameters on the shape of the surge cycle is discussed in Section 3.2.

Appendix D

Hot-wire calibration

The principle of hot-wire anemometry (HWA) is based on transfer of heat from an electrically heated element to the flow. The heat transfer to the flow depends on the fluid velocity, which cools the heated element. Due to the cooling the electrical resistance of the element drops, which indirectly gives a measure for the fluid velocity An extensive overview of the HWA technique is given by *Bruun [7]*. The hot-wire is used in a Constant Temperature Anemometer (CTA) mode. The length of the hot-wire element was 1 [mm], the thickness was 5 [μm] and was made of tungsten. The overheat ratio of the wire was 1.5.

A relation between the measured output voltage and the velocity can be found when a heat balance of the wire is performed, see for reference *Bruun [7]*. The relation used is:

$$E^2 = A + B \sqrt{U}. \tag{D.1}$$

In which E is the wire voltage, A and B are constant that have to be determined from calibration, and U is the velocity.

The calibration of the hot-wire was performed before every measurement session with use of an airflow out of a nozzle. Figure D.1(a) gives a sketch of the calibration set-up (*[55]*). The airflow out of the nozzle is generated with high-pressure air of 6 [bar]. After the valve, the air is led into a buffer to attenuate the high frequency pressure variations. Before it enters the mass flow controller (MFC) the air is filtered by an oil filter. The MFC is used to regulate the mass flow and thereby indirectly the outlet velocity of the nozzle. From the MFC the air flows through a heater that is controlled by a regulator and a feed-back temperature indicator. The hot-wire probe axis is placed in the main stream direction at the centre line of the jet, which minimizes the influence of the probe on the flow. The hot-wire signal of the anemometer is led via an A/D convertor to a personal computer. The software used to control the sampling of the wire signal is written in LABVIEW. The mass flow through the nozzle is read from the MFC. The relation between the velocity at the nozzle and the mass flow through the nozzle has been determined by calibration, with use of the pressure drop over the nozzle, *Ovink [55]*. The calibration procedure can be found in *Maas [47]*. In Figure D.1(b) a calibration curve is shown from which the calibration constants A and B, in Equation (D.1), are determined. As can be seen, for velocities larger than 4 [m/s] there is a good approximation of the relation between the velocity and the output voltage, for velocities smaller than 4 [m/s] the fit is less accurate. The
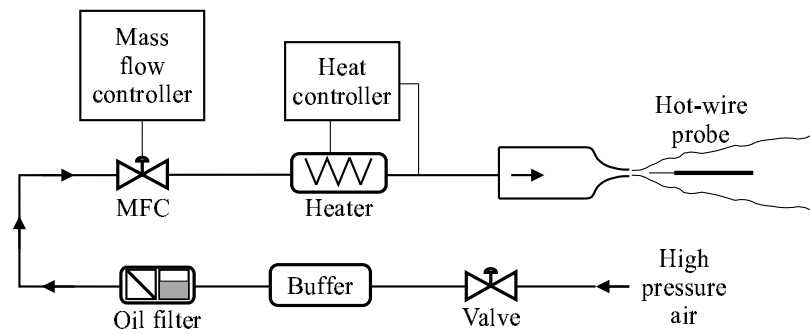
(a) experimental set-up
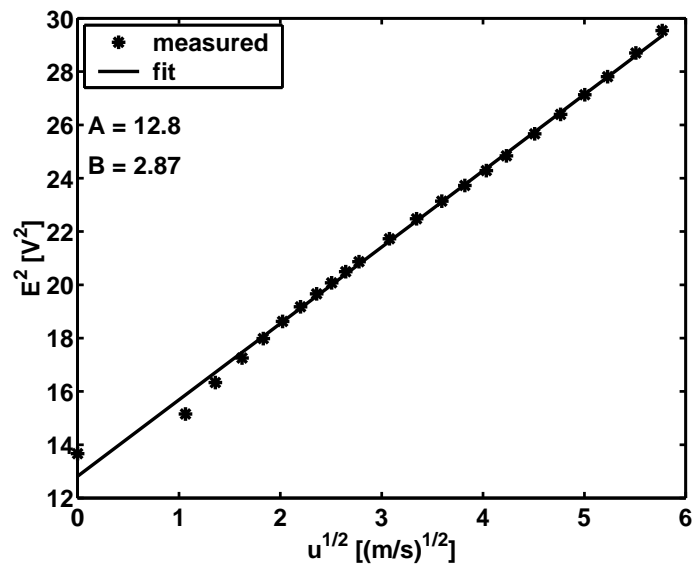
(b) relation between the output voltage and the velocity

Figure D.1: Hot-wire calibration.

velocities expected to be measured in the compressor are between 10 and 30 [m/s] which is in the accurately defined area of the calibration.

Appendix E

Analyses of an oscillating pipe flow

In Chapter 4 the difference between an exact solution of a flow and a solution obtained with a quasi-steady approach of the viscous contribution is studied by means of an analytical study of an unsteady flow in an infinitely long channel. In this chapter the results are presented for a pipe flow (*Schlichting [65]*). In this way it is studied whether the results depend on the geometry.

E.1   Exact solution of an oscillating pipe flow

The pipe is assumed to be infinitely long, with the $x-$axis lying in the centre, see Figure E.1. Since the pipe is assumed to be long, a developed incompressible flow, which motion is independent of x, is studied. From the Navier-Stokes equations a linear equation is obtained:

Figure E.1: Infinitely long pipe.

$$\frac{\partial u}{\partial t} = -\frac{1}{\rho}\frac{dp}{dx} + \nu\frac{1}{r}\left(\frac{\partial}{\partial r}\,r\,\frac{\partial u}{\partial r}\right)\,, \tag{E.1}$$

with boundary conditions $u = 0$ at $r = R$. The pressure gradient is assumed to be set by a harmonically moving piston:

$$-\frac{1}{\rho}\frac{dp}{dx} = \mathcal{K}\,\sin(nt)\,,$$

in which $\mathcal{K}$ is a constant. To solve the linear differential equation a complex notation of the pressure gradient is used:

$$-\frac{1}{\rho}\frac{dp}{dx} = -i\,\mathcal{K}\,e^{int}\,, \tag{E.2}$$

where only the real part has physical significance.

The unsteady velocity profile is:

$$u(r, t) = -\frac{\mathcal{K}}{n} e^{int} \left\{ 1 - \frac{\mathcal{J}_0 \left(\frac{r}{R} \alpha_i \right)}{\mathcal{J}_0 (\alpha_i)} \right\} , \tag{E.3}$$

in which

$$\alpha_i = \alpha \sqrt{-i} ,$$

and the dimensionless:

$$\alpha = R \sqrt{\frac{n}{\nu}}$$

is a Stokes number that characterizes the relative importance of time-dependent inertia terms relative to viscous terms. $\mathcal{J}_0$ is the zeroth order Bessel function.

The exact mass flow is obtained by multiplying the velocity profile by the density and by integrating it over the radius of the pipe:

$$\dot{m}(t) = \frac{i \rho \mathcal{K} \pi R^4}{\alpha_i^2 \nu} \left\{ 1 - \frac{2}{\alpha_i} \frac{\mathcal{J}_1 (\alpha_i)}{\mathcal{J}_0 (\alpha_i)} \right\} e^{int} . \tag{E.4}$$

The momentum Equation (E.1) can be integrated such, that it gives an exact momentum equation expressed in terms of the mass flow:

$$\frac{d\dot{m}}{dt} = -\pi R^2 \frac{\Delta p}{L} + 2\pi R \tau_w . \tag{E.5}$$

Herein, is $\tau_w = \rho \nu \left. \partial u / \partial r \right|_w$ the wall shear stress, with $\left. \partial u / \partial r \right|_w$ the derivative of the velocity at the wall (at $y = R$). The exact wall shear stress can be determined with Equation (E.3):

$$\tau_w = \frac{i \rho \mathcal{K} R}{\alpha} \frac{\mathcal{J}_1 (\alpha)}{\mathcal{J}_0 (\alpha)} e^{int} . \tag{E.6}$$

E.2 Quasi-steady approach of the viscous contribution

For very low frequencies a quasi-steady velocity profile is obtained:

$$u(r, t)_{qs} = -i \frac{\mathcal{K}}{4\nu} \left\{ R^2 - r^2 \right\} e^{int} \qquad (n \to 0) . \tag{E.7}$$

The quasi-steady mass flow is:

$$\dot{m}_{qs}(t) = -\frac{i \rho \mathcal{K} \pi R^4}{8 \nu} e^{int} . \tag{E.8}$$

The momentum equation with a quasi-steady viscous contribution is obtained if a quasi-steady wall shear stress is used:

$$\frac{d\dot{m}}{dt} \;=\; -\pi\,R^2\,\frac{\Delta p}{L} \;+\; 2\pi\,R\,\tau_{w_{qs}} \;. \tag{E.9}$$

The quasi-steady wall shear stress can be determined with Equations (E.7) and (E.8):

$$\tau_{w_{qs}} \;=\; -\,\frac{4\,\nu}{\pi R^3}\,\dot{m}_{qs} \;. \tag{E.10}$$

In Figure E.2 the mass flow determined from the quasi-steady momentum Equation (E.9) is compared with the exact mass flow solution for different Stokes numbers, α. Herein, the amplitude, Λ_m, represents the ratio of the amplitude of the approximated mass flow and the exact mass flow oscillation, characterised by the ratio of the standard deviations, according to:

$$\Lambda_m \;=\; \frac{\text{std}\left(\dot{m}\right)}{\text{std}\left(\dot{m}_{ex}\right)} \;. \tag{E.11}$$

This ratio becomes equal to unity at small and large Stokes numbers.

The phase, $\Delta\theta_m$, is the difference between the approximated mass flow oscillation phase, θ_m, and the exact mass flow oscillation phase, $\theta_{m,ex}$. It indicates the phase lead of the approximated mass flow with respect to the exact mass flow:

$$\Delta\theta_m \;=\; \theta_m \;-\; \theta_{m,ex} \;. \tag{E.12}$$

The geometrical and physical values used are shown in Table E.1. As can be seen in Figure E.2, the quasi-steady approach overestimates the mass flow amplitude for $0.5 < \alpha < 80$. Furthermore, compared to the exact mass flow the quasi-steady approximated mass flow leads for $1 \cdot 10^{-1} < \alpha < 3$ in phase, while for $3 < \alpha < 2 \cdot 10^2$ it is lagging. These results are comparable to those obtained for the channel flow, see Figure 4.2.
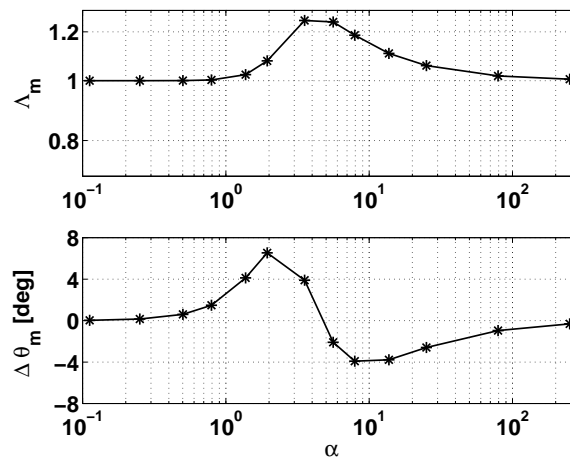

Figure E.2: Quasi-steady approach compared to the exact solution for the pipe flow.

Table E.1: Pipe dimensions.

R	[m]	0.01
L	[m]	0.50
$\mathcal{K}$	[m/s^2]	1.0
ν	[m^2/s]	$1.0 \cdot 10^{-6}$
ρ	[kg/m^3]	$1.0 \cdot 10^{3}$

E.3 Approximation of the error made with the quasi-steady approach

The error χ made with the assumption of a quasi-steady viscous term equals the difference between Equation (E.5) and Equation (E.9). The quasi-steady equation will be improved by an approximation of this χ according:

$$\frac{d\dot{m}}{dt} = -\pi R^2 \frac{\Delta p}{L} + 2\pi R \left\{ \tau_{w_{qs}} + \chi \right\} . \tag{E.13}$$

In which χ is the error between the exact wall shear stress, Equation (E.6), and the quasi-steady wall shear stress, as meant in Equation (E.9) with the exact mass flow, Equation (E.4):

$$\chi = \tau_w - \tau_{w_{qs}} .$$

Following the same derivation as in Section 4.3 the expansion of the error χ is:

$$\chi = \frac{1}{24} \frac{R^2}{\nu} \frac{d\tau_{w_{qs}}}{d\dot{m}} \frac{d\dot{m}}{dt} - \frac{1}{1152} \frac{R^4}{\nu^2} \frac{d\tau_{w_{qs}}}{d\dot{m}} \frac{d^2\dot{m}}{dt^2} + \dots . \tag{E.14}$$

In Figure E.3 the mass flows determined from the corrected Equation (E.13) (new) and the quasi-steady Equation (E.9) (old) are shown both compared to the exact mass flow solution Equation (E.4) for different Stokes numbers. In the corrected equation only the first derivative of the mass flow is taken into account. This means that this approach only is expected to be valid for α smaller than for which the higher order term $-R^2/(1152\,\nu)\ d^2\dot{m}/dt^2 < 1/24\ d\dot{m}/dt$. This is the case for $\alpha < 7$. As can be seen, the new approach gives better results than the old approach for $0.5 < \alpha < 2$.

The dependence on α of the exact error and the correction term:

$$\chi_{app} = \mathcal{C} \frac{R^2}{\nu} \frac{d\tau_{w_{qs}}}{d\dot{m}} \frac{d\dot{m}}{dt} \qquad \left(\mathcal{C} = \frac{1}{24} \right), \tag{E.15}$$

is studied in detail. In Figure E.4(a) the response on the imposed pressure gradient of the exact error and the correction term is shown. Herein, the amplitude, Λ_χ, represents the ratio of the amplitude of the approximated or exact error, χ, and the pressure gradient, dp/dx, according to:

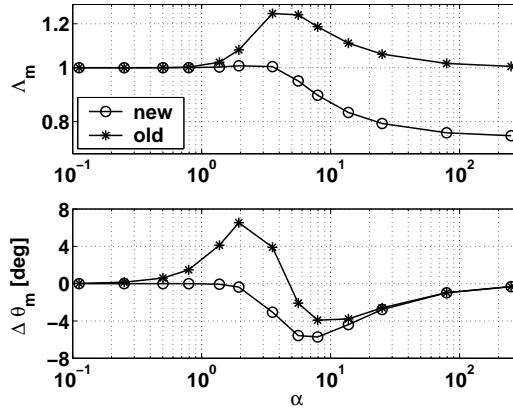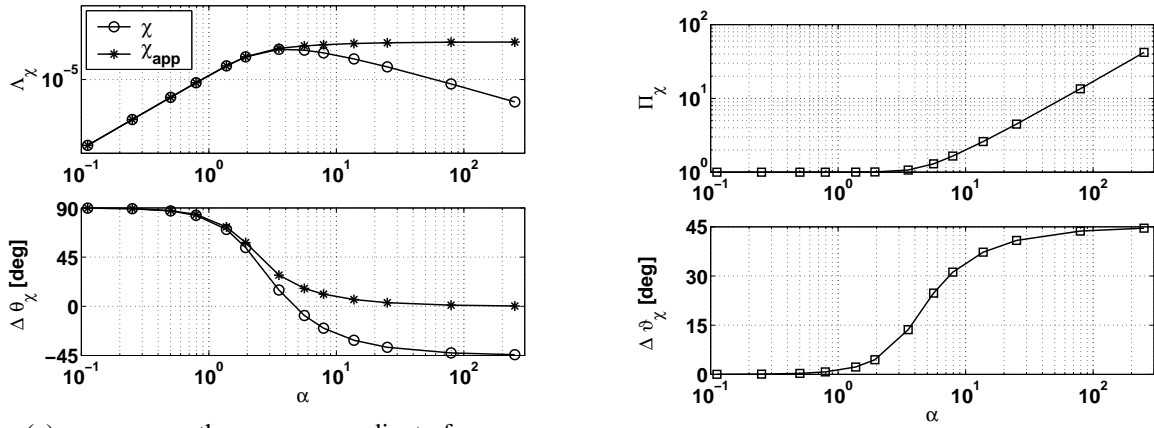$$\Lambda_\chi = \frac{\chi}{dp/dx} .$$

Figure E.3: Effect of the correction for the pipe flow. $\mathcal{C} = \dfrac{1}{24}$

The phase, $\Delta\theta_\chi$, is the difference in phase between the approximated or exact error and the pressure gradient:

$$\Delta\theta_\chi = \theta_\chi - \theta_{dp/dx} \ .$$

It is seen in Figure E.4(a), that the presented approximation of the error applies for $\alpha < 2$.

(a) response on the pressure gradient of error χ and correction χ_{app}

(b) ratio of and phase between χ and χ_{app}

Figure E.4: Error χ and correction χ_{app} as function of α for the pipe flow.

In Figure E.4(b) the difference between the two responses are shown. Herein, the amplitude, Π_χ, represents the ratio of the amplitude of the approximated error, χ_{app}, and the exact error, χ_{ex}, according to:

$$\Pi_\chi = \frac{\chi_{app}}{\chi_{ex}} \ .$$

The phase, $\Delta\vartheta_\chi$, represents the difference between $\Delta\theta_{\chi,app}$ and $\Delta\theta_{\chi,ex}$ that is equal to:

$$\Delta\vartheta_\chi = \theta_{\chi,app} - \theta_{\chi,ex} \ .$$

For $\alpha > 2$ the correction should become smaller and eventually for large α become zero. To achieve this a relaxation equation of the correction term is suggested according:

$$
\begin{aligned}
\frac{d\dot{m}}{dt} &= -\frac{\pi R^2}{L} \Delta p + 2\pi R \left\{ \tau_{w_{qs}} + \chi \right\} , \\
\tau \frac{d\chi}{dt} &= \mathcal{C} \frac{R^2}{\nu} \frac{d\tau_{w_{qs}}}{d\dot{m}} \frac{d\dot{m}}{dt} - \chi .
\end{aligned}
\tag{E.16}
$$

In Figure E.5 the mass flow determined from the corrected and relaxated Equation (E.16) (new) and the quasi-steady Equation (E.9) (old) is shown versus the exact mass flow solution. Time scales belonging to two extremes in Figure E.4(b), $\alpha = 2$ and $\alpha = 200$, are applied and shown in Figures E.5(a) and E.5(c). For the large time scale the old solution without correction is obtained, for the small time scale the correction has a positive influence on the solution compared with Figure E.3. The amplitude can become closer to one over the total α range if the time scale is chosen in between the two extremes. This is shown in Figure E.5(b). For $\alpha = 20$ a good result is obtained for the amplitude and only a small difference from zero (maximum of 4 degree) in the phase.
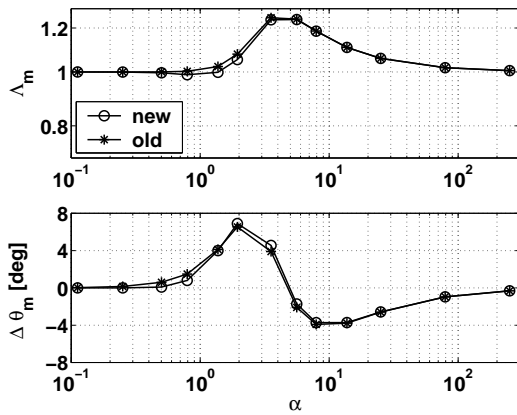
(a) $\tau = 157$ [s] corresponding to $\alpha = 2$
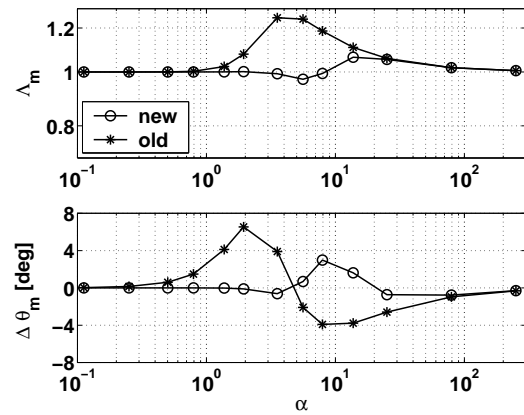
(b) $\tau = 1.6$ [s] corresponding to $\alpha = 20$
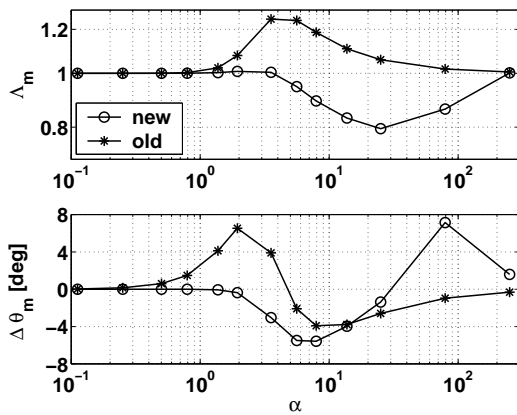
(c) $\tau = 157 \cdot 10^{-4}$ [s] corresponding to $\alpha = 200$

Figure E.5: Effect of the correction with relaxation for the pipe flow.

Appendix F

Water channel set-up and measurement system

To study the relation between the unsteady mass flow and pressure in an oscillating flow at different frequencies a water channel set-up is built. An advantage of this set-up is that it is accessible for detailed measurement of the unsteady velocity profile with which the unsteady mass flow is determined. The experimental set-up consists of two reservoirs, see Figure F.1. In between these reservoirs the test-section (3), which is made of 6 [mm] thick perspex, is mounted. A circulation pump pumps the necessary volume flow from the outlet to the inlet reservoir. The oscillations are applied at the outlet reservoir. With the use of a direct current motor and a variable power supply an oscillation frequency between $0-1$ [Hz] is produced. The rotation of the motor is converted into a linear movement with the use of an acentric positioned rod, which drives a plate. The amplitude of the pressure oscillation produced depends on the amount of water that is distributed by the plate during its oscillation.

F.1   Steady volume flow measurement

The Filtra swimming pool circulation pump of KSB Nederland has a mean capacity of 12 [m^3/h] and a rotational speed of $N = 2800$ [rpm]. Since, the rotational speed is fixed the volume flow has to be controlled by using a by-pass in the pump flow circuit, see Figure 2.1. The steady volume flow through the channel is measured with a volume flow meter downstream the outlet reservoir. The volume flow can be controlled by the valves in a range of $0 - 3.3 \cdot 10^{-3}$ [m^3/s].

F.2   Pressure measurement

To measure pressure differences two low differential pressure sensors (Druck LPM 5480) are available. The specifications are:
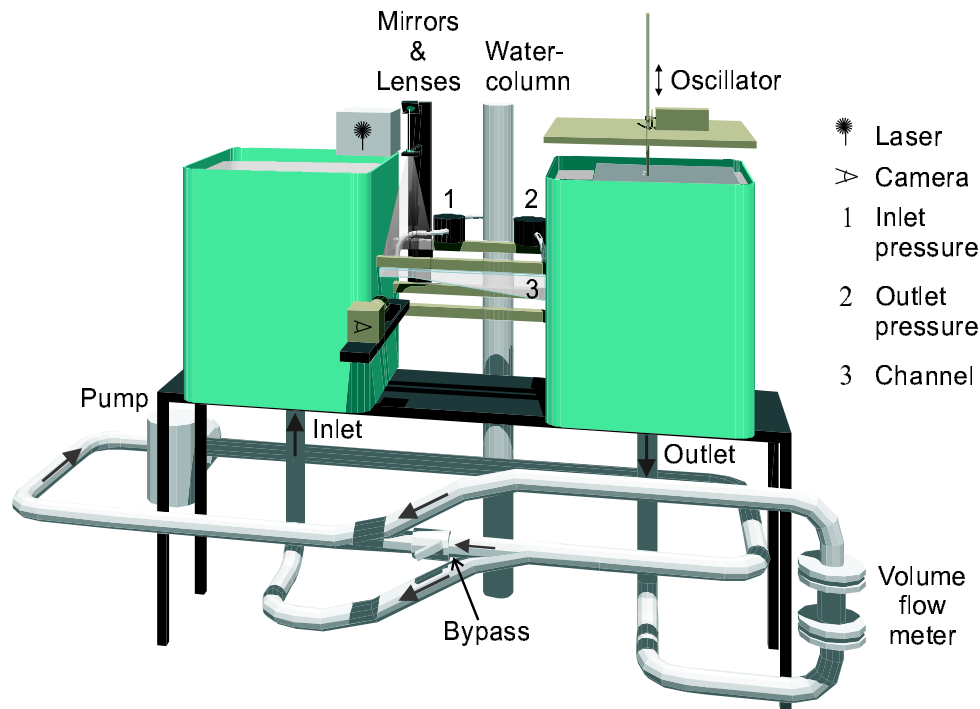
Figure F.1: Experimental water channel set-up.

measuring gain:	-10 to $+10$ [mbar] differential (bi-directional)
accuracy:	max. 0.25 [%] of the measuring gain
output gain:	0 to $\pm\,5$ [V]

Two pressure difference sensors are used. One side of each sensor is connected to the channel and one side to a water column. In this way the pressure duct lengths could be kept small so that the resonance frequency of the pressure sensor ducts did not exist in the oscillation frequency range of interest, $f_o < 1$.

The acquisition of the pressure data is performed with a data acquisition program LabView. The sample frequency of the pressure depends on the oscillation frequency of the oscillator and are tabulated in Table F.2.

F.3 Unsteady mass flow measurement

F.3.1 measurement with laser and CCD-camera

To determine the unsteady mass flow in the channel a Particle Image Velocimetry (PIV) technique is employed, *[4], [60]*. With this non-intrusive method velocity fields are determined from images of a seeded flow. A plane within the flow is illuminated twice by means of a (Nd:YAG) laser. With the laser light a light sheet is made, with mirrors and lenses, which is applied at the top of the channel. The direction of the light sheet is in flow direction and it illuminates approximately $5 \cdot 10^{-2}$ [m] at the beginning of the channel. The flow is seeded with Polyamide

Table F.1: Water channel dimensions.

ν	kinematic viscosity	[m^2/s]	$1.0 \cdot 10^{-6}$
ρ	density	[kg/m^3]	$1.0 \cdot 10^{3}$
test-section dimensions			
d	height (PIV-area)	[m]	0.02
b	width	[m]	0.20
L	length	[m]	0.50
(synthetic) reservoir dimensions			
volume		[m^3]	0.240
height		[m]	0.711
width	*top - bottom*	[m]	0.597 - 0.656
depth	*top - bottom*	[m]	0.597 - 0.656
thickness		[mm]	6
oscillation plate dimensions			
height		[m]	0.01
width		[m]	0.55
depth		[m]	0.49
straightener dimensions			
of one square channel			
height		[mm]	5
width		[mm]	5
length		[mm]	50
thickness		[mm]	0.5

Table F.2: Sample frequency of the pressure transducers.

oscillation frequency [Hz]	sample frequency [Hz]	number of samples
steady flow	20	100
$0 < f_o < 0.10$	5	2048
$0.10 < f_o < 0.30$	10	2048
$0.30 < f_o < 1.0$	20	4096

particles of 20 [μm]. It is assumed that the tracer particles move with local flow velocity between the two illuminations. The light scattered by the particles is recorded by a CCD camera on two separate frames. The displacement of the particle images between the two light pulses are determined by an evaluation (cross-correlation) of the two PIV recordings.

The (dual) frame rate of the PIV-measurement is 13.75 [Hz]. To obtain useful recordings, the CCD camera and the laser are synchronised. The triggered double illumination of the laser and exposure of the CCD camera starts with the user supplied trigger (A) as illustrated in Figure F.2 and Table F.3. Since the laser has a light output delay (B) after the flashlamp is flashed, the time pulse allowance for the first illumination must be programmed into the camera via the command: Transfer Pulse Delay (TPD$= 1.93 \cdot 10^{-4}$ [s]). The second image has a fixed exposure
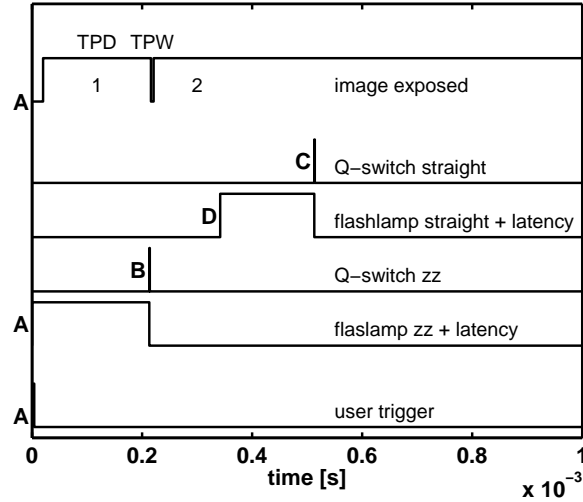
Figure F.2: Time trace of the triggered double exposure.

Table F.3: Time indication of the triggered double exposure.

				position on head
$A = T0$	[s]	flashlamp zz	lamp trig
$B = A + 1.93 \cdot 10^{-4}$	[s]	Q-switch zz	rear
$C = B + x$	[s]	Q-switch straight	side
$D = C - 1.72 \cdot 10^{-4}$	[s]	flashlamp straight	lamp trig delay

period of 33 milliseconds. The time between the two illuminations is set by the time variable x, which depends on the velocity of the flow. Generally, speaking, the displacement of the seeding in the second frame is $1.5 \cdot 10^{-4}$ [m] with respect to the first frame.

F.3.2 PIV evaluation

An example of an exposure of the channel with seeding (white spots) is shown in Figure F.3(a). The boundaries of the channel are recognised by the two horizontal white lines. The large white spot above the channel is a light source that is used to synchronise the PIV-measurements with the pressure measurements. The PIV-recordings are evaluated by locally cross-correlating two frames of single exposures of the channel. Furthermore, the PIV-recordings are subdivided into interrogation areas. In Table F.4 the size and displacement of the interrogation window in x- and y-direction is given. At steady flow measurements the size of the interrogation area is adjusted for larger mean velocities. The flow direction in the channel is mainly in x-direction. Therefore, to obtain a better resolution of the velocity field in y-direction the interrogation window is taken rectangular. Also, an overlap of half the size of the interrogation window is used. For completeness, at the subpixel level the displacement is determined from the correlation data with a Gaussian peak fit, which explanation can be found in *[4]* and *[60]*.

The vectors shown in Figure F.3(b) represent the displacement of each interrogation area in

Table F.4: Interrogation areas.

oscillating and steady mean velocities < 0.6 [m/s]		
interrogation window	$x = 128$ [pixel]	$y = 8$ [pixel]
interrogation window displacement	$\Delta x = 64$ [pixel]	$\Delta y = 4$ [pixel]
steady mean velocities > 0.6 [m/s]		
interrogation window	$x = 256$ [pixel]	$y = 8$ [pixel]
interrogation window displacement	$\Delta x = 128$ [pixel]	$\Delta y = 4$ [pixel]

the channel. As can be seen, the displacement profiles are quite uniform in the window of the measurement and the gradient of the boundary-layer profile is captured in detail. Next, one velocity profile is determined from the mean of the displacement profiles that is divided by the time between the two subsequent exposures.

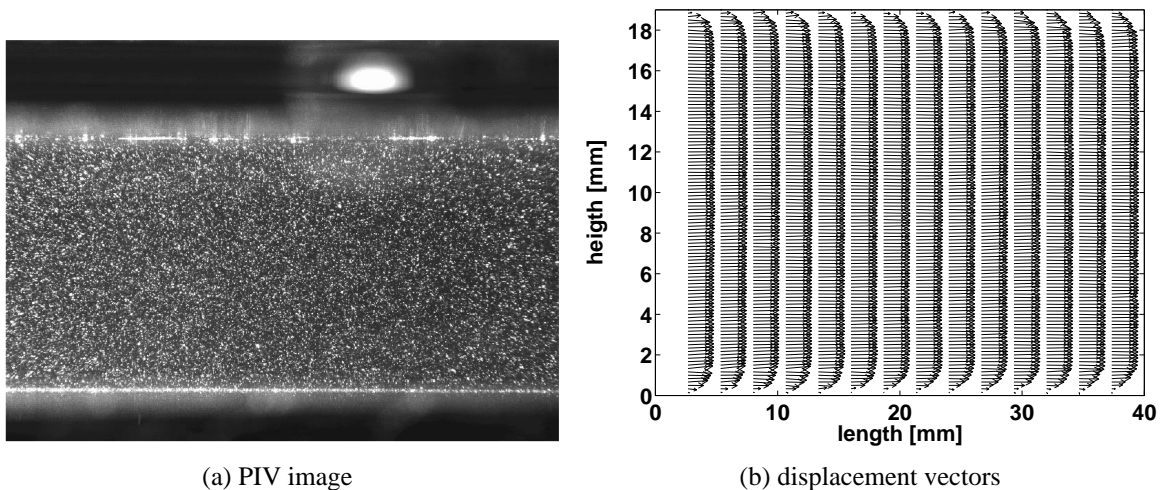(a) PIV image   (b) displacement vectors

Figure F.3: Unsteady velocity measurement with PIV.

Examples of velocity profiles at different phases of the oscillation for three different mean velocities are shown in Figure F.4(a), F.4(c), and F.4(e). For a mean oscillation velocity $\bar{u} \approx$ 0.5 [m/s] the velocity gradient at the walls is large and it leads to a straight profile further away from the walls. No negative velocities are measured. For a smaller mean velocity, $\bar{u} \approx 0.2$ [m/s], the shape of the velocity profile is found to depend on the phase of the oscillation. At some instances the flow near the walls becomes negative and backflow occurs. For a mean oscillation velocity $\bar{u} \approx 0.1$ [m/s] even the flow far from the walls reaches the zero velocity line. Generally speaking, these three velocity profile figures show that with the PIV method it is possible to capture the velocity profile of the flow in detail even when backflow occurs.

Finally, the velocity profiles are used to determine the mass flow oscillation in the channel. By integrating the velocity profile over the height and by multiplication by the density of water, the unsteady mass flow is obtained. The resulting mass flow oscillations are shown in Figure F.4(b), F.4(d), and F.4(f). A smooth sinusoidal mass flow oscillation is found. Furthermore, at the lowest mean oscillation velocity the mass flow becomes negative during a part of the cycle.
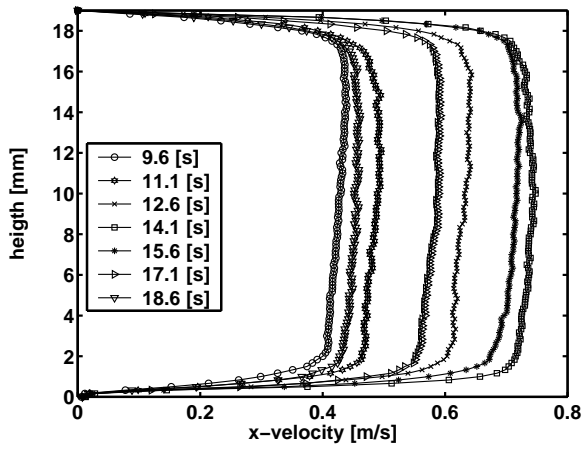
(a) velocity profile: $f = 0.20$ [Hz]
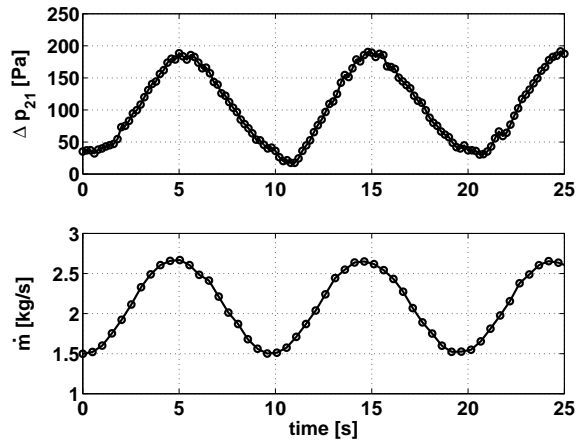
(b) pressure difference and mass flow: $f = 0.20$ [Hz]
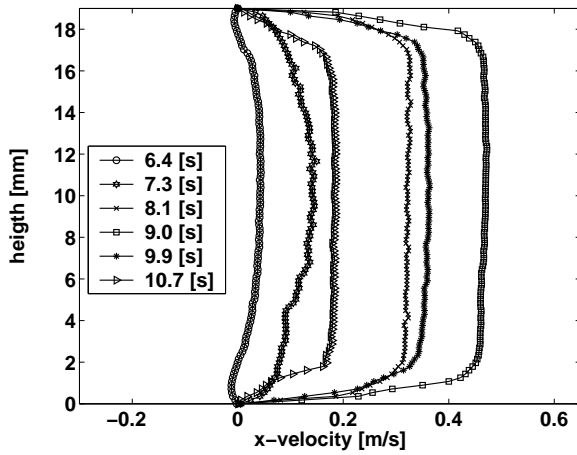
(c) velocity profile: $f = 0.20$ [Hz]
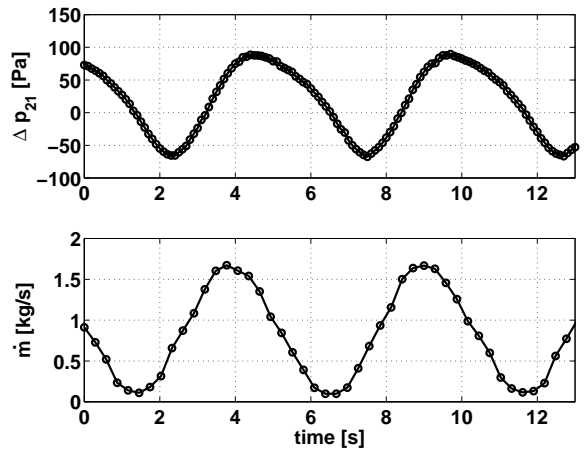
(d) pressure difference and mass flow: $f = 0.20$ [Hz]
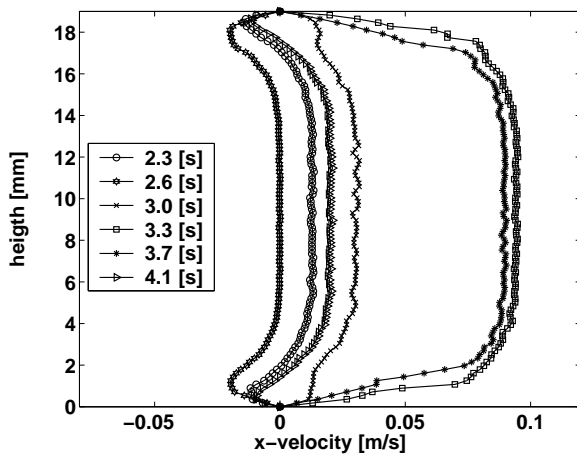
(e) velocity profile: $f = 0.50$ [Hz]
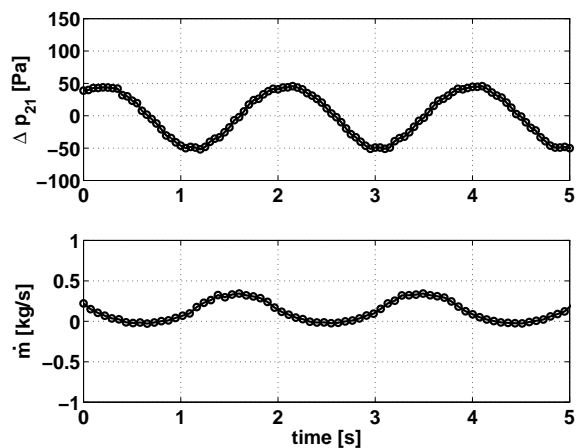
(f) pressure difference and mass flow: $f = 0.50$ [Hz]

Figure F.4: Oscillating divergent channel flow at three different mean velocities.

In Figure F.4(b), F.4(d), and F.4(f) the unsteady pressure differences of the channel are shown as well. The pressure and mass flow measurements are synchronised by using a light source, which is triggered by the oscillator. At a certain position of the oscillator the light is put on for a short period. Together with the pressure measurement, the voltage of the light is measured. As the light is put on a voltage peak is measured and at the "same time" in the PIV measurement the light is captured in one or more frames. A quotation mark is used for the same time since both measurements are only synchronised such that the phase of the period with respect to the oscillator is equal. The pressure measurements could be shifted complete periods in time with respect to the mass flow measurement.

In Figure F.4(b), F.4(d), and F.4(f) the influence of the oscillation frequency with respect to the phase between the pressure difference and the mass flow is seen. For a low frequency both traces nearly follow the same path through the oscillation with respect to time. The phase difference is small. For higher frequency the phase of the mass flow oscillation leads the phase of the pressure difference oscillation. This result is discussed in Chapter 5.

F.4   Phase accuracy

In Chapter 5 the amplitude ratio of and the phase difference between the mass flow and pressure difference measurement is discussed. Here the accuracy of the phase between these two measurement quantities is given.

The (dual) frame rate of the PIV-measurement is 13.75 [Hz]. Which means that 2 exposures are captured in 0.073 [s]. The exposure time of the first image is TPD$= 1.93 \cdot 10^{-4}$ [s], which is too short to capture the synchronisation light. The second image exposure time is $33 \cdot 10^{-3}$ [s], in which the synchronisation light is captured. Now, somewhere in between 0 [s] and 0.073 [s] the light switches on, which is always brought back to $t = 0$ [s]. This introduces a one-sided inaccuracy on the phase of the mass flow with respect to the oscillator. The maximum inaccuracy in phase for a frequency range of $0 < f_o < 1$ [Hz] is equal to $360 \cdot 0.073 f_o$ [deg]. It means that the determined mass flow can lead in phase compared to the real mass flow. Therefore, the determined phase of the mass flow is in between $-360 \cdot 0.073 f_o < \theta_m < 0$ [deg].

The pressure difference is measured synchronic with the oscillator. Furthermore, the voltage change, when the light is switched on, is so steep that hardly any time is past before the light is really on. Therefore, the phase uncertainty of the pressure with respect to the oscillator can be put to zero. The phase difference between the mass flow and pressure measurement is determined by hand, which introduces an error that is approximately ± 1.5 [deg]. Hence, the total inaccuracy of the phase difference between mass flow and the pressure measurement is $-360 \cdot 0.073 f_o - 1.5 < \theta_m - \theta_p < 1.5$ [deg].

Nomenclature

In this appendix the symbols and acronyms used throughout this thesis are explained. A reference to a specific chapter or appendix is made if a symbol is specifically used in this chapter or appendix.

Greek

Symbol	Definition	Dimension	Chapter / Appendix
α	Stokes number $\left(\frac{h}{2}\sqrt{\frac{n}{\nu}}\right)$	[-]	
α_{co}	maximum α without relaxation	[-]	
α_i	$\alpha\sqrt{-i}$	[-]	
α_r	α relaxation determining τ	[-]	
γ	ratio of specific heats	[-]	
Δ_{co}	shift of valley point ψ_{c_0}	[-]	
δ	boundary-layer thickness	[m]	
δ_s	steady boundary-layer thickness	[m]	
θ	phase	[deg]	
ϑ	$\theta_{\chi,app} - \theta_{\chi,ex}$	[-]	
Λ	amplitude ratio	[-]	
ν	kinematic viscosity	[m^2 s^{-1}]	
ξ	relative position of the hot-wire probe	[-]	2
Π_χ	χ_{app}/χ_{ex}	[-]	
ρ	density	[kg m^{-3}]	
τ	time constant	[s]	
$\tilde{\tau}$	nondimensional time constant	[-]	C
τ_w	wall shear stress	[kg m^{-1} s^{-2}]	
ϕ	dimensionless mass flow, flow coefficient	[-]	
χ	error $(\tau_w - \tau_{w_{qs}})$	[kg m^{-1} s^{-2}]	
ψ	dimensionless pressure rise	[-]	
ψ	pressure rise coefficient	[-]	
ψ_{c_0}	ψ at zero flow coefficient	[-]	
ω	frequency	[rad s^{-1}]	

Symbol

Symbol	Definition	Dimension	Chapter / Appendix
A	area	[m^2]	
A	calibration constant	[V^2]	D
A	time indication	[s]	F
$\mathcal{A}$	multiplication factor	[kg/m]	
a	speed of sound	[m/s]	
B	$\frac{U}{2\omega_H L_c}$	[-]	
B	calibration constant	[V^2 (m/s)$^{-1/2}$]	D
B	time indication	[s]	F
b	(exit impeller tip) width	[m]	
C	time indication	[s]	F
$\mathcal{C}$	constant	[-]	
$\mathcal{C}'$	constant	[-]	
C_x	axial velocity	[m/s]	
C_m	meridional velocity	[m/s]	C
c_T	throttle valve parameter	[-]	
D	time indication	[s]	F
d	diameter	[m]	
d	height	[m]	5, F
E	wire voltage	[V]	D
f	frequency	[Hz]	
G	$\frac{L_T A_c}{L_c A_T}$	[-]	
H	pressure rise coefficient parameter	[-]	
h	height	[m]	
$\mathcal{J}_0$	zeroth order Bessel function	[-]	E
$\mathcal{J}_1$	first order Bessel function	[-]	E
$\mathcal{K}$	constant	[m s^{-2}]	
L	length	[m]	
M	mass flow amplitude ratio	[-]	
M	Mach number	[-]	A
$\dot{m}$	mass flow	[kg/s]	
N	rotational speed	[rpm]	
N	number of rotor revolutions	[-]	C
n	$2\,\pi\,f$	[rad/s]	
P	pressure difference amplitude ratio	[-]	
p	pressure	[Pa]	
Δp	pressure difference	[Pa]	
R	gas constant	[J/kg/K]	
R	radius	[m]	
Re	Reynolds number	[-]	A
r	radius direction	[m]	
$\mathcal{S}$	Strouhal number $\left(\frac{\overline{u}f_o}{L}\right)$	[-]	5

Symbol continue

Symbol	Definition	Dimension	Chapter / Appendix
T	temperature	[K]	
t	time	[s]	
$\tilde{t}$	dimensionless time	[-]	
U	blade speed	[m/s]	
U	velocity	[m/s]	D
u	velocity	[m/s]	
V	volume	[m^3]	
V_x	axial velocity	[m/s]	
v	velocity	[m/s]	
W	flow coefficient parameter	[-]	
x	x-direction	[m]	
x	time variable	[s]	F
Y_T	dimensionless throttle valve position	[-]	
y	throttle valve position	[V]	2
y	y-direction	[m]	
Z	number of impeller blades	[-]	2
z	number of diffuser blades	[-]	2
z	z-direction	[m]	

Acronym

Symbol	Definition	Chapter / Appendix
CCD	charge coupled device	F
H-W	hot-wire	2
MFC	mass flow controller	D
Nd:YAG	neodym (ion): yttrium-aluminum-garnet (crystals)	F
PIV	particle image velocimetry	
PSD	power spectral density	
TPD	transfer pulse delay	F
VFM	volume flow meter	5, F

Subscript

Symbol	Definition	Chapter / Appendix
0	ambient condition	
1	at compressor inlet	
1	at channel inlet	5
2	at compressor outlet	
2	impeller outlet	2
2	at channel outlet	5
3	at throttle inlet	
3	vanes inlet	2
4	vanes outlet	2
a	casing	
a	analytical	6
app	approximated	
b	exit impeller tip width	A
c	compressor	
c	blade chord length	A
ex	exact	
H	Helmholtz	
h	hub	
m	mass flow	
o	oscillation	
or	orifice	
p	plenum	
p	pressure difference	5
qs	quasi-steady	
s	surge	
ss	steady-state	
T	throttle	
t	at the tip	
t	total condition	5
t	meridional	C
w	at the wall	
χ	error χ versus dp/dx	

Samenvatting

Voor kleine massastromen wordt het operationele werkgebied van compressorsystemen begrensd door het optreden van aërodynamische stromingsinstabiliteiten. Deze instabiliteiten kunnen leiden tot een rampzalige storing van de compressor door het ontstaan van een te hoge mechanische en thermische belasting. Eén van deze instabiliteiten is *surge* van het compressorsysteem dat wordt gekarakteriseerd door grote oscillaties in de drukopbouw van de compressor en een instationaire massastroom. Dit proefschrift gaat over het meten en modelleren van surge in een compressorsysteem met een centrifugaal compressor.

In een experimentele gasturbineinstallatie zijn door middel van drukmetingen bij de uitlaat van de compressor, voor verschillende rotatiesnelheden en smoorklepstanden, de karakteristieken van surge bepaald. Uit de drukmetingen zijn de minimum en maximum drukopbouw tijdens een surgecyclus en de surgefrequentie ($\approx 19-24$ [Hz]) bepaald. Het blijkt dat de surgefrequentie toeneemt als de smoorklep wordt gesloten. Dit geeft aan dat het systeem een *classic* of *deep* surgecyclus doorloopt. Om de massastroom oscillatie te bestuderen, is een hittedraad bij de inlaat van de compressor geplaatst. Door de gemeten snelheid te correleren met de massastroom is een impressie van de periode met een positieve massastroom in de surgecyclus verkregen.

Bestaande simulatiemodellen van surge zijn gebaseerd op een *lumped parameter* benadering waarin de prestatie van de compressor quasi-stationair wordt gemodelleerd. Als in dit conventionele model de geometrisch bepaalde parameters van het compressorsysteem worden gebruikt is, ten opzichte van de experimenten, de gesimuleerde maximale drukopbouw te laag en de gesimuleerde surgefrequentie te hoog. Alleen de vorm van de surgecyclus wordt dichtbij de maximale drukopbouw goed gesimuleerd. De surgefrequentie en de maximale drukopbouw kunnen goed worden gesimuleerd wanneer de verhouding van de compressorlengte en het volume van het plenum met een factor tien, ten opzichte van de fysische bepaalde verhouding, wordt verhoogd. De vorm van de surgecyclus komt dan echter dichtbij de maximale drukopbouw niet overeen.

In dit proefschrift is een nieuwe correctie ontwikkeld waarmee, ten opzichte van simulaties met het conventionele model, betere resultaten worden verkregen. In het conventionele model wordt aangenomen dat de drukopbouw van de compressor quasi-stationair reageert op massastroom veranderingen, terwijl een instationaire benadering realistischer is. De ontwikkelde correctie geeft de invloed van een instationaire grenslaag ten opzichte van een stationaire grenslaag op de prestatie van de compressor weer. De correctie is afgeleid door de instationaire impulsvergelijking van een volledig ontwikkelde laminaire stroming in een kanaal te beschouwen. In deze versimpelde afleiding komt het Stokes getal (α) als een belangrijke parameter naar voren. Wanneer de ontwikkelde correctie wordt toegepast in het gebied $0.5 < \alpha < 80$, komt de gesimuleerde

amplitude en fase van de druk en massastroom oscillaties beter overeen met de exacte oplossing.

Vervolgens is de ontwikkelde correctie toegepast op een turbulente inlaatstroming. Om de simulaties te kunnen vergelijken zijn er PIV- en drukmetingen in een waterkanaal gedaan, waarin een kanaal met en zonder een drukgradiënt is getest voor $0.7 < \alpha < 7.5$. Vooral voor het kanaal met een tegenwerkende drukgradiënt is een verschil gevonden tussen de simulaties met het conventionele model en de experimenten. Simulaties met het verbeterde model geven een amplitudeverhouding en een fase, van de massastroom en de druk, die goed overeenkomen met de metingen.

Tot slot is de correctie toegepast op het experimentele compressorsysteem, waarin $\alpha \approx 10$. Simulaties met het verbeterde model resulteren in een surgefrequentie en een maximum drukopbouw, alsook een drukopbouwperiode van de surgecyclus, die goed overeenkomen met de metingen. Een winst van het verbeterde model is dat de parameters te bepalen zijn uit de fysische afmeting van het compressorsysteem. Daarnaast is een parameterverhouding gevonden die, in plaats van afhankelijk te zijn van het compressorsysteem waarin de compressor wordt gebruikt, specifiek afhankelijk is van de compressor.

Nawoord

Ondanks dat alleen mijn naam op de eerste bladzijde van dit proefschrift vermeld staat moge het duidelijk zijn dat dit niet had kunnen worden geschreven zonder medewerking van velen. Zonder de co-promotor Rick de Lange was dit proefschrift niet tot stand gekomen. Met zijn enorme inzicht in fysische en wiskundige zaken wist hij altijd een richting te geven voor verder onderzoek, wanneer ik weer eens vast liep in het project. Voor het doelgericht werken en de coherentie van het project heb ik goed kunnen terugvallen op de promotor Anton van Steenhoven.

Naast deze twee directe begeleiders heb ik veel steun gehad van de overige leden van het Compressor Surge Project. De maandelijkse discussies met de regelboys, Frank Willems, Bram de Jager en Jan Kok, gaven mij een bredere kijk op hoe compressor surge kan worden bestudeert. Ik dank hen dan ook voor de waardevolle adviezen, de ondersteuning en de prettige werksfeer.

De enorm goede werksfeer bij Energie Technologie kan ik niet anders omschrijven dan een warme deken en dat ik de mensen als mijn werkfamilie heb beschouwd. Allereerst hebben we mijn werkpappa Frits van Veghel, die altijd voor me klaar stond als er weer eens met gasturbine moest worden gedraaid ná werktijd. Zijn zin in werken, interesse in mensen en liefde voor sport hebben mij altijd erg aangesproken. Bovendien was hij de persoon die samen met werkoom Frank Seegers altijd klaar stond met een bak koffie voor de nodige ontspanning op een dag. Dan hebben we mijn werkmamma Rian Tielemans, die de voor haar dodelijk vermoeiende gave bezit zich voor iedereen in te kunnen zetten. Rian ik heb het altijd reuze fijn gevonden even bij je langs te komen om te kletsen.

Mijn werkoom Lambert van der Schoot wist zelfs met de vaagste aanwijzingen en tekeningen de in dit proefschrift beschreven opstellingen te maken. Het is gebleken dat het bewerken van perspex met een föhn al snel tot een kwaliteit van Lambert behoorde, hetgeen bewijst dat hij niet terugschrok voor onbekende bewerkingen. Door mij een grote mate van zelfstandigheid te geven in de werkplaats kregen werkoom Peter Ewalts en Lambert het voor mekaar om van iemand met twee linkerhanden in een zeer korte tijd een knutselmeid te maken. Lambert ik vind het een reuze gemis dat je mijn promotie niet kan meemaken.

Vele mensen hebben dagelijks iets voor mij betekent. Hen wil ik dan ook tot mijn werkbroers en werkzussen rekenen. Zoals vaker in een grote familie moet je je kamer delen met een broer of zus. Tijdens mijn promotiewerk was dit met achtereenvolgens Harm van Essen, Rob Schook en Marja Houben. Stuk voor stuk hebben jullie ervoor gezorgd dat ik prettig werkte, gemotiveerd werd en aanspraak had. Mocht ik dan toch een keertje helemaal geen energie meer hebben dan deed een praatje en een lach met werkzus Marjan Dijk veel goed. Zij wist er altijd de positieve zin weer in te brengen. Grote broers kunnen je veel steun geven in tijden dat je

een nieuw pad gaat bewandelen in je ontwikkeling. Tot mijn grote werkbroers reken ik Rob Bastiaans, Bart Somers en Douwe de Vries. Jullie kalmte in gestresste tijden en jullie helpende hand bij vele vraagstukken heeft me zeer gesteund in mijn werk. Alhoewel broers en zussen qua leeftijd altijd minstens negen maanden uit elkaar liggen (meerlingen uitgesloten) kwamen bij onze vakgroep de Promovendi met golven. In mijn golf heb ik steun gekregen van René Kieft, Misheck Mwaba, Marco van Beek, Maurice Limpens, Bart Lammers, Marco Nagtegaal, Karel-Joop Bosschaart, Jeroen van Oijen en Ronald Rook.

Het voordeel van de universiteit zijn de fantastische sportfaciliteiten. Zaalvoetballen met het vakgroepsteam, squashen met Grazia Lamanna en cardiofitnessen met Marja zijn sporten waarmee ik mijn zinnen heb kunnen verzetten. Na vier jaar te hebben gewaterpoloed in de tongelreep heb ik zelf nog een jaartje kunnen genieten van het zwembad dat nu aan het sportcentrum is toegevoegd. Dit brengt mij tot het bedanken van alle mensen die ik heb ontmoet binnen Nayade. Vooral de waarde van alle meiden die ik om me heen had tijdens de vele wedstrijden en trainingen weet ik nu goed in te schatten. Het is voor mij een aan den lijve ondervonden beleving dat vrouwen niet altijd met elkaar in de clinch liggen en gezamenlijk tot grote prestaties kunnen komen. Dames bedankt voor jullie goedheid en alomvattend begrip.

Voor mijn vrienden en familie willen ik mijn enorme waardering uitspreken. Ondanks alle gekke capriolen die ik en mijn lichaam uithalen, blijven jullie in mij geïnteresseerd en mij met warmte omringen. Deze steun zorgt ervoor dat ik het leven kan ervaren zoals ik hem nu beleef.

Als laatste wil ik Jeroen enorm bedanken. Eigenlijk is dit boekje ook een beetje van jou. Zonder jou onvoorwaardelijke steun zou het mij nooit zijn gelukt!

Corine

Eindhoven - Augustus 2002

Curriculum Vitae

Corine Meuleman werd geboren op 6 januari 1972 in Goor. In 1990 behaalde zij haar VWO-diploma aan de scholengemeenschap Marianum in Groenlo. Aansluitend begon zij de studie luchtvaart- en ruimtevaarttechniek aan de Technische Universiteit Delft. Na het behalen van haar propaedeuse heeft ze voor de vakgroep lage snelheids aërodynamica gekozen.

In 1994 heeft zij een stageproject verricht aan de NTH-Trondheim in Noorwegen, onder begeleiding van prof.dr.techn. H. Nørstrud. Hierin is een theoretisch en experimentele studie gedaan naar de weerstand van "downhill"-skiers en schanspringers. In 1995 heeft zij een stageproject verricht in het lage snelheids laboratorium in Delft, onder begeleiding van dr.ir. B. van Hest en ir. D. Passchier. Hierin is experimenteel onderzoek gedaan naar de interactie van turbulente spots.

De studie luchtvaart- en ruimtevaarttechniek werd in augustus 1996 afgerond, onder leiding van dr.ir. R. Henkes en Prof.dr.ir. J. van Ingen, met een afstudeerscriptie getiteld: 'Computation of laminar separation bubbles in boundary-layers with a streamwise pressure gradient'. Het project omvatte een een numerieke studie naar laminaire loslaatblazen in grenslaagstromingen met een drukgradiënt, die met behulp van de methode van 'sterke visceuze-niet visceuze interactie' is uitgevoerd.

Op 1 oktober 1996 trad zij in dienst van de faculteit werktuigbouwkunde aan de Technische Universiteit Eindhoven. Binnen de sectie Energietechnologie heeft zij, onder begeleiding van prof.dr.ir. A.A. van Steenhoven en dr.ir. H.C. de Lange, onderzoek gedaan naar het fenomeen centrifugaal compressor surge. Het verrichte werk heeft tot de totstandkoming van dit proefschrift geleid. Tijdens de promotie heeft zij voor 2 maanden gewerkt aan een numerieke studie naar de prestatie van een twee-traps turbine; met en zonder stromingslekkage aan de tip, onder leiding van Dr. M. Decker, bij Siemens Power Generation (KWU), Steam Turbine Development, Mühlheim-Ruhr in Duitsland.